



PONTIFICIA UNIVERSIDAD CATOLICA DE CHILE

# Spatial biology of Ising-like synthetic genetic networks

Tesis entregada a la Pontificia Universidad Católica de Chile en  
cumplimiento parcial de los requisitos para optar al Grado de  
Doctor en Ciencias con mención en Genética Molecular y  
Microbiología

Por

KEVIN MATÍAS SIMPSON ALFARO

Directores de Tesis:

Fernán Federici Noe

Juan Keymer Vergara

July 2021

*Para Camila ...*



# *Abstract*

Understanding how spatially-correlated cellular states emerge from the local interaction of gene network dynamics is a fundamental challenge in biology. Short and long-range correlations and anti-correlations in gene expression can be found in spatially-distributed cellular systems such as eukaryotic tissues and microbial communities. However, the study of gene spatial correlations emerging from cell-cell coupling in natural systems is difficult since complex interactions are the norm. An alternative is to generate synthetic genetic networks (SGNs) that capture essential features of cell-cell interactions and reveal their influence in the emergence of cellular state patterns. Here, we combine synthetic biology, theoretical modelling and computational simulations to study the emergence of macroscopic gene correlations and address possible mechanisms for multi-scale self-organization of gene states in bacteria. We applied the Ising model as a theoretical framework to study the self-organization of spatially-correlated gene expression in two-state SGNs that are coupled by short-range chemical signals in *E. coli*. Inspired by the Ising model, we name these SGNs ferromagnetic or anti-ferromagnetic depending if they stabilize the same or the opposite state in neighboring cells. As predicted by our simulations that combine the two-dimensional Ising model with the Contact Process lattice model of cell population dynamics, these SGNs allowed the self-organization of spatial patterns of short and long-scale cellular state domains in bacterial colonies, where the size of the domains depends on the type of interaction, ferromagnetic or anti-ferromagnetic. The emergence of spatial correlations showed to be independent of the cell shape and the underpinning mechanical forces. The similarity found between ferromagnetic colonies and simulated ferromagnetic populations suggest these colonies are near the critical point of phase transition, implying that far regions in the colony are correlated. This work provides resources and a general scope theoretical framework that explain how both short and long-range correlations (and anti-correlations) are able to self-organize from locally-interacting networks. These results on multi-scale organization of gene network states shed light onto the study of pattern formation in developmental biology and microbial ecology, as well as provide a theoretical framework for the engineering of spatially-arranged cell systems.

# *Resumen*

Comprender cómo estados celulares espacialmente correlacionados emergen a partir de interacciones locales de redes génicas es un desafío fundamental en biología. Correlaciones de corto y largo alcance en la expresión de genes emergen en sistemas celulares espacialmente distribuidos como tejidos eucariotas y comunidades microbianas. Sin embargo, el estudio de correlaciones espaciales génicas que emergen a partir del acople célula-célula en sistemas naturales es difícil ya que interacciones complejas son la norma. Una alternativa es generar redes genéticas sintéticas (SGN) que capturen características esenciales de interacciones célula-célula y que revelen su influencia en la emergencia de patrones de estados celulares. Aquí, combinamos biología sintética, modelamiento teórico y simulaciones computacionales para estudiar la emergencia de correlaciones génicas macroscópicas y abordar posibles mecanismos responsables de la auto-organización multi-escala de estados génicos en bacteria. Utilizamos el modelo de Ising como marco teórico para estudiar la auto-organización de la expresión génica en SGN con dos estados acoplados por señales químicas de corto alcance en *E. coli*. Inspirados en el modelo de Ising, denominamos a estas SGN ferromagnéticas o anti-ferromagnéticas dependiendo de si estabilizan el mismo estado celular o el opuesto en células vecinas. De acuerdo a las predicciones de nuestras simulaciones que combinan el modelo de Ising con el modelo de lattice "Contact Process", estas SGN permitieron la auto-organización de patrones espaciales de dominios de estados celulares de corta y larga escala en colonias bacterianas, en donde el tamaño de los dominios depende del tipo de interacción. La emergencia de correlaciones espaciales mostró ser independiente de la forma de las células y las fuerzas mecánicas subyacentes. La similitud encontrada entre colonias ferromagnéticas y poblaciones simuladas sugiere que estas colonias se encuentran cerca al punto crítico de la transición de fases, implicando que regiones lejanas de las colonias se encuentran correlacionadas. Este trabajo proporciona recursos y un marco teórico de alcance general que explica cómo correlaciones de corto y largo alcance son capaces de auto-organizarse a partir de redes que interactúan localmente. Estos resultados sobre la organización multi-escala proveen información adicional para el estudio de la formación de patrones en biología del desarrollo y ecología microbiana, además de proporcionar un marco teórico para la ingeniería de sistemas celulares distribuidos espacialmente.

# *Acknowledgements*

I would like to express my deepest gratitude to my research supervisor Fernán Federici. It was a real pleasure working under his guidance. Beyond all the knowledge and wisdom that I may have acquired during these years, what I value and appreciate the most is the affection and concern that he showed me not as a researcher, but as a person. I really enjoyed my years in the Ph.D., and I owe it in large part to him.

I would also like to thank my "second" research supervisor to Juan Keymer. Juan was my co-tutor only on the paper, because in reality he helped me as much as a tutor. From the beginning I admired his immense knowledge (really, I am still impressed by his ability to know about everything). However, what I appreciate the most are the life lessons he passed on to me. I am tremendously grateful that I was able to learn science while learning from his experiences. I want to extend my heartfelt thanks to Janneke Noorlag, who was always willing to help me. Like Juan, Janneke not only helped me in my research, but also in my life decisions. For both of you, I only have words of sincere gratitude and affection.

I feel extremely fortunate to have had the opportunity to develop my research in an environment like the one generated by Fernán, Juan and Janneke. For that, I will always be grateful.

I would like to thank the members of my committee María Luisa Cordero, Luis Larrondo and Andreas Schüller, for taking the time to supervise my thesis. I appreciate their concern and encouragement, and also the words of advice they gave me that helped me improve my research. I would like to express my gratitude especially to María Luisa Cordero, for allowing me to use her laboratory when things were not working. I also want to thank Timothy Rudge for all his support and help with my experiments.

Words are not enough to express the immense gratitude I feel towards Peter Galajda, who opened the doors of his laboratory in Hungary without even knowing me. I owe a deep sense of gratitude to Peter for making me feel welcome in his laboratory and for helping me with my research. I want to extend my sincere thanks to his research group, who welcomed me and helped me during my stay in Hungary. I want to especially thank Ágnes Ábrahám, who dedicated most of her time to help me. The time I spent in Hungary was easily one of the moments I

most enjoyed during my Ph.D., and I owe it in large part to Peter and his research group. I am extremely grateful for all the experiences and knowledge that I was able to gain during my stay in the beautiful Szeged, something that I will never forget and hope to repeat one day.

I would like to thank my research colleagues and friends that I made during these years in the different laboratories in which I worked. Not only did they help me with the experiments, but they also made doing experiments a lot more fun. I also thank my friends from my generation of the Ph.D. I probably did not show it enough, but they were an important part during these years, and contributed greatly to making the Ph.D. a phase that I really enjoyed. I would like to especially thank Miles Wetherington, who not only helped me here in Chile, but also in Hungary. I would have liked to share more with him.

I am extremely grateful to my parents for their love, caring and sacrifices they made for me. It would have been impossible to get this far without their incessant support. One life is not enough to pay for everything they have done for me, and the only way I know to give them back a little is to keep trying every day to do better.

Finally, but perhaps most importantly, I would like to thank the person who gave me the strength to keep going all this time. Camila, my love, my life. None of this would have been possible without your love, concern, and understanding. Everything was made so much easier knowing that when I got home, you would be there. I have so much to thank you, so many moments that I would like to share with you, but there is no time left ... Thank you for accompanying me to be alone.

This research was supported by the National Agency for Research and Development (ANID), Scholarship Program, Beca de Doctorado Nacional 2016 - 21160554; ANID – Núcleo Milenio Física Materia Activa - Iniciativa Científica Milenio; ANID Fondecyt Regular 1191893; ANID – Iniciativa Científica Milenio – ICN17-022; ANID Fondecyt Regular 1211218.

# Contents

<b>Abstract</b>	<b>ii</b>
<b>Resumen</b>	<b>iii</b>
<b>Acknowledgements</b>	<b>iv</b>
<b>List of Figures</b>	<b>ix</b>
<b>List of Tables</b>	<b>xi</b>
<b>Abbreviations</b>	<b>xii</b>
<b>1 Introduction</b>	<b>1</b>
1.1 Spatial patterns of gene expression in multicellular systems . . . . .	1
1.2 Positive and negative spatial correlations of gene states . . . . .	3
1.3 General models for pattern formation in multicellular systems: The Ising Model . . . . .	4
1.4 The Ising Model in biological systems . . . . .	9
1.5 Synthetic biology as a tool for studying pattern formation . . . . .	11
1.6 Orthogonal system for cell-to-cell communication . . . . .	12
1.7 Project rationale . . . . .	13
1.8 Hypothesis . . . . .	14
1.9 Objectives . . . . .	14
1.9.1 General Objective . . . . .	14
1.9.2 Specific Objectives . . . . .	14
<b>2 Materials and Methods</b>	<b>15</b>
2.1 Computational modeling . . . . .	15
2.2 Bacterial strains and Growth conditions . . . . .	15
2.3 Molecular cloning . . . . .	16
2.3.1 Bacterial transformation . . . . .	16
2.3.2 Selection of positive colonies by Colony PCR . . . . .	16
2.3.3 Generation of DNA fragments for Gibson assembly . . . . .	17
2.3.4 DNA purification . . . . .	18

2.3.5	Plasmid construction . . . . .	19
2.3.5.1	Golden Gate assembly . . . . .	19
2.3.5.2	Gibson assembly . . . . .	21
2.4	Plate fluorometry . . . . .	23
2.5	Microscopy . . . . .	24
2.6	Image analysis . . . . .	24
2.7	Microfluidic devices . . . . .	26
2.7.1	Fabrication of the master mold of the mother machine . . .	26
2.7.2	Fabrication of PDMS microfluidic devices . . . . .	27
<b>3</b>	<b>Computational Modeling</b>	<b>28</b>
3.1	Use a spin model to study the behaviour of two-state and coupled systems in a population of growing cells . . . . .	28
3.1.1	Simulation of the Ising model during the growth of a bacterial population . . . . .	28
3.2	C Code of the CP-IM simulations that combines the Contact Process and the Ising Model . . . . .	30
3.2.1	Simulation of the two-dimensional Ising model in growing cell populations . . . . .	38
<b>4</b>	<b>Two-state and coupled bacterial systems</b>	<b>43</b>
4.1	Design and construct synthetic bacterial systems that exhibit two states and coupling between them . . . . .	43
4.1.1	Generation of coupled two-state gene networks in bacteria .	43
4.1.2	Behaviour of ferromagnetic and anti-ferromagnetic populations in a well-mixed environment . . . . .	46
4.2	Study of spatial patterns generated by the two-state coupled systems in bacterial colonies . . . . .	52
4.2.1	Ising-like patterns emerge in bacterial colonies of ferromagnetic and anti-ferromagnetic rod-shaped cells . . . . .	52
4.2.2	Ising-like patterns in bacterial colonies of ferromagnetic and anti-ferromagnetic spherical cells . . . . .	56
4.2.3	Spatial correlations in ferromagnetic and anti-ferromagnetic bacterial colonies . . . . .	64
4.2.4	Percolation theory . . . . .	67
<b>5</b>	<b>Microfluidics</b>	<b>69</b>
5.1	Dynamics of the two-state and coupled systems in micro-fabricated environments . . . . .	69
5.1.1	The classic mother machine and the addition of side channels	69
<b>6</b>	<b>Discussion and Conclusions</b>	<b>77</b>
6.1	Short-range two-state coupling . . . . .	77
6.2	SGNs that generate Ising-like interactions in bacteria . . . . .	80
6.2.1	Ferromagnetic interactions . . . . .	81
6.2.2	Anti-ferromagnetic interactions . . . . .	82

---

6.3	The Moran effect . . . . .	84
6.4	Spatial autocorrelation . . . . .	85
6.4.1	Behavior of the two-state and coupled systems in the mother machine . . . . .	87
6.5	Conclusions . . . . .	90
A	Cellular state patterns generated in colonies of cells carrying the coupled two-state systems	91
B	Python program to calculate the Hamming distance	96
	Bibliography	98

# List of Figures

1.1	Local coupling and long-range correlation . . . . .	4
1.2	Ferromagnetic and anti-ferromagnetic Ising model . . . . .	6
2.1	Golden Gate assembly . . . . .	20
2.2	Gibson assembly . . . . .	21
3.1	Ising-like interactions in a growing population obtained from the CP-IM simulations . . . . .	39
3.2	Power-law decay of the spatial autocorrelation function in simulated ferromagnetic population . . . . .	42
4.1	Two-state and coupled SGNs . . . . .	44
4.2	Behaviour of the two-state and coupled SGNs in a well-mixed population . . . . .	47
4.3	Induction of red and green fluorescence by C6HSL in colonies of rod-shaped cells carrying different versions of the reporter vector . .	53
4.4	Self-organized patterns of red and green cellular states generated in colonies of ferromagnetic and anti-ferromagnetic rod-shaped cells . .	55
4.5	Induction of red and green fluorescence by C6HSL in colonies of spherical cells carrying different versions of the reporter vector . . .	57
4.6	Ising-like patterns generated in colonies of spherical cells carrying the ferromagnetic and anti-ferromagnetic gene networks . . . . .	59
4.7	Hamming distance between ferromagnetic colonies of spherical cells and ferromagnetic populations obtained from CP-IM simulations . .	61
4.8	Cellular state patterns generated by the coupled two-state systems .	62
4.9	Patterns of cellular state domains in colonies of spherical cells without coupling mechanisms . . . . .	62
4.10	Cellular state switch in ferromagnetic colonies grown on solid medium supplemented with the inhibitor of the repressors . . . . .	63
4.11	Spatial autocorrelation function of colonies carrying the two-state and coupled gene networks . . . . .	65
4.12	Ferromagnetic system at the percolation threshold . . . . .	68
5.1	The mother machine . . . . .	70
5.2	The mother machine with two side channels . . . . .	71
5.3	Scanning Electron Microscopy images of the mother machine with side channels . . . . .	72



---

5.4	Behaviour of ferromagnetic and anti-ferromagnetic cells in the mother machine with side channels . . . . .	74
5.5	Ferromagnetic and anti-ferromagnetic cells growing inside the growth channels of the classic mother machine . . . . .	76
A.1	Colonies of rod-shaped <i>E. coli</i> cells carrying the ferromagnetic system with reporter vector 1 or 2 . . . . .	92
A.2	Colonies of rod-shaped <i>E. coli</i> cells carrying the anti-ferromagnetic system with reporter vector 1 or 2 . . . . .	93
A.3	Colonies of spherical <i>E. coli</i> cells carrying the ferromagnetic system with reporter vector 1 or 2 . . . . .	94
A.4	Colonies of spherical <i>E. coli</i> cells carrying the anti-ferromagnetic system with reporter vector 1 or 2 . . . . .	95

# List of Tables

2.1	Thermal cycling conditions for colony PCR amplification . . . . .	17
2.2	Thermal cycling conditions for Phusion DNA Polymerase-mediated PCR amplification . . . . .	18
2.3	Thermal cycling conditions for Golden Gate assembly . . . . .	21
4.1	<b>Reporter vector.</b> Biological parameters that characterize the binding of C6HSL and C12HSL to the <i>mCherry2</i> and <i>sfGFP</i> promoters in cells carrying the reporter vector. . . . .	49
4.2	<b>Ferromagnetic system.</b> Biological parameters that characterize the binding of C6HSL and C12HSL to the <i>mCherry2</i> and <i>sfGFP</i> promoters in cells carrying the ferromagnetic system. . . . .	49
4.3	<b>Anti-ferromagnetic system.</b> Biological parameters that characterize the binding of C6HSL and C12HSL to the <i>mCherry2</i> and <i>sfGFP</i> promoters in cells carrying the anti-ferromagnetic system. . . . .	49
4.4	Length constants of ferromagnetic and anti-ferromagnetic colonies of rod-shaped and spherical <i>E. coli</i> cells. Values correspond to the mean $\pm$ the standard deviation (in $\mu\text{m}$ ) of the sACF of around 40 colonies for each system. . . . .	66

# Abbreviations

<b>HSL</b>	Acyl-homoserine lactone
<b>SGN</b>	Synthetic genetic network
<b>DNA</b>	Deoxyribonucleic acid
<b>PCR</b>	Polymerase chain reaction
<b>TU</b>	Transcriptional unit
<b>CDS</b>	Coding sequence
<b>3OC6HSL</b>	3-oxo-C6-homoserine lactone
<b>3OC12HSL</b>	3-oxo-C12-homoserine lactone
<b>GFP</b>	Green fluorescent protein
<b>RFP</b>	Red fluorescent protein
<b>sACF</b>	Spatial autocorrelation function
<b>SOC</b>	Self-organized criticality
<b>IPTG</b>	Isopropyl $\beta$ -D-1-thiogalactopyranoside
<b>ATC</b>	Anhydrotetracycline
<b>PDMS</b>	Polydimethylsiloxane
<b>OD</b>	Optical density
<b>BSA</b>	Bovine Serum Albumin
<b>ON</b>	Overnight

# Chapter 1

## Introduction

### 1.1 Spatial patterns of gene expression in multicellular systems

The generation of coherent gene expression patterns has been a subject of extensive research in Developmental Biology, with an emphasis on cell differentiation in multicellular eukaryotic tissues [1]. Understanding the mechanisms underlying the formation of gene expression patterns in spatially arranged cellular systems is a long-standing challenge in Biology, and several models that combine mechanical and chemical interactions between cells have been elaborated. Most of these models are based on the generation of morphogen gradients, which are locally produced signaling molecules that can activate different and specific cellular process depending on their concentration [2, 3]. Two models based on the generation of morphogen gradients have been predominantly used to explain multicellular pattern formation: the “French flag model”, which is based on a previously defined gradient of morphogens that activate the differential expression of genes depending on the concentration to which cells are exposed [4–6]; and the reaction-diffusion model, which is based on the formation of self-organized spatial patterns of two locally produced opposing signals (an activator and an inhibitor with differential diffusion) that interact to generate patterns [7–9].

Systems composed of many cells can also undergo order generation by mechanisms that seem to be more elementary than the establishment of morphogen gradients or higher order molecular networks. In this sense, the generation of gene expression patterns also takes place during the emergence of different distributions of cellular states based on cell-cell coupling [10–16]. For instance, social interactions of bacteria significantly affect the dynamics of a community, and different spatial structures emerge from bacterial communities with different social interactions [10]. Another example of cell-cell interactions that allow the generation of ordered structures in multicellular populations are metabolic syntrophic exchanges that emerge between different cellular states in an initially homogeneous population. These cross-feeding interactions and gene expression correlations are established due to the diffusion of metabolites, in which different nearby populations exchange metabolites that they cannot synthesize [11, 17]. Gene expression correlations emerge even inside a population of genetically identical bacteria [13, 18, 19], where different sub-population of cells specialize on complementary metabolic pathways. For example, sub-populations of cells with different cellular states emerge in isogenic colonies of *E. coli* depending on the position of cells within a colony [12]. In this case, cells in the interior of the colony and close to the nutrient medium are able to ferment glucose to acetate, which is consumed by a second sub-population of cells in the surface of the colony. A similar behavior was observed in *B. subtilis*, where cells in the interior of a biofilm produce ammonium, which is consumed by a sub-population of cells in the periphery of the biofilm [14]. These type of correlations at the level of gene expression can emerge both in large colonies in a nutrient-rich environment and in a small population of cells in a nutrient-poor environment [18].

## 1.2 Positive and negative spatial correlations of gene states

The emergence of spatially-correlated structures is a phenomenon that pervades biology from molecular to ecological scales (e.g. [7, 20–23]), and a classical example is the self-organization of positive and negative spatial correlations of gene states in eukaryotic tissues and microbial communities [6, 12, 13, 19, 24, 25]. For instance, negative spatial correlations (neighbours having different phenotypes) can emerge during eukaryotic cell differentiation (e.g. Notch-delta [26]) and metabolic cross-feeding in microbial systems [27]. Positive gene spatial correlations (neighbours having the same phenotypes), on the other hand, are important for synchronizing growth and sharing resources in isogenic bacterial systems (e.g. [14, 16]). These correlations can occur either at short-range or at the scale of the whole populations [16, 19], and short-range correlations in gene expression (at the scale of few cells) have been attributed to shared lineage history and spatial proximity effects due to local gradients of nutrients and metabolites [28]. In this sense, while microbes are constantly adjusting their metabolism to ever-changing environments and nutrient conditions, they can also collectively modify their environment. Specifically, in a dense and spatially structured environment, local steep gradients of metabolites of only few cells of length are generated as cells consume and release compounds [18, 27]. The generation of these gradients of metabolites give rise to different sub-populations of cells with different metabolic states, allowing that a seemingly homogeneous population can become spatially structured. This means that the phenotype of a cell mostly depends on the population context in which it grows [19], where the generation of local micro-environments provides feedback control onto the genetic networks controlling the uptake and release of metabolites.

The diverse repertoire of short-range, long-range, positive and negative correlation patterns can emerge from a wide range of different mechanisms. Regardless of the particular sources, developing a common theoretical framework and a minimum experimental test-bed to study the scaling properties of these gene expression patterns could shed light to fundamental problems in biology, with

promising applications to the engineering of spatially-arranged cellular systems [1, 29–33]. An open question is whether a local coupling between metabolic networks could also lead to longer range correlations in gene expression, i.e. beyond the scale of coupling gradients, as schematically depicted in Fig. 1.1.

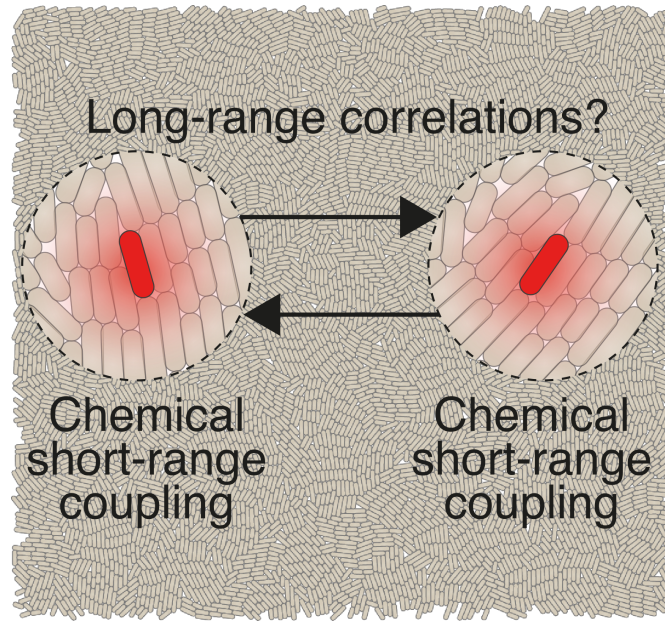


**Figure 1.1: Short-range coupling and long-range correlation.** Schematic representation of whether a local chemical interactions between neighbouring cells can generate long-range patterns of correlations in gene expression

### 1.3 General models for pattern formation in multicellular systems: The Ising Model

The understanding of how local interactions between cells can lead to the emergence of a spatial organization of gene expression requires a theoretical framework able to link individual gene network dynamics at a local scale to spatial state configurations at the population level. Since generally it is difficult to embrace the full repertoire of components and dynamics underpinning the functioning of real systems, one way to gain knowledge of complex systems is the use of abstract models to study their properties and capture essential information of the system. In this sense, understanding how macroscopic order arises from microscopic rules of local interactions in large systems has been a thoroughly studied problem in Physics,

and one important model in Statistical Mechanics is the Ising model. Originally designed to understand the sudden loss of magnetism in ferromagnetic materials as temperature increases [34], the Ising model provides a mathematical machinery able to address how macroscopic long-range correlations (and anti-correlations) emerge from the local interaction of two-state particles, allowing to study how discrete changes at local level suddenly lead to major changes, known as phase transitions. This model allows the understanding of complex emergent phenomena without the need of a detailed description of the parts of the system, since the interactions between the parts are more important than their details [35]. Interestingly, the Ising model has been widely applied to biological systems, and it has been specially useful in the study of spatial patterns in Biology at the molecular and ecological scale (see section 1.4). In the classical Ising model, the 2D space is divided in a square lattice of  $N$  sites with each site occupied by a discrete variable denominated spin ( $\sigma$ ). Each spin, which represents a magnetic moment in ferromagnetic materials, has a fixed location on the lattice (labeled by the index  $i$ ), can take one of two possible orientation values denoted by  $\sigma = \pm 1$ , and can only interact with their nearest neighbour (north, south, east and west in a 2D lattice) (Fig. 1.2A), with a total energy determined by the Hamiltonian

$$\mathcal{H} = -J \sum_{\langle ij \rangle}^N \sigma_i \sigma_j - h \sum_i \sigma_i \quad (1.1)$$

where  $\langle ij \rangle$  means that only the interaction between nearest neighbour spins are considered,  $J$  is the contribution to free energy made by the coupling interaction between these neighbour spins  $i$  and  $j$ , and  $h$  is the magnitude of an externally applied magnetic field acting on each spin of the lattice. A fundamental property of the Ising model is that the system always tries to reach a state of minimum energy. In absence on an external magnetic field ( $h = 0$ ), Equation 1.1 shows that the configuration that minimizes the energy of the system depends on the value of  $J$ : if  $J > 0$ , the interaction energy is minimized when neighbours spins align (have the same orientation) with each other, and the system is called ferromagnetic; if  $J < 0$ , the system is called anti-ferromagnetic and the energy



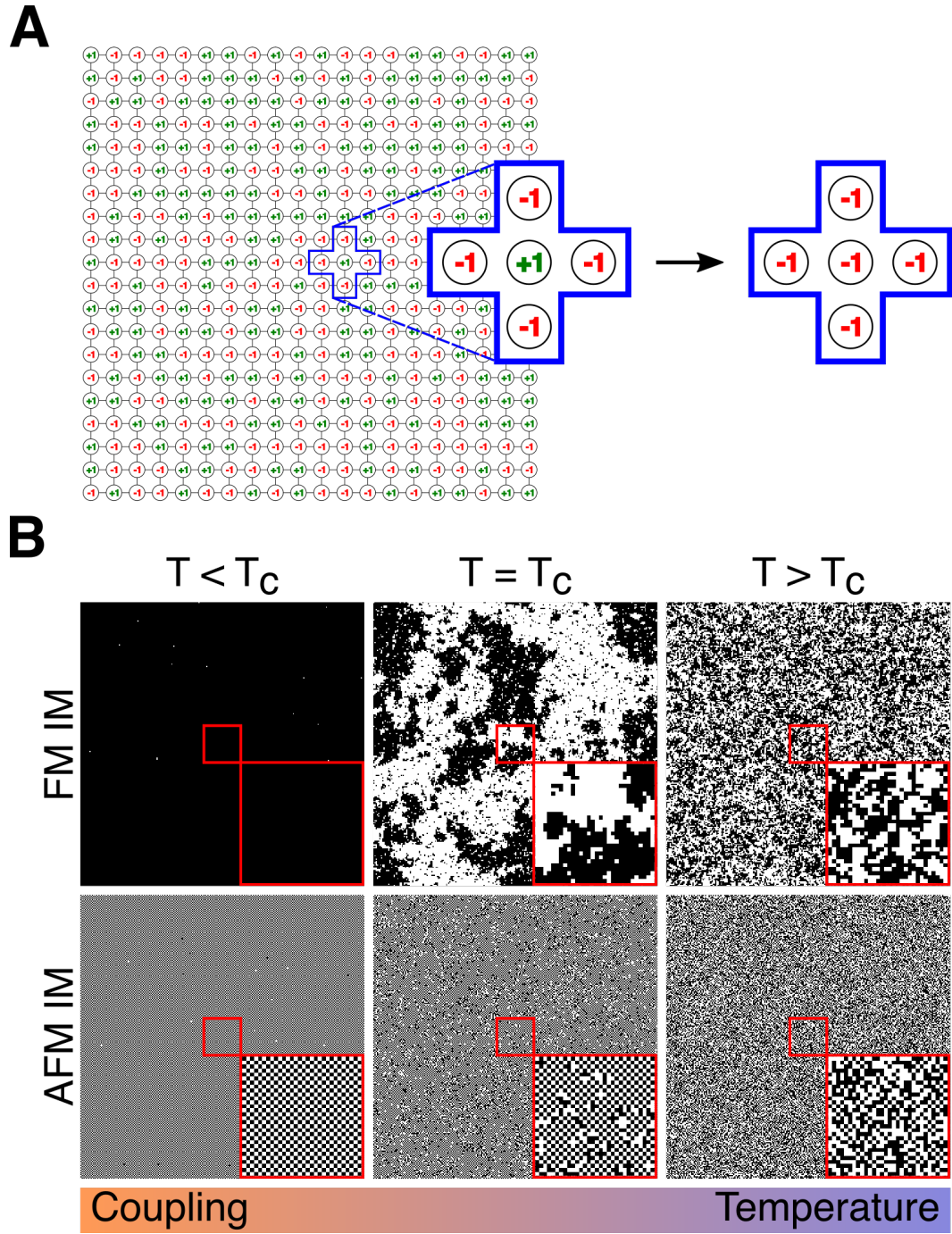


**Figure 1.2: Ferromagnetic and anti-ferromagnetic Ising Model.** (A) Schematic representation of a spin configuration of the 2D ferromagnetic Ising model on a square lattice, highlighting the interaction of a spin with its four nearest neighbours and the change in its orientation due to the minimization of the interaction energy. Spins are represented as red  $-1$  and green  $+1$ . (B) Numerical simulations of the two-dimensional ferromagnetic (FM IM) and anti-ferromagnetic (AFM IM) Ising model on a  $250 \times 250$  lattice at different temperatures  $T$  relative to the critical temperature  $T_c$ . White and black squares represent the spin orientations  $\sigma = \pm 1$ , which is determined by two opposite effects: the temperature and the coupling between spins. Insets correspond to a magnification of a  $30 \times 30$  square in the center of the images

is minimized when neighbour spins have the opposite orientation. The parameter that accounts for the degree of alignment of the spins, and thus the order of the system, is the magnetization per site ( $M$ ), which is defined as

$$M = \frac{1}{N} \sum_i^N \sigma_i \quad (1.2)$$

where  $N$  is the number of sites in the lattice. Thus, the magnetization per site is the average value of the spin. When most of the spins have the same orientation the value of  $|M|$  is close to 1, defining an ordered state of the system, while when all the spins are randomly distributed in the lattice the value of  $|M|$  is close to 0 and the system is in a disordered state. In the classical Ising model, two opposite effects determine the orientation of the spins on the lattice: the minimization of the interaction energy (Eq. 1.1), which allows spins to tend to align their orientations with those of their neighbours, and the thermal fluctuations, which tend to randomize the orientation of spins [36] (Fig. 1.2B). Thus, the parameter that determines the value of  $M$ , and therefore the balance between order and disorder, is the temperature of the system  $T$ . The probability  $P$  that (in equilibrium) the system is in a certain spatial configuration of spins  $\sigma$  depends on the energy of that configuration and the value of  $T$ , and this probability is given by the Boltzmann distribution:

$$P(\sigma) = \frac{e^{-\mathcal{H}(\sigma)/k_B T}}{Z} \quad (1.3)$$

where  $Z$  is the partition function  $Z = \sum e^{-\mathcal{H}(x)/k_B T}$  (sum over all possible configurations),  $\mathcal{H}(\sigma)$  is the energy of that configuration,  $k_B$  is the Boltzmann constant, and  $T$  the absolute temperature. In Equation 1.3  $T$  acts as an external control parameter of the configuration probability  $P(\sigma)$ : at low temperature, only the configurations that have low energy have a high probability; at high temperature, configurations of high and low energy have the same probability. Thus, equations 1.1 and 1.3 show the contribution of spin coupling  $J$  and temperature  $T$  to the probability distribution of spatial configurations. For a given coupling force

$J$ , varying the temperature  $T$  determines the transition through ordered, critical and disordered configurations of the system (Fig. 1.2B).

In a ferromagnetic system, at low temperatures ( $T < T_c$ ) the spins tend to align their states with those of their neighbours since the minimization of the interaction energy between spins prevails in the system. The tendency of spins to align with their neighbours eventually leads to only one spin orientation dominating the lattice (Figure 1.2B top left), and thus  $|M|$  is close to its maximum value of 1 (the ordered phase). At high temperatures ( $T > T_c$ ), the minimization of the interaction energy between spins become less relevant since the thermal fluctuations dominate the system. At this point, high energy configurations are equally probable as low energy configurations, and spins are equally likely to adopt either orientation, regardless of the orientation of their neighbours. The randomization of the spin orientations lead to a lattice with a noise-like appearance (Figure 1.2B top right), in which the value of  $M$  is zero (the disordered phase). Near a critical value of  $T$  ( $T = T_c$ ), spins are neither aligned nor random, and the system exhibits a second-order phase transition. At this critical point the configuration of the lattice becomes fractal (scale invariant), with clusters of spins with the same orientation of all sizes forming and disappearing over time (Figure 1.2B top middle) [36]. A similar behavior can be observed in an anti-ferromagnetic system, with an ordered phase at  $T < T_c$  (Figure 1.2B bottom left) and a disordered phase at  $T > T_c$  (Figure 1.2B bottom right). However, in the anti-ferromagnetic system the interaction energy is minimized when spins have the opposite orientation of their neighbours. This means that in the ordered phase the anti-aligning of spins is favored, resulting in a checkerboard-like pattern (a black square surrounded by four white squares and vice versa). As in a ferromagnetic system, at  $T = T_c$  spins are neither aligned nor random, and the system is composed of clusters of checkerboard-like patterns separated by disordered regions (Figure 1.2B bottom middle).

## 1.4 The Ising Model in biological systems

Different studies have demonstrated the applicability of the Ising model to the study of the spatial organization of biological processes at different scales. Studying the propagation of allosteric states in large multiprotein complexes, Bray et al. showed that arrays of closely packed units can show large-scale integrated behavior since the combined energy of two adjacent units with the same conformation is lower than the energy of two adjacent units with different conformations [21]. The coupling between units causes that the conformation of each unit influence the conformation of its neighbour, spreading throughout the entire system in a mechanism denominated conformational spread. As in the Ising model, this mechanism, which assumes energetic coupling between neighbour units, is based on two assumptions: a) each unit of the system can exist in one of two conformations and undergoes a conformational changes, and b) coupling between neighbouring units favors a coherent configuration, leading to the propagation of conformational changes [22].

At a cellular level, Wioland et. al showed that geometrically confined suspensions of the swimming bacteria *Bacillus subtilis* can spontaneously organize in phases of magnetic order. They constructed different microfluidic devices composed of a lattice of identical circular cavities connected with each other. The geometry of each cavity allowed the formation of a stably circulating vortex of bacteria, defining a clockwise or anti-clockwise bacterial current (the vortex spin). The lattices of bacterial vortices coupled hydrodynamically showed to organize spontaneously into patterns characterized by ferromagnetic and anti-ferromagnetic order [37], where the coupling between adjacent bacterial vortices can be controlled by changing the size of the gap connecting the cavities. These observations suggested that theoretical concepts used to describe magnetism can capture the essence of microbial behaviours in complex environments. Another *in silico* study at the cellular level suggested that the introduction of a genetic circuit that allows a dipole-like behaviour with coupling states between cells could induces second order phase transitions that coordinates the behaviour of bacterial cell ensembles [38]. Using numerical simulations, Weber et. al showed that as a function of the

transport rate of quorum sensing molecules across the membrane a population of cells can undergo spontaneous symmetry breaking from a state in which each cell can switching its phenotype independently to a global collective organization.

In addition, the Ising model has also been used to explain biological processes taking place at much larger scales. Inspired by the conceptual clarity of this model, Wang et. al constructed a two-dimensional lattice model that captures essential features of the follicle alignment system during the self-organization of mammalian hair patterning [39]. Studying several spatial models of single-species populations with local dispersal and uncorrelated environmental noise, Noble et. al showed that short-range dispersal of populations allows the emergence of long-range synchronization in a two-cycle oscillating ecological systems over distances much longer than the dispersal scale and in absence of environmental correlation (the Moran effect [40]). As in the Ising model, the space was divided in a lattice composed of habitat patches in which the local spin variable correspond to a local two-cycle amplitude of population density defined at each habitat patch. The results of this work suggest that spontaneous emergence of ecological boundaries between habitat patches with opposite synchronization can occur in different ecological systems with local dispersal and environmental noise [41]. Another example of spatial correlations in cyclic dynamics as the result of endogenous factors can be observed in the annual nut production in a plantation of pistachio trees, in which the seed production can be described by a two-cycle alternating of years of high and low production. Using 5 years of data obtained from a pistachio orchard, Noble et. al showed that the spatial patterns of tree yield can be explained by endogenous forces in analogy with the Ising model [20]. In this case, short-range interactions between trees, such as root grafting, can lead to long-range correlations in the spatial patterns of annual nut production over space and time, even in the presence of large environmental variability .

These studies have shown that local coupling between cycling or two-state processes leads to long-range correlations in biological systems, suggesting that these two features (i.e. local coupling and two-states) would be sufficient

for the generation of self-organized patterns of positive or negative correlations in two-dimensional arranged systems.

## 1.5 Synthetic biology as a tool for studying pattern formation

Experimental verification, as well as the engineering applications of models of gene expression patterning and spatial correlation is challenging because natural gene networks are embedded in complex physiological contexts that make difficult to disentangle essential mechanisms from hidden interactions [42–44]. Since removing the underlying context in natural biological systems is impossible, an alternative to study gene spatial correlations is the generation of synthetic bacterial systems. In this sense, Synthetic Biology offers the possibility of building minimal synthetic genetic networks (SGNs) that incorporate essential features of the process under study, providing a test-bed in which mechanistic processes can be isolated as much as possible from cellular processes and characterized in detail [45–47]. Synthetic Biology applies engineering design principles of modularization, rationalization and modelling to guide the design process of artificial biological systems [47, 48]. The construction of the first genetic circuits, the toggle switch [45] and the “repressilator” [46], showed that engineering principles could be applied to the construction of biological systems that could be analyzed and tested in isolation. Next, bigger building blocks were created to implement system-level synthetic circuits [49] to encapsulate more advanced elementary functions that could be parametrized and abstracted in computational models more easily [50]. The use of efficient DNA fabrication, well-characterized components and mathematical modeling has enabled the engineering of SGNs of unprecedented scale and predictability. In this sense, Nielsen et al. recently developed an environment in which users writes a code (representing logic gate circuits) that is automatically transformed into functional DNA circuits thanks to a better abstraction and increased reliability of the building blocks employed [50]. This reliability has provided more

tractability to microbial engineering practices [30–33], as well as enabled more control and analytical power to hypothesis-driven studies in cell biology, ecology and developmental biology [45, 46, 51–55]. A growing interest in engineering biological patterns has created new frontiers of interdisciplinary research that employ minimal and reconfigurable synthetic gene networks [42, 52, 53, 56–60]. These efforts could be instrumental for defining a common theoretical ground for the spatial biology of SGNs.

Generally, Synthetic Biology uses bacteria as model organisms, and despite being considered single-cell organisms, they are able to self-organize at the population level [61–65], displaying many features characteristics of multicellular organisms such as cellular differentiation, cell-cell communication and the formation of spatial structures [66]. These features make bacteria a useful model system to identify the underlying principles of the emergence of gene expression patterns in multicellular organisms. Despite these advances, engineering at single cell scale have encountered different limitations, such as crosstalk interactions, metabolic burden and genetic instability, limiting the implementation of more complex circuits within single cells [43, 49]. Engineering distributed instructions at a population level have appeared as a solution [67–69]. Different circuits at multicellular level have been developed, in which populations of cells interact to give rise to more complex behaviors [54, 57, 70–75]. The spatiotemporal pattern formation mediated by these and other circuits also provides a new tool for discovering fundamental mechanisms of developmental processes [43, 76].

## 1.6 Orthogonal system for cell-to-cell communication

Intercellular signaling in both directions is crucial to create the interactions that allows the establishment of stable positive and negative spatial correlations of gene states in multicellular systems. The acyl homoserine lactone (AHL)-based quorum sensing systems found in different bacteria provide components for the generation

of synthetic circuits for cell-cell communication. These signaling systems are composed of two core proteins: a LuxI-type protein (the AHL synthase), which synthesizes small molecules of AHL that can freely diffuse and increase its concentration as population density increases, and a LuxR-type protein (the response regulator), which binds AHL molecules and activates the transcription of genes [77]. Despite its usefulness, the use of multiple AHLs in the same circuit is challenging due to the different types of crosstalk that exist between different systems (i.e. functional interactions between components of the quorum sensing machinery that are not naturally paired). For example, the receiver proteins (LuxR-type proteins) can bind not only their cognate signal molecules, but also AHLs from other species (signal crosstalk), and these receiver proteins can also activate non-naturally paired promoters (promoter crosstalk) [78]. In order to generate an orthogonal cell-cell communication circuit using the quorum sensing system based on AHL, Grant et al. used the *Vibrio fischeri* LuxR [79] and *Pseudomonas aeruginosa* LasR [80] receptor proteins, which recognize 3-oxo-C6-homoserine lactone (3OC6HSL) and 3-oxo-C12-homoserine lactone (3OC12HSL), respectively. By adjusting the expression levels of both receptor proteins and making base pair changes in their target promoters to minimize non-cognate receiver protein binding, they were able to reduce the crosstalk between the signaling molecules, generating a system capable of differentiating between two different AHL in the same cell, producing two different orthogonal responses [74].

## 1.7 Project rationale

Here, we apply a theoretical framework based on the Ising model and spatial biology to study the emergence of global gene expression correlations from SGNs able to acquire two states and interact locally by artificial cell-to-cell signaling in *Escherichia coli*. In analogy to the two-state interacting particles of the Ising model, we constructed synthetic toggle switches [45] whose states are coupled by the synthesis of two orthogonal AHL molecules [74]. Deciphering the generic mechanisms that link synthetic gene networks switching behavior to the global



distribution of states could shed light to the study of specialization and division of labor in bacterial communities e.g. [28, 81, 82], as well as provide instrumental guidance in the engineering of self-organized structures in multicellular systems, such as spatially-functionalized biofilms, structured bio-materials and artificially-patterned tissues.

## **1.8 Hypothesis**

Coupling between two cellular states allows the generation of self-organized spatial patterns in multicellular bacterial systems.

## **1.9 Objectives**

### **1.9.1 General Objective**

To study the establishment and maintenance of cellular-state patterns in bi-stable coupled systems.

### **1.9.2 Specific Objectives**

1. Use a spin model to study the behaviour of coupled two-state systems in a population of growing cells.
2. Design and construct synthetic bacterial systems that exhibit two states and coupling between them.
3. Study the fluorescent patterns generated by the coupled two-state systems in bacterial colonies.

# Chapter 2

## Materials and Methods

### 2.1 Computational modeling

The code for the simulation of the Ising model during the growth of a bacterial population was written in the C programming language, and it is described in Chapter 3.1.1. The graphical user interface was created with GTK+ 3 (<https://developer.gnome.org/gtk3/stable/>).

### 2.2 Bacterial strains and Growth conditions

All experiments were performed using the TOP10 One Shot™ (Thermofisher) or the KJB24 *E. coli* strains. KJB24 strain contains a stop codon mutation in the cell wall protein RodA, which results in the generation of spherical cells, and a second mutation that allows cells to grow in rich medium [83]. Cells of both TOP10 One Shot™ and KJB24 strains were made competent by the CCMB80 method ([http://openwetware.org/wiki/TOP10\\_chemically\\_competent\\_cells](http://openwetware.org/wiki/TOP10_chemically_competent_cells)), and 50  $\mu$ L aliquots of these competent cells were stored in 0.6 mL tubes at -80 °C.

Cells were grown on liquid LB medium (tryptone 10 g, yeast extract 5 g, NaCl 5 g, and distilled water to a final volume of 1 L) or liquid M9-glucose

medium (1x M9 salts supplemented with  $\text{MgSO}_4 \cdot 7\text{H}_2\text{O}$  2 mM,  $\text{CaCl}_2$  0.1 mM, glucose 0.4% and casamino acids 0.2%, where 1 L of 5x M9 salts contains 64 g of  $\text{Na}_2\text{HPO}_4 \cdot 7\text{H}_2\text{O}$ , 15 g of  $\text{KH}_2\text{PO}_4$ , 2.5 g of  $\text{NaCl}$ , and 5 g of  $\text{NH}_4\text{Cl}$ ). To prepare solid LB or M9-glucose medium, 1.5% w/v agar was added to the corresponding liquid medium. When necessary, both liquid and solid media were supplemented with 50  $\mu\text{g}/\text{mL}$  kanamycin, 100  $\mu\text{g}/\text{mL}$  carbenicillin, 50  $\mu\text{g}/\text{mL}$  spectinomycin or 10  $\mu\text{g}/\text{mL}$  chloramphenicol. In order to prepare the stock solutions of acyl-homoserine lactone molecules, 3-oxohexanoyl-homoserine lactone (C6HSL, Cayman Chemicals) and 3-oxododecanoyl-homoserine lactone (C12HSL, Sigma) were dissolved in DMSO to a concentration of 0.067 M. Before being used, both acyl-homoserine lactones were first diluted in ethanol to a concentration of 2 mM, and then diluted in M9-glucose medium to the described concentrations.

## 2.3 Molecular cloning

### 2.3.1 Bacterial transformation

To transform *E. coli* cells with plasmids, aliquots of competent cells were thawed on ice for 15 minutes, and then 1-5  $\mu\text{L}$  of DNA was added to the cells. The competent cell/DNA mixture was mixed gently by flicking the bottom of the tube, and incubated on ice for 15 minutes. The tubes were placed into a 42 °C water bath for 60 seconds, and then immediately on ice for 2 minutes. 250  $\mu\text{L}$  of liquid LB without antibiotic was added to the cells, and they were grown at 37 °C in a shaking incubator for 1 hour. 100  $\mu\text{L}$  of the transformed cells were plated onto LB agar plates containing the appropriate antibiotics. Plates were incubated at 37 °C overnight.

### 2.3.2 Selection of positive colonies by Colony PCR

To select colonies carrying plasmids with DNA fragments of interest, for each event of transformation, five colonies were picked with a pipette tip and resuspended in

10  $\mu\text{L}$  of nuclease-free water. For each colony, the following reaction was prepared: 5  $\mu\text{L}$  of 5x Green GoTaq Buffer, 2  $\mu\text{L}$  of 25 mM  $MgCl_2$ , 0.4  $\mu\text{L}$  of 10 mM dNTPs, 0.8  $\mu\text{L}$  of 10  $\mu\text{M}$  forward primer, 0.8  $\mu\text{L}$  of 10  $\mu\text{M}$  reverse primer, 0.1  $\mu\text{L}$  of GoTaq DNA Polymerase (Promega), nuclease-free water to 19  $\mu\text{L}$ , and 1  $\mu\text{L}$  of colony resuspended in water. The reactions were transferred to a thermocycler, and the fragments were amplified using the program detailed in the Table 2.1.

Step		Temperature	Time
Initial Denaturation		95 °C	10 minutes
35 Cycles	Denaturation	95 °C	45 seconds
	Annealing	60 °C	45 seconds
	Extension	72 °C	1 minute/kb
Final Extension		72 °C	5 minutes
Hold		4 °C	

**Table 2.1:** Thermal cycling conditions for colony PCR amplification

Next, 15  $\mu\text{L}$  of the reactions were loaded into 1% w/v agarose gels and electrophoresis was performed at 120 volts for 30 minutes. The bands of the PCR products were visualized on a blue LED transilluminator (iorodeo.com). Positive colonies (colonies with a band of the PCR product of an expected size) were grown overnight on liquid LB medium supplemented with the appropriate antibiotic. Glycerol stocks were made mixing 500  $\mu\text{L}$  of these cultures and 500  $\mu\text{L}$  of 50% glycerol in cryogenic tubes, and they were stored at -80 °C.

### 2.3.3 Generation of DNA fragments for Gibson assembly

To generate the DNA fragments used in the construction of vectors by Gibson assembly, fragments were amplified using the Phusion High-Fidelity DNA Polymerase. For each DNA fragment, the following reaction was prepared in a 0.2  $\mu\text{L}$  tube: 6  $\mu\text{L}$  of 5x Phusion buffer, 0.6  $\mu\text{L}$  of 10 mM dNTPs, 1.5  $\mu\text{L}$  of 10  $\mu\text{M}$  forward primer, 1.5  $\mu\text{L}$  of 10  $\mu\text{M}$  reverse primer, 0.3  $\mu\text{L}$  Phusion High-Fidelity DNA Polymerase (NEB), 1  $\mu\text{L}$  of template, and nuclease-free water to 30  $\mu\text{L}$ . As templates, purified vectors containing the desired fragment at a concentration of

approximately 1 ng/ $\mu$ L were used. The tubes were transferred to a thermocycler and the fragments were amplified using the program detailed in Table 2.2.

Step		Temperature	Time
Initial Denaturation		98 °C	30 minutes
35 Cycles	Denaturation	98 °C	10 seconds
	Annealing	60 °C	30 seconds
	Extension	72 °C	30 seconds/kb
Final Extension		72 °C	10 minutes
Hold		4 °C	

**Table 2.2:** Thermal cycling conditions for Phusion DNA Polymerase-mediated PCR amplification

The 30  $\mu$ L of the reactions were loaded into 1-1.5% w/v agarose gels and electrophoresis was performed at 100 volts for 45 minutes. The bands of the PCR products were visualized on a blue LED transilluminator (iorodeo.com) using SYBR Safe (Thermofisher), and the fragments were purified and quantified (Section 2.3.4).

### 2.3.4 DNA purification

The purification of DNA fragments from agarose gel was performed using the Wizard SV Gel and PCR Clean-Up System (Promega), according to the instructions of the manufacturer. After the purification, the concentration and quality of the DNA fragments were determined using a Synergy HTX plate reader (BioTek), and the fragments were stored at -20 °C.

To extract and purify plasmids from bacteria, cells stored in glycerol stocks carrying the desired vectors were inoculated into 5 mL of liquid LB medium supplemented with the appropriated antibiotics and grown overnight. The purification of the vectors was performed using the Wizard Plus SV Minipreps DNA Purification System (Promega) according to the instructions of the manufacturer. The purified plasmids were quantified using a Synergy HTX plate reader (BioTek) and were stored at -20 °C.

### 2.3.5 Plasmid construction

Plasmids used in this work were constructed using a combination of the Golden Gate Assembly [84] (Fig. 2.1) and Gibson Assembly [85] (Fig. 2.2) molecular cloning methods .

#### 2.3.5.1 Golden Gate assembly

Golden Gate assembly allows the simultaneous assembly of multiple DNA fragments (contained in Level 0 vectors) into a vector backbone using Type II restriction enzymes and T4 DNA ligase. All the Level 0 parts used in the Golden Gate assembly, which contain one of the four genetic elements that are part of a Transcriptional Unit (TU) (promoter, ribosome binding site (RBS), coding sequence (CDS), and terminator) (2.1), were obtained from the CIDAR MoClo kit [86] deposited in Addgene (Kit #1000000059), except the Level 0 parts containing the pLux76pTet promoter, the pLas81pLac promoter, and the mCheery2 CDS. These Level 0 parts were constructed by Gibson Assembly using gBlocks supplied by IDT (idtdna.com). The sequences of the pLux76 and pLas81 promoters were obtained from [74], while the sequence of *mCheery2* was obtained from [87].

To generate a Level 1 vector, which contains a complete TU (2.1), 4 Level 0 parts containing each part of a TU were combined with one of the four Level 1 destination vectors (12X, 23X, 34X, 45X). Thus, to construct a Level 1 vector through Golden Gate assembly, 10 fmol of the destination vector and 20 fmol of each Level 0 part were mixed in a total volume of 7  $\mu\text{L}$  in a 0.2 mL tube. 1  $\mu\text{L}$  of T4 DNA Ligase 10x (NEB), 1  $\mu\text{L}$  of T4 DNA Ligase 10 U/ $\mu\text{L}$  (NEB) and  $\mu\text{L}$  1  $\mu\text{L}$  of BsaI 20 U/ $\mu\text{L}$  (NEB) were added to the mix of DNA parts. The tubes were placed on a thermocycler, and the reactions were performed using the program detailed in Table 2.3.

*E. coli* competent cells were transformed using 5  $\mu\text{L}$  of the reactions, colonies generated were checked by colony PCR, and two positive colonies were

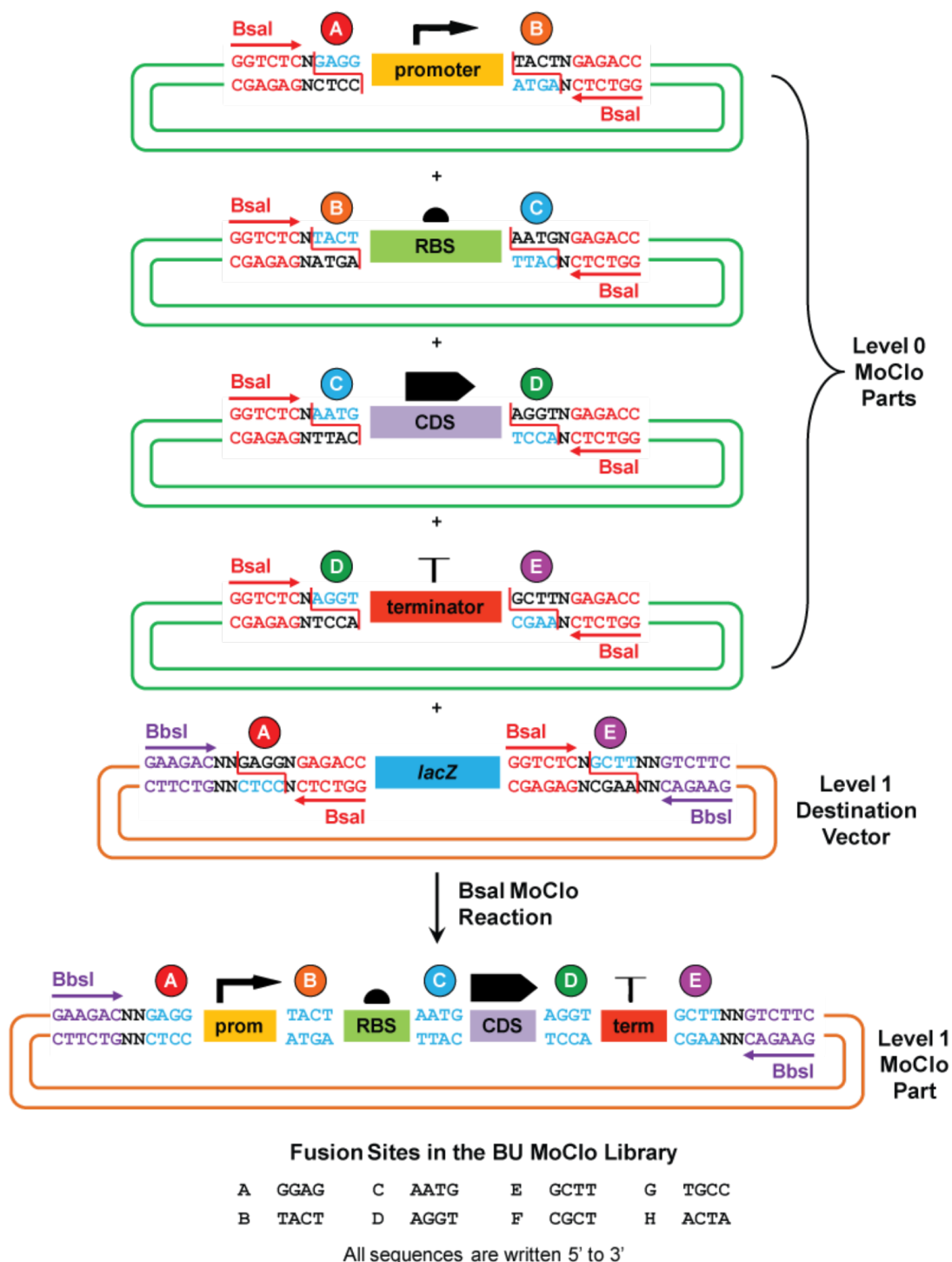


**Figure 2.1: Golden Gate assembly.** Schematic representation of the generation of a Level 1 vector using 4 Level 0 parts containing one of the four genetic elements that are part of a Transcriptional Unit (TU): promoter, ribosome binding site (RBS), coding sequence (CDS) and a Level 1 destination vector. Figure was obtained from <http://2013.igem.org/Team:BostonU/MoCloChara#>

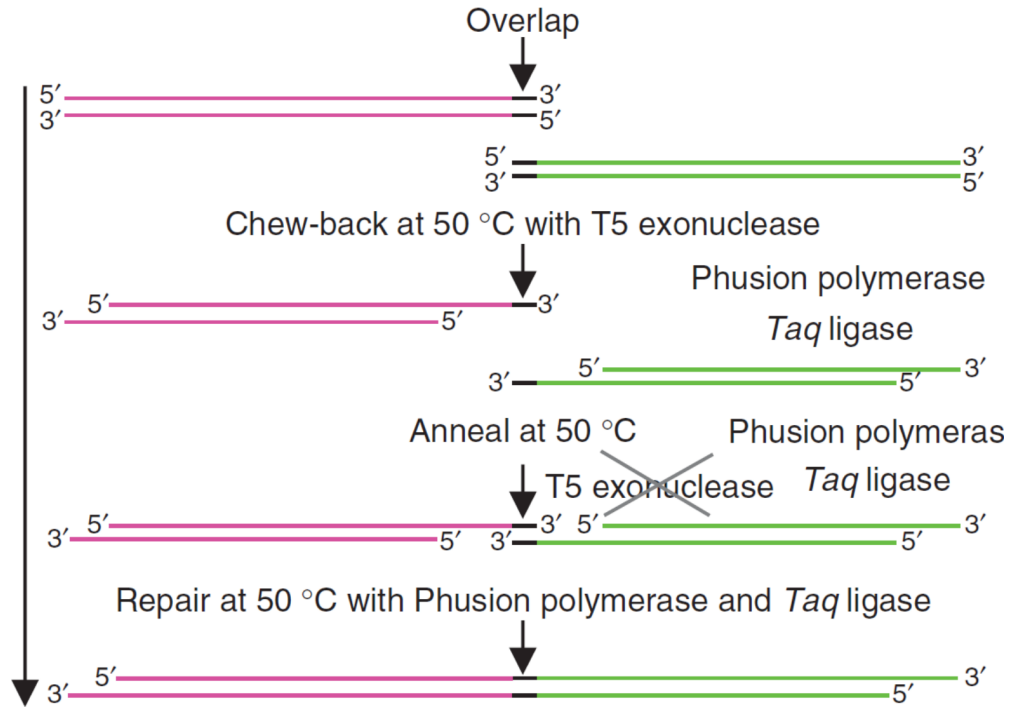


**Figure 2.2: Gibson assembly.** Schematic representation of the steps of Gibson assembly cloning, in which two DNA fragments are joined together in a one-step isothermal in vitro recombination by the action of a T5 Exonuclease, a Phusion DNA Polymerase, and a Taq DNA Ligase. Figure was obtained from [85].

Step		Temperature	Time
20 Cycles	Activation of BsaI	37 °C	2 minutes
	Activation of Ligase	16 °C	3 minutes
Inactivation of BsaI		50 °C	5 minutes
Inactivation of Ligase		80 °C	10 minutes

**Table 2.3:** Thermal cycling conditions for Golden Gate assembly

selected for sequencing. This methodology allowed the generation of a large number of different Level 1 vectors with a different combination of promoter, RBS, CDS, and terminator.

### 2.3.5.2 Gibson assembly

The construction of Level 0 vectors containing the mCheery2 CDS, pLux76pTet and pLas81pLac promoters, as well as Level 2 vectors, which contain different combinations of TUs from Level 1 vectors assembled by Golden Gate, was performed by Gibson assembly. This molecular cloning method consists in the use of three



enzymes (T5 Exonuclease, Phusion DNA Polymerase, and Taq DNA Ligase) in a single isothermal reaction to join multiple overlapping DNA fragments into a large DNA molecule (Fig. 2.2). After the amplification and purification of the DNA fragments (Section 2.3.3), for the assembly of multiple fragments into a vector, it is necessary to mix all the fragments in an equimolar ratio. Thus, the volume of each DNA fragment needed to prepare an equimolar mixture of fragments to be assembled was calculated using Equations 2.1, 2.2 and 2.3.

$$pmols\ fragment \left[ \frac{pmol}{\mu L} \right] = \frac{Concentration \left[ \frac{ng}{\mu L} \right] * 1000}{650 \left[ \frac{Daltons}{bp} \right] * Length [bp]} \quad (2.1)$$

$$Volume\ ratio\ of\ one\ fragment [\mu L] = \frac{X pmol}{pmols\ fragment} \quad (2.2)$$

$$Volume\ fragment = \frac{Final\ volume * Volume\ ratio\ of\ one\ fragment}{Sum\ of\ the\ volume\ ratios\ of\ all\ fragments} \quad (2.3)$$

Equation 2.1 allows the transformation of nanograms of DNA fragments into picomols. In this equation, *Concentration* correspond to the concentration of the fragments in  $\left[ \frac{ng}{\mu L} \right]$ , 1000 is the conversion factor from nanograms to picograms, 650 is the average molecular weight of a base pair (bp) in Daltons, and *Length* is the length of the DNA fragment in bp. Equation 2.2 allows to determine the volume ratio between DNA fragments using the picomols of the fragments ( $pmols\ fragment \left[ \frac{pmol}{\mu L} \right]$ ) and a factor *X*, which is 0.01 for fragments with more than 2500 bp, 0.03 for fragments between 200 bp and 2500 bp, and 0.05 for fragments with less than 200 bp. Equation 2.3 allows to calculate the volume (in  $\mu L$ ) to be added of each fragment to generate an equimolar mixture of DNA fragments. The *Final volume* corresponds to the total volume of the DNA fragment mixture, *Sum of the volume ratios of all fragments* is the sum of the volume ratios of all

the fragments to be assembled, and *Volume ratio of one fragment* is the volume ratio of each fragment.

Depending on the concentration of the fragments, 3 to 5  $\mu\text{L}$  of total volume of the mixture of DNA fragment was prepared. 1.5  $\mu\text{L}$  of this mixture of DNA fragments were transferred to a 0.2  $\mu\text{L}$  tube, and 4.5  $\mu\text{L}$  of a Gibson Master Mix, which contains isothermal buffer, T5 exonuclease (Epicentre), Phusion High-Fidelity DNA Polymerase (NEB), and Taq DNA Ligase (NEB) (<https://www.protocols.io/view/fabrication-of-dna-constructs-by-gibson-assembly-a-7r8hm9w?step=3>), were added to this mix of DNA fragments. The tubes were transferred to a thermocycler at 50 °C and were incubated at that temperature for 1 hour. To transform *E. coli* competent cells, the 5  $\mu\text{L}$  of the reactions were used. Colonies generated from this transformation were checked by colony PCR, and two positive colonies were selected for sequencing.

## 2.4 Plate fluorometry

*E. coli* cells stored in glycerol stocks were inoculated into 4 ml of liquid M9-glucose medium supplemented with the appropriate selective antibiotics, and the cultures were grown overnight in a shaking incubator at 37 °C. The overnight cultures were diluted 1:1000 in the same fresh liquid medium, and 200  $\mu\text{l}$  of these dilutions were transferred to a well of a 96-well clear-bottom plate. Depending on the experiment, each well was supplemented with different concentrations of one of the inducer molecules (C6HSL or C12HSL). The plates were placed in a Synergy HTX plate reader (BioTek) and fluorescence (sfGFP: 485/20 nm excitation, 516/20 nm emission; mCherry2: 585/10 excitation, 620/15 nm emission) and optical density (600 nm) were measured every 10 min for 24 hours. The plates were maintained at 37 °C during the experiment and were shaken at 200 rpm between readings.

## 2.5 Microscopy

To obtain images of bacterial colonies, *E. coli* cells stored in glycerol stocks were inoculated into liquid M9-glucose medium supplemented with the appropriate selective antibiotics, and these cells were grown overnight at 37 °C. The overnight culture was diluted 1:100 into the same fresh liquid medium, and cells were grown to an optical density (600 nm) of 0.2, diluted 1:1000 and 20  $\mu$ L of these dilutions were plated onto M9-glucose agar plates supplemented with the appropriate antibiotic and the described concentrations of C6HSL. Plates inoculated with TOP10 *E. coli* cells were incubated at 37 °C for 14 hours, while plates inoculated with KJB24 *E. coli* cells were incubated at 37 °C for 18 hours. A Nikon Ti microscope equipped with 10x, 20x and 40x objectives, and FITC and TRITC Filter Cube Sets were used to obtain the images of colonies and microfluidic devices. Images were acquired using the Nikon NIS-Elements BR software.

## 2.6 Image analysis

The processing and analysis of the images of the colonies were performed using the Fiji [88] distribution of ImageJ [89]. Single-channel images of the colonies were created by merging a z-stack using the Extended Depth Field plugin, while multi-channel images were merged using the Merge command. Before the analysis of the images, single-channel images were converted into 8-bits, the background was removed using the Subtract Background command and the images were binarized using the Automatic Threshold plugin. To investigate the possible existence of a characteristic spatial distribution of the cellular-state domains, we used the AutoCorrelation Function (ACF) plugin [90] (<http://www.vwalter.fr/resources/software/>) to calculate the spatial Autocorrelation Function (sACF) of the binarized images of whole colonies. A value of 1 or  $-1$  of the sACF means a perfect correlation or anticorrelation, respectively, while a value of 0 means no correlation. To calculate the mean size of the patterns generated in the colonies

we used Gnuplot (<http://www.gnuplot.info/>) to fit the data of the sACF to the one phase exponential decay equation

$$y = y_0 e^{-x/b} + c \quad (2.4)$$

where  $y$  is the value of the sACF,  $x$  is the distance in  $\mu\text{m}$ ,  $y_0$  is the value of  $y$  when  $x$  is zero,  $c$  is the value of  $y$  at infinite times, and  $b$  is the length constant, which correspond to the average size of the cellular states domains generated in the colonies.

To obtain the probability distribution of cluster sizes, we calculate the number and size of the clusters of binarized images of colonies and simulations using the Find Connected Regions Plugin of ImageJ (<http://homepages.inf.ed.ac.uk/s9808248/imagej/find-connected-regions/>). The slope of the plots of the probability distribution of the cluster size correspond to the scaling exponent  $\gamma$ .

To determine the similarity between ferromagnetic colonies and ferromagnetic populations obtained from CP-IM simulations, we calculate the Hamming distance using a custom Python program that determines the number of pixel positions in which the images are different. Binarized images were scaled to have the same number of pixels, saved as a binary array in a text file, and the Python program was used to compare each position in the array (which represents a pixel of the binarized image) of two images. If in that position both images have the same pixel value, the program adds a 0, but if the values are different, the program adds a 1. The total number of pixels in which the images are different is then divided by the total number of pixels to obtain the Hamming distance. For this analysis, 42 colonies of ferromagnetic cells with the reporter vector 1 and 65 colonies of ferromagnetic cells with the reporter vector 2 were compared with 10 simulated population for each value of the control parameter between 2 and 2.54. To find the smallest value of the Hamming distance between a colony and a simulated population, the image of the simulated population was rotated every 15 degrees,

generating a total of 24 versions for each simulated population. Thus, the final value of the Hamming distance corresponds to the smallest value obtained from the calculation of the distance between the colony and each version of the simulated population. One-way ANOVA followed by Dunnett's multiple comparisons test was performed using GraphPad Prism for Windows, GraphPad Software, San Diego, California USA, <http://www.graphpad.com>.

## 2.7 Microfluidic devices

### 2.7.1 Fabrication of the master mold of the mother machine

The design and fabrication of the mother machine was carried out in collaboration with Dr. Peter Galajda and members of his research group at the Biological Research Center in Szeged, Hungary. The microfluidic devices constructed in this work were designed using the KLayout software (<https://www.klayout.de/>), and the master molds were fabricated using soft lithography techniques [91]. Using SU-8 photoresists (MicroChem), we constructed the master mold of the mother machine in two steps: the first layer for the growth channels and the second layer for the central channel. To align these two layers during the fabrication process, chromium alignment marks were printed first in a silicon wafer (University Wafer, Inc). To print these marks, the wafer was first spin coated (1.3-1.5  $\mu\text{m}$ ) with the positive photoresist SU-8 S1818 (MicroChem). Then, the alignment marks were written into the photoresist using a laser pattern generator ( $\mu\text{PG}$  101, Heidelberg Instruments), and a layer of chromium was deposited to create the alignment marks. To fabricate the master mold of the mother machine, the wafer with the alignment marks was first spin coated with a layer (1.2  $\mu\text{m}$ ) of the negative photoresist SU-8 2002 (MicroChem) and the design of the first layer (the growth channels) was written into the photoresist. Next, the wafer was spin coated with a

layer (15  $\mu\text{m}$ ) of the negative photoresist SU-8 2015 (MicroChem) and the design of the second layer (the central channel) was written into the photoresist.

### 2.7.2 Fabrication of PDMS microfluidic devices

Once the master molds were created, we used polydimethylsiloxane (PDMS) for the fabrication of the devices. PDMS was prepared using the silicone elastomer kit Sylgard 184 (Dow Corning) by mixing the base (part A) and the curing agent (part B) in a 10:1 weight ratio. The uncured PDMS was degassed by centrifugation and poured onto the master mold. PDMS was cured at 65 °C for at least one hour, and the PDMS layer was carefully peeled from the silicon wafer. Individual devices were cut out from the PDMS using a surgical blade and holes for the inlets and outlets were made with a biopsy puncher (0.5 mm). To bond the PDMS devices to a glass coverslip, scotch tape was used to remove dust and dirt from the surfaces of the devices and coverslips, and the side of the PDMS with the design and the glass coverslips were plasma cleaned using a plasma oven. The patterned side of the PDMS devices and the glass coverslip were joined together and incubated at 65 °C overnight to let them bond. Devices constructed in this way were loaded with cells using a syringe. To prevent cell adhesion to the PDMS surface, 0.1% of bovine serum albumin (BSA) was added to the culture prior to the injection of cells into the device. The tubes that allow the entry of fresh medium and the exit of the wastes were connected to the device, and the device was placed under the microscope to take pictures every 10 minutes.

# Chapter 3

## Computational Modeling

### **3.1 Use a spin model to study the behaviour of two-state and coupled systems in a population of growing cells**

#### **3.1.1 Simulation of the Ising model during the growth of a bacterial population**

As seen in Chapter 1, the Ising model explicitly captures potential mechanisms for controlling the generation of patterns of gene spatial correlations and anti-correlations in spatially arranged cellular systems. To study the effects of Ising-like mechanisms in a growing population of cells, we created a lattice model that embodies cell population dynamics and Ising model-based rules for cell state differentiation. We combined the simulation of the two-dimensional Ising model using the Metropolis algorithm [92] with the Contact Process lattice model [93] to represent cell population dynamics, and we name this model CP-IM (Contact Process - Ising Model). This model consists of an interacting particle system which follows colonization, extinction and differentiation dynamics of particles on a bi-dimensional lattice ( $\mathcal{L}$ ) of  $N$  sites. Each site of this lattice can be in one of four

states  $S = \{\emptyset, *, -1, +1\}$ , which represent vacant locations ( $\emptyset$ , white squares), locations occupied with undifferentiated cells ( $*$ , black squares), and locations occupied with differentiated cells in red ( $+1$ , red squares) or green ( $-1$ , green squares) state. The state of a site  $x$  at a time  $t$  can be described as  $\xi_t(x)$ . Thus, an interacting particle system  $\xi_t : \mathcal{L} \rightarrow S$  (that assign one states from  $S$  to all sites in the lattice) is determined by the following lattice reactions that combine two sets of processes:

*i)* Birth, death, colonization and differentiation processes: cells can die or survive at rates  $\delta$  and  $b$ , respectively. If they survive, they divide and give birth to daughter cells that can occupy only nearest (north, south, east and west) vacant sites in the lattice, originating an advancing front of growing cells that colonizes available habitat in the landscape. This spatial spread is represented by  $\emptyset_x + *_y \rightarrow *_x + *_y$ , while cell death is represented by  $*_x \xrightarrow{\delta} \emptyset_x$ . Colonization only occurs between nearest neighbours  $\|x - y\| \leq 1$  for  $x, y$  representing sites on the lattice  $\mathcal{L}$ . At the beginning of the simulation, an undifferentiated cells is placed in the center of the lattice. Then, a site on the lattice is randomly selected, and if this focal site is vacant, a random neighbour is selected. If this neighbour of the focal site is occupied, it colonizes the vacant site with probability 1. On the other hand, if the focal site is occupied by a undifferentiated cell ( $*$ ), it can differentiate into a red ( $+1$ ) or green ( $-1$ ) state at a certain rate  $\alpha$ , which is represented by  $*_x \xrightarrow{\alpha} +1_x$  and  $*_x \xrightarrow{\alpha} -1_x$ . These differentiated cells can also die or give birth to daughter cells with the same rates  $\delta$  and  $b$ .

*ii)* Ising-like cellular states alignment process: To determine if differentiated cells can change from one state to another (red to green or green to red), a site in the lattice occupied by a differentiated cell is randomly selected and the change in the interaction energy  $\Delta\mathcal{H}$ , which results if the state of the cell at that site is changed, is calculated using the Equation 1.1. The notation  $\langle ij \rangle$  in this equation indicates that the sum is between neighbouring pairs of cells, allowing only a short-range interaction between cells. For the interaction energy calculations, we assumed that  $J = +1$  for ferromagnetic systems and  $J = -1$  for anti-ferromagnetic systems. This assumption implies that the interaction energy



between neighbouring cells is minimized when they have the same state in a ferromagnetic system, or the opposite state in an anti-ferromagnetic system (Eq. 1.1). Thus, if  $\Delta\mathcal{H} < 0$ , the change in the state is accepted since this change decreases the total energy of the system. If  $\Delta\mathcal{H} \geq 0$ , which means an increase in the total energy of the system, the change in the state is accepted only if  $r < e^{-\Delta\mathcal{H}/k_B T}$ , where  $r$  is a random number such  $0 < r < 1$  [94]. In the classical Ising model,  $T$  is the absolute temperature, and correspond to the control parameter. This means that varying  $T$  determines the transition between ordered and disordered configurations of the system. Since we are interested in studying the emergence of gene correlations due to the coupling of cells, in our model  $T$  represents a parameter that determines the coupling strength between cells in the system.

In this model, one generation time corresponds to the moment when all the sites in the lattice have had the possibility of being visited. In a 250x250 lattice, we run simulations for 200 generation times. It is also important to note that a lattice site in the CP-IM simulations can have two interpretations. As described above, a lattice site in the CP-IM simulations can represent a cell. However, a lattice site in this model can also represent a cell territory. Considering lattice sites as cellular territories is particularly relevant since it allows to map a lattice site to a sector in a colony. In this interpretation, beside considering lattice sites as cell territories (and not individual cells), the death rate represents the clearance rate of territories, and the division/birth rate represents the local colonization rate. However, the usefulness of the model remains the same: local interactions can give rise to large scale order.

## 3.2 C Code of the CP-IM simulations that combines the Contact Process and the Ising Model

The next pages contain the code for the simulation of the Ising model during the growth of a population of cells (CP-IM simulations). This code was written in the C programming language, and the graphical user interface was created with

GTK+ 3 (<https://developer.gnome.org/gtk3/stable/>).

---

```

1 //LIBS
2 #include <windows.h>
3 #include <stdlib.h>
4 #include <gtk/gtk.h> //GUI, Gtk Lib
5 #include "mt64.h" //pseudo Random Number Generation 64bit MT Lib
6 #include <math.h> //math to transform random n from continuous to discrete
7 #include <time.h> //time library to initialize random generator with time seed
8 #include <stdio.h>
9
10 //MACROS to later define a 2D Lattice of 250 x 250 sites
11 #define X_SIZE 250
12 #define Y_SIZE 250
13
14 //STRUCTURE with the simulation DATA
15 struct simulation
16 {
17     int lattice_configuration[X_SIZE][Y_SIZE]; //Lattice configuration
18     gint run; //Time handler tag. Standard C unsigned int type
19     gboolean running; //Are we running? should only contain the value TRUE or FALSE
20     gboolean initialized; //Have we been initialized?
21     int generation_time; //Generations simulated
22     double occupancy; //Lattice occupancy
23     float T; //Temperature
24     float J; //J
25 } s; //Instance s of the structure to hold the simulation
26
27 //Declare PUT PIXEL function to access individual pixel data on a Pixel Buffer
28 void put_pixel(GdkPixbuf *pixbuf, int x, int y, guchar red, guchar green, guchar blue, guchar alpha);
29
30 //Paint a background function to make a pixel buffer and an image to display as default canvas
31 static void paint_a_background (gpointer data)
32 {
33     GdkPixbuf *p;
34     p = gdk_pixbuf_new(GDK_COLORSPACE_RGB, 0, 8, X_SIZE, Y_SIZE);
35     int x,y;
36     for (x = 0; x < X_SIZE; x++)
37     {
38         for (y = 0; y < Y_SIZE; y++)
39         {
40             put_pixel(p, (int)x, (int)y, (guchar)x, (guchar)y, (guchar)x, 255);
41         }
42     }
43     gtk_image_set_from_pixbuf(GTK_IMAGE(data), GDK_PIXBUF(p));
44     g_object_unref(p);
45 }
46
47 //Function to count the particles and print the data
48 static void count (gpointer data)
49 {
50     GdkPixbuf *p;
51     p = gdk_pixbuf_new(GDK_COLORSPACE_RGB, 0, 8, X_SIZE, Y_SIZE);
52     int x, y;
53     int RP = 0;
54     int GP = 0;
55     int BP = 0;
56     int WP = 0;
57     for (x = 0; x < X_SIZE; x++)
58     {
59         for (y = 0; y < Y_SIZE; y++)
60         {
61             switch(s.lattice_configuration[x][y])

```

```

62         {
63             case 0: //Vacant: White
64                 WP++;
65                 put_pixel(p, (int)x, (int)y, (guchar)255, (guchar)255, (guchar)255, 255);
66                 break;
67             case 1: //Occupied: Black
68                 BP++;
69                 put_pixel(p, (int)x, (int)y, (guchar)0, (guchar)0, (guchar)0, 255);
70                 break;
71             case 2: //+1: Red
72                 RP++;
73                 put_pixel(p, (int)x, (int)y, (guchar)255, (guchar)0, (guchar)0, 255);
74                 break;
75             case 3: //-1: Green
76                 GP++;
77                 put_pixel(p, (int)x, (int)y, (guchar)0, (guchar)255, (guchar)0, 255);
78                 break;
79             default:
80                 put_pixel(p, (int)x, (int)y, (guchar)0, (guchar)0, (guchar)0, 255);
81                 break;
82         }
83     }
84 }
85 FILE *fp;
86 fp = fopen("Ising.txt", "a+");
87 fprintf(fp, "%u\t%f\t%.1f\t%d\t%d\t%d\t%d\t%d\t%d\t%d\n", s.generation_time, (s.occupancy/(X_SIZE*Y_SIZE)
88 ),s.T, s.J, WP, BP, RP, GP,(X_SIZE*Y_SIZE), (WP+BP+RP+GP));
89 fclose(fp);
90 if(p != NULL)
91 {
92     gchar *str = g_strdup_printf ("T_%.2f_J_%.2f_.png", s.T, s.J);
93     cairo_surface_t *surf = cairo_image_surface_create(CAIRO_FORMAT_RGB24, X_SIZE, Y_SIZE);
94     cairo_t *cr = cairo_create(surf);
95     gdk_cairo_set_source_pixbuf(cr, p, 0, 0);
96     cairo_paint(cr);
97     cairo_surface_write_to_png(surf, str);
98     g_print("Screenshot saved as T_%.2f_J_%.2f_.png\n", s.T, s.J);
99 }
100 else
101 {
102     g_print("Unable to get the screenshot.\n");
103 }
104
105 //Function to paint lattice DATA from the simulation into a pixbuffer
106 static void paint_lattice (gpointer data)
107 {
108     GdkPixbuf *p;
109     p = gdk_pixbuf_new(GDK_COLORSPACE_RGB, 0, 8, X_SIZE, Y_SIZE);
110     //Paint the lattice configuration to a pixbuffer
111     int x,y;
112     for (x = 0; x < X_SIZE; x++)
113     {
114         for (y = 0; y < Y_SIZE; y++)
115         {
116             switch(s.lattice_configuration[x][y])
117             {
118                 case 0: //Vacant: White
119                     put_pixel(p, (int)x, (int)y, (guchar)255, (guchar)255, (guchar)255, 255);
120                     break;
121                 case 1: //Occupied: Black
122                     put_pixel(p, (int)x, (int)y, (guchar)0, (guchar)0, (guchar)0, 255);
123                     break;
124                 case 2: //+1: Red
125                     put_pixel(p, (int)x, (int)y, (guchar)218, (guchar)0, (guchar)0, 255);

```

```

126         break;
127         case 3: //-1: Green
128             put_pixel(p, (int)x, (int)y, (guchar)0, (guchar)201, (guchar)29, 255);
129             break;
130         default:
131             put_pixel(p, (int)x, (int)y, (guchar)0, (guchar)0, (guchar)0, 255);
132             break;
133     }
134 }
135 }
136 gtk_image_set_from_pixbuf(GTK_IMAGE(data), GDK_PIXBUF(p));
137 g_object_unref(p);
138 }
139
140 //Function to calculate the interaction energy
141 int energy (int random_x_coor2, int random_y_coor2)
142 {
143     double j = s.J;
144     int EO, Et;
145     int R = 0;
146     int G = 0;
147     if (s.lattice_configuration[random_x_coor2][random_y_coor2] == 2){EO = 1;}
148     else if (s.lattice_configuration[random_x_coor2][random_y_coor2] == 3){EO = -1;}
149     if (s.lattice_configuration[random_x_coor2][(int)((Y_SIZE + random_y_coor2+1)%Y_SIZE)] == 2){R++;}
150     else if (s.lattice_configuration[random_x_coor2][(int)((Y_SIZE + random_y_coor2+1)%Y_SIZE)] == 3){G++;}
151     if (s.lattice_configuration[random_x_coor2][(int)((Y_SIZE + random_y_coor2-1)%Y_SIZE)] == 2){R++;}
152     else if (s.lattice_configuration[random_x_coor2][(int)((Y_SIZE + random_y_coor2-1)%Y_SIZE)] == 3){G++;}
153     if (s.lattice_configuration[(int)((X_SIZE + random_x_coor2-1)%X_SIZE)][random_y_coor2] == 2){R++;}
154     else if (s.lattice_configuration[(int)((X_SIZE + random_x_coor2-1)%X_SIZE)][random_y_coor2] == 3){G++;}
155     if (s.lattice_configuration[(int)((X_SIZE + random_x_coor2+1)%X_SIZE)][random_y_coor2] == 2){R++;}
156     else if (s.lattice_configuration[(int)((X_SIZE + random_x_coor2+1)%X_SIZE)][random_y_coor2] == 3){G++;}
157     Et = j*EO*(R-G);
158     return Et;
159 }
160
161 //Update Function which simulates the stochastic process and updates the lattice configuration
162 int update_lattice(gpointer data)
163 {
164     long random_number;
165     double random_number1, random_number2;
166     int r_n_s; //Random_neighbour_state
167     long random_neighbour;
168     int x, y, E1, E2, dE1, dE2;
169     double T = s.T;
170     double B1, B2;
171     int sites = 0;
172     int random_x_coor, random_y_coor, random_x_coor2, random_y_coor2;
173     double probability_of_state = 0.1; //Probability of adopting a state (+1 or -1)
174     double death_rate = 0.0001; //Probability of death
175     for (sites; sites < (int)(Y_SIZE*X_SIZE); sites++)
176     {
177         random_x_coor = (int) floor(genrand64_real3()*X_SIZE);
178         random_y_coor = (int) floor(genrand64_real3()*Y_SIZE);
179         switch(s.lattice_configuration[random_x_coor][random_y_coor]) //Pick a random focal site
180         {
181             case 0: //If the site is empty chose a random neighbour from the 4 possible ones
182                 random_neighbour = (long) floor(genrand64_real3()*4);
183                 switch(random_neighbour)
184                 {
185                     case 0: //south
186                         r_n_s=s.lattice_configuration[random_x_coor][(int)((Y_SIZE+random_y_coor-1)%Y_SIZE)];
187                         break;
188                     case 1: //north
189                         r_n_s=s.lattice_configuration[random_x_coor][(int)((Y_SIZE+random_y_coor+1)%Y_SIZE)];
190                         break;

```

```

191         case 2: //east
192             r_n_s=s.lattice_configuration[(int)((X_SIZE+random_x_coor-1)%X_SIZE)][random_y_coor];
193             break;
194         case 3: //west
195             r_n_s=s.lattice_configuration[(int)((X_SIZE+random_x_coor+1)%X_SIZE)][random_y_coor];
196             break;
197     }
198     //If its random neighbour is occupied: put a particle at the focal site. Note that when all 4
199     //neighbours are occupied colonization of the focal site happens with probability 1.0.
200     if (r_n_s == 1)
201     {
202         s.lattice_configuration[random_x_coor][random_y_coor]= 1;
203         s.occupancy ++;
204     }
205     else if (r_n_s == 2)
206     {
207         s.lattice_configuration[random_x_coor][random_y_coor]= 2;
208         s.occupancy ++;
209     }
210     else if (r_n_s == 3)
211     {
212         s.lattice_configuration[random_x_coor][random_y_coor]= 3;
213         s.occupancy ++;
214     }
215     break;
216 case 1: //If a black particle is present at the focal site:
217     //It can die with probability death_rate
218     if (genrand64_real2() < death_rate)
219     {
220         s.lattice_configuration[random_x_coor][random_y_coor]= 0;
221         s.occupancy --;
222     }
223     //It can adopt a state (+1 or -1) with probability probability_of_state
224     else
225     {
226         if (genrand64_real1() < probability_of_state)
227         {
228             random_number = (long) floor(genrand64_real3()*2);
229             if (random_number == 0)
230             {
231                 s.lattice_configuration[random_x_coor][random_y_coor]= 2;
232             }
233             else if (random_number == 1)
234             {
235                 s.lattice_configuration[random_x_coor][random_y_coor]= 3;
236             }
237         }
238     }
239     break;
240 }
241 int MC = 0;
242 for (MC; MC < 100; MC++)
243 {
244     random_x_coor2 = (int) floor(genrand64_real3()*X_SIZE);
245     random_y_coor2 = (int) floor(genrand64_real3()*Y_SIZE);
246     switch(s.lattice_configuration[random_x_coor2][random_y_coor2]) //Pick a second random focal site
247     {
248         case 2: //If a red particle is present at the focal site, calculate the interaction energy
249             if (genrand64_real2() < death_rate)
250             {
251                 s.lattice_configuration[random_x_coor2][random_y_coor2]= 0;
252                 s.occupancy --;
253             }
254             else
255             {

```

```

255         random_number1 = genrand64_real3();    //r must be a random number such that 0 < r < 1
256         E1 = energy (random_x_coor2, random_y_coor2);
257         dE1 = -E1-E1;
258         B1 = exp(-dE1/T);
259         if (dE1 < 0 || random_number1 < B1)
260         {
261             s.lattice_configuration[random_x_coor2][random_y_coor2] = 3;
262         }
263     }
264     break;
265     case 3: //If a green particle is present at the focal site, calculate the interaction energy
266         if (genrand64_real2() < death_rate)
267         {
268             s.lattice_configuration[random_x_coor2][random_y_coor2] = 0;
269             s.occupancy --;
270         }
271         else
272         {
273             random_number2 = genrand64_real3();    //r must be a random number such that 0 < r < 1
274             E2 = energy (random_x_coor2, random_y_coor2);
275             dE2 = -E2-E2;
276             B2 = exp(-dE2/T);
277             if (dE2 < 0 || random_number2 < B2)
278             {
279                 s.lattice_configuration[random_x_coor2][random_y_coor2] = 2;
280             }
281         }
282         break;
283     }
284 }
285 }
286 s.generation_time ++;
287 paint_lattice (data);
288 g_print ("\tGen:\t%u\n", s.generation_time);
289 if(s.generation_time == 200)    //Stop the simulation after 200 generations
290 {
291     g_source_remove(s.run);
292     s.running = FALSE;
293     g_print ("Simulation Stopped\n");
294     count (data);    //Call the function that counts the particles
295 }
296 return 0;
297 }
298
299 //TIME HANDLER to connect the update function to the Gtk loop for its computation
300 gboolean time_handler (gpointer data)
301 {
302     update_lattice(data);
303     return TRUE;
304 }
305
306 //CALL BACK to initialize the lattice button click
307 static void init_lattice(GtkWidget *widget, gpointer data)
308 {
309     int r=2;
310     //Start with an empty lattice
311     int x,y;
312     for (x = 0; x < X_SIZE; x++)
313     {
314         for (y = 0; y < Y_SIZE; y++)
315         {
316             s.lattice_configuration[x][y]=0;
317         }
318     }
319     s.occupancy = 0;

```

```

320     s.lattice_configuration[X_SIZE/2][Y_SIZE/2]=1; //Put a particle in the middle
321     s.occupancy ++;
322     s.initialized = TRUE;
323     s.generation_time = 0;
324     paint_lattice(data);
325     g_print ("Lattice initialized\n");
326 }
327
328 //CALL BACK to start the simulation button click
329 static void start_simulation (GtkWidget *widget, gpointer data)
330 {
331     if(!s.running && s.initialized)
332     {
333         s.run = g_idle_add((GSourceFunc) (GSourceFunc) time_handler, GTK_IMAGE(data));
334         s.running = TRUE;
335         g_print ("Simulation started\n");
336     }
337 }
338
339 //CALL BACK to stop simulation button click
340 static void stop_simulation (GtkWidget *widget, gpointer data)
341 {
342     if(s.running)
343     {
344         g_source_remove(s.run);
345         s.running = FALSE;
346         g_print ("Simulation Stopped\n");
347     }
348 }
349
350 //CALL BACK to respond Gtk SCALE SLIDE move event
351 static void T_scale_moved (GtkRange *range, gpointer user_data)
352 {
353     GtkWidget *label = user_data;
354     gdouble pos = gtk_range_get_value (range);
355     s.T = (float) pos;
356     gchar *str = g_strdup_printf ("T = %.2f", pos);
357     gtk_label_set_text (GTK_LABEL (label), str);
358     g_free(str);
359 }
360
361 //CALL BACK to respond Gtk SCALE SLIDE move event
362 static void J_scale_moved (GtkRange *range, gpointer user_data)
363 {
364     GtkWidget *label = user_data;
365     gdouble pos = gtk_range_get_value (range);
366     s.J = (float) pos;
367     gchar *str = g_strdup_printf ("J = %.2f", pos);
368     gtk_label_set_text (GTK_LABEL (label), str);
369     g_free(str);
370 }
371
372 //ACTIVATE function with all Widget Initialization and creation
373 static void activate (GtkApplication *app, gpointer user_data)
374 {
375     //Declare a bunch of Gtk WIDGETS for the GUI
376     GtkWidget *window, *grid, *button, *image_lattice;
377     //To draw into the window images
378     GdkPixbuf *pixbuf;
379     //To control the parameter of the process
380     GtkWidget *T_scale, *T_label, *J_scale, *J_label;
381
382     //Initialize the mt algorithm for random number generation
383     unsigned long long seed = (unsigned int)time(NULL);
384     init_genrand64(seed);

```

```

385
386 //Define default parameters of the simulation
387 s.T = 0.10;
388 s.J = -1.00;
389 s.running = FALSE;
390 s.initialized = FALSE;
391
392 //Create a new WINDOW, and set its title
393 window = gtk_application_window_new (app);
394 gtk_window_set_title (GTK_WINDOW (window), "Ising Model");
395 gtk_window_set_resizable (GTK_WINDOW(window), FALSE);
396
397 //Make a GRID that is going to pack the Widgets
398 grid = gtk_grid_new ();
399 //Pack the GRID in the window
400 gtk_container_add (GTK_CONTAINER (window), grid);
401
402 //SCALE SLIDE BAR to set and LABEL display T
403 T_scale = gtk_scale_new_with_range(GTK_ORIENTATION_HORIZONTAL,0.01,10,0.01);
404 T_label = gtk_label_new ("T");
405 g_signal_connect (T_scale,"value-changed", G_CALLBACK (T_scale_moved), T_label);
406 gtk_grid_attach (GTK_GRID (grid), T_scale, 0, 0, 1, 1);
407 gtk_grid_attach (GTK_GRID (grid), T_label, 1, 0, 2, 1);
408
409 //SCALE SLIDE BAR to set and LABEL display J
410 J_scale = gtk_scale_new_with_range(GTK_ORIENTATION_HORIZONTAL,-1,1,1);
411 J_label = gtk_label_new ("J");
412 g_signal_connect (J_scale,"value-changed", G_CALLBACK (J_scale_moved), J_label);
413 gtk_grid_attach (GTK_GRID (grid), J_scale, 3, 0, 1, 1);
414 gtk_grid_attach (GTK_GRID (grid), J_label, 4, 0, 3, 1);
415
416 //PIXEL BUFFER @ START UP and LATTICE CONFIGURATION DISPLAY IMAGE
417 pixbuf = gdk_pixbuf_new(GDK_COLORSPACE_RGB, 0, 8, X_SIZE, Y_SIZE);
418 image_lattice = gtk_image_new_from_pixbuf(pixbuf);
419 paint_a_background(image_lattice);
420 gtk_grid_attach (GTK_GRID (grid), image_lattice, 0, 1, 5, 1);
421
422 // ----- INIT BUTTON -----
423 button = gtk_button_new_with_label ("Initialize");
424 g_signal_connect (button, "clicked", G_CALLBACK (init_lattice),
425 GTK_IMAGE(image_lattice));
426 gtk_grid_attach (GTK_GRID (grid), button, 0, 3, 1, 1);
427
428 // ----- START BUTTON -----
429 button = gtk_button_new_with_label ("Start");
430 g_signal_connect (button, "clicked", G_CALLBACK (start_simulation),
431 GTK_IMAGE(image_lattice));
432 gtk_grid_attach (GTK_GRID (grid), button, 1, 3, 1, 1);
433
434 // ----- STOP BUTTON -----
435 button = gtk_button_new_with_label ("Stop");
436 g_signal_connect (button, "clicked", G_CALLBACK(stop_simulation), NULL);
437 g_signal_connect (button, "clicked", G_CALLBACK(count), NULL);
438 gtk_grid_attach (GTK_GRID (grid), button, 2, 3, 1, 1);
439
440 //----- QUIT BUTTON -----
441 button = gtk_button_new_with_label ("Quit");
442 g_signal_connect_swapped (button, "clicked", G_CALLBACK (gtk_widget_destroy), window);
443 gtk_grid_attach (GTK_GRID (grid), button, 4, 3, 1, 1);
444
445 //Show the window and all widgets
446 gtk_widget_show_all (window);
447 }
448
449 //Main

```



---

```

450 int main (int argc, char **argv)
451 {
452     GtkApplication *app;
453     int status;
454     app = gtk_application_new ("keymer.lab.contact_process", G_APPLICATION_FLAGS_NONE);
455     g_signal_connect (app, "activate", G_CALLBACK (activate), NULL);
456     status = g_application_run (G_APPLICATION (app), argc, argv);
457     g_object_unref (app);
458     return status;
459 }
460
461 //Implementation of putpixel. https://developer.gnome.org/gdk-pixbuf/stable/gdk-pixbuf-The-GdkPixbuf-Structure.html
462 void put_pixel(GdkPixbuf *pixbuf, int x, int y, guchar red, guchar green, guchar blue, guchar alpha)
463 {
464     guchar *pixels, *p;
465     int rowstride, numchannels;
466     numchannels = gdk_pixbuf_get_n_channels(pixbuf);
467     rowstride = gdk_pixbuf_get_rowstride(pixbuf);
468     pixels = gdk_pixbuf_get_pixels(pixbuf);
469     p = pixels + y * rowstride + x * numchannels;
470     p[0] = red; p[1] = green; p[2] = blue; p[3] = alpha;
471 }

```

---

### 3.2.1 Simulation of the two-dimensional Ising model in growing cell populations

To study how positive and negative gene correlations arise from short-range coupling between gene networks (Fig. 1.1), we employed the CP-IM simulations (Section 3.1.1) since this explicitly captures the essence of how long-range patterns of spatial correlations emerge from the dynamics of two-state interacting entities. As mentioned in Chapter 1 (Section 1.3), in the Ising model without the influence of an external magnetic field, two competing effects determine the orientation of the spins on the lattice: *i*) the tendency of spins to align (or anti-align) their orientations to minimize the energy of the system (Eq. 1.1), and *ii*) the thermal fluctuations, which increase with the temperature  $T$  of the system, that tend to randomize the orientation of spins (Eq. 1.3) (Fig. 1.2B). Thus, the parameter that determines the degree of alignment of spins (and the transition between order and disorder) is  $T$  in the classical Ising model; hence, a small value of  $T$  represents a strong coupling between cells, while a large value represents a weak coupling.

The magnetization per site ( $M$ ) calculated for ferromagnetic populations obtained from CP-IM simulations (Fig. 3.1B left) showed a good agreement with

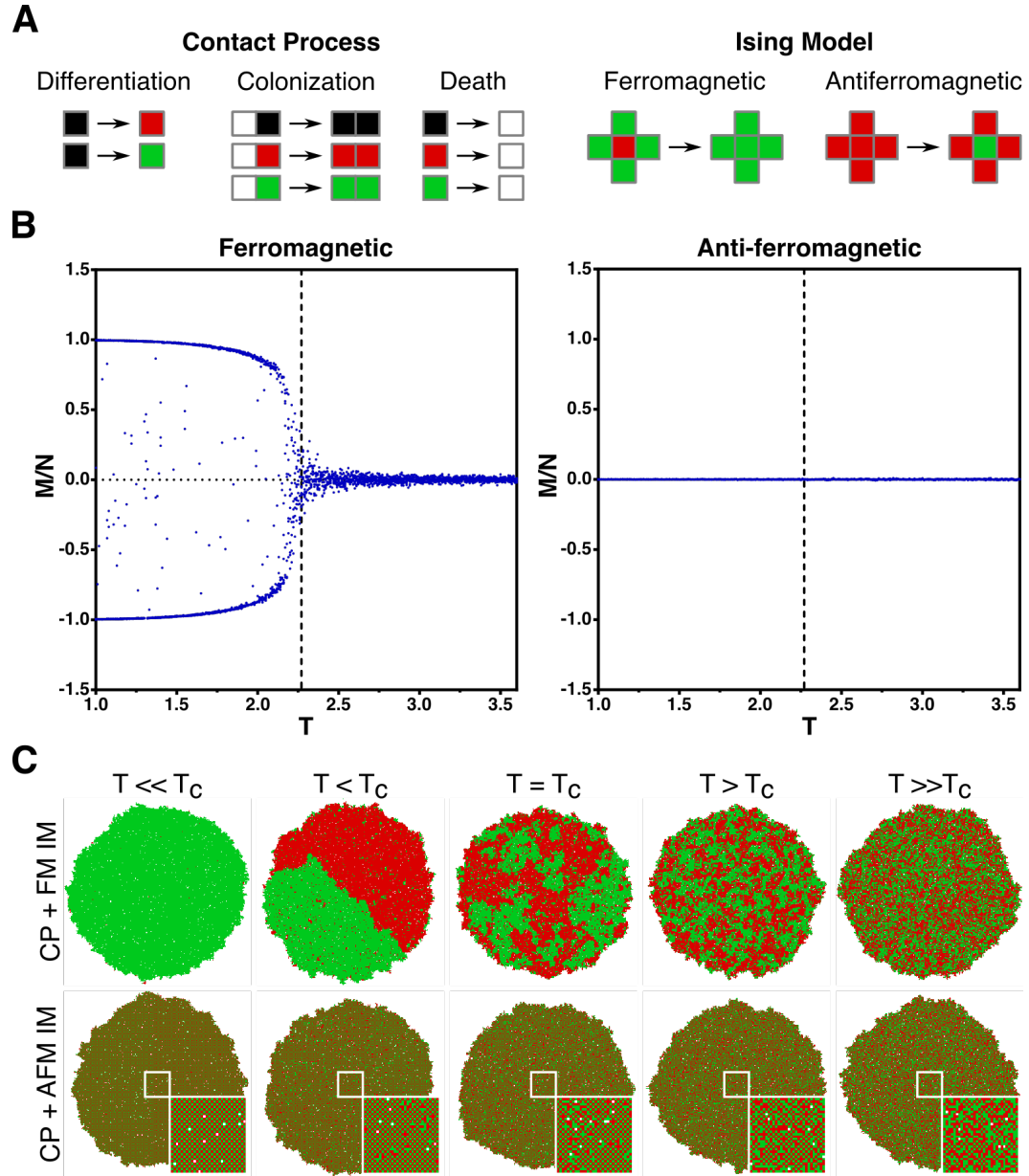


**Figure 3.1: Ising-like interactions in a growing population obtained from the CP-IM simulations.** (A) Lattice reactions of colonization, differentiation and death processes (left) and Ising-like cellular state change mechanisms (right) that define the model that combines the Contact Process lattice model and the two-dimensional Ising model (CP-IM simulations). Squares represents a vacant space (white), an undifferentiated cell (black), or a differentiated cell in red (red) or green (green) state. (B) Magnetization per site  $M/N$  as a function of  $T$  for ferromagnetic and anti-ferromagnetic populations obtained from CP-IM simulations. Dotted vertical lines mark the critical value of  $T$  ( $T_c$ ). 10 simulations per each value of  $T$  (C) Numerical simulations of the two-dimensional Ising model during the growth of ferromagnetic (CP + FM IM) and anti-ferromagnetic (CP + AFM IM) cell populations at different values of the control parameter  $T$  relative to the critical value  $T_c$ . In this model,  $T$  represents a parameter that determines the strength of the coupling between cells. Insets correspond to a magnification of the square in the center of the anti-ferromagnetic colonies showing a detail of the checkerboard-like pattern.

the behaviour observed in the classical 2D Ising model [95]. Before  $T_c$ , most cells have the same cellular state due to the strong coupling between cells, and the value of  $|M|$  is close to 1, defining the ordered state of the system. Above  $T_c$ , the coupling between cells is not strong enough and cells can randomly adopt a cellular state, independent of the state of their neighbours. At this point, the value of  $|M|$  is close to 0 and the system is in the disordered state. On the other hand, the value of the magnetization for a population with anti-ferromagnetic interactions showed to be always close to zero, independent of the value of  $T$  (Fig. 3.1B right).

The results of the magnetization per site can be graphically observed in Figure 3.1C, which shows the different cellular state configurations that emerge during the growth of a cellular population depending on the strength of the coupling between cells (the value of  $T$ ) and the type of interaction (ferromagnetic or anti-ferromagnetic). In a ferromagnetic colony (Fig. 3.1C top), a strong interaction ( $T < T_c$ ) favours the alignment of states between neighbouring cells, leading to the emergence of large homogeneous patches of cells in the same state. A further increase in the coupling strength ( $T \ll T_c$ ) leads the system to be completely dominated by the internal energy of cell coupling, making ordered configurations more favourable, i.e. the generation of populations with cells in only one state. On the other hand, if the coupling between cells is weak ( $T > T_c$ ), the contribution of the interaction energy  $\mathcal{H}$  (Eq. 1.1) becomes less relevant in the formation of spatial structures. Here, high energy configurations are equally probable as low energy configurations (Eq. 1.3), and cells can freely change their states regardless the state of their neighbours, leading to a colony with a noise-like appearance. Near a critical value of  $T$  ( $T = T_c$ ), cellular states are neither aligned nor random. Colonies spontaneously self-organize into patterns that resemble the long-range correlations and power-law decaying fractal objects described by universality class exponents of the Ising model at phase transition. At the critical point of the Ising model, the correlation function, which is a measure of the order in a system, falls as a power law given by

$$C(r) \sim \frac{1}{r^{d-2+\eta}} \quad (3.1)$$

where  $d$  is the dimension of the space ( $d = 2$  in a two-dimensional space), and  $\eta$  is the critical exponent of the correlation function [95, 96]. At the critical point, the spatial autocorrelation function (sACF) of ferromagnetic populations from the CP-IM simulations showed to follow a power-law decay of the form  $C(r) \sim r^{-\eta}$  (Fig. 3.2), with  $\eta = 0.2518$ . This critical exponent showed to be consistent with the reported value for the Ising model at the critical temperature  $\eta = 0.250$  [95] (the spatial autocorrelation function will be discussed in more detail in Section 4.2.3). This behavior close to the critical transition is particularly relevant since it links the short-range coupling between cellular states with the generation of macroscopic long-range correlations (Fig. 1.1).

A similar behavior can be observed in anti-ferromagnetic colonies: an ordered configuration of cellular states emerges in colonies with strong coupling between cells (small values of  $T$ ), and a disordered configuration in colonies with weak interactions (large values of  $T$ ) (Fig. 3.1C bottom). However, since in anti-ferromagnetic colonies the interaction energy is minimized when cells have the opposite state of their neighbours, in the ordered configuration the opposite cellular states between neighbouring cells are favoured. This results in the emergence of a checkerboard-like pattern of cellular states, i.e. a cell in the red state surrounded by four cells in the green state and vice versa. Near the critical value, colonies are composed of patches of checkerboard-like patterns separated by disordered regions.

Taken together, the CP-IM simulations suggested that Ising-like interactions during the growth of a cell population allow the generation of different self-organized patterns of gene correlations. These results lead us to suggest that implementing these rules in synthetic genetic network (SGNs), i.e. two states coupled through short-ranged interactions, should be enough to generate cellular state patterns of either positive or negative gene spatial correlations similar to those observed in the simulations of the Ising model in a bacterial population.

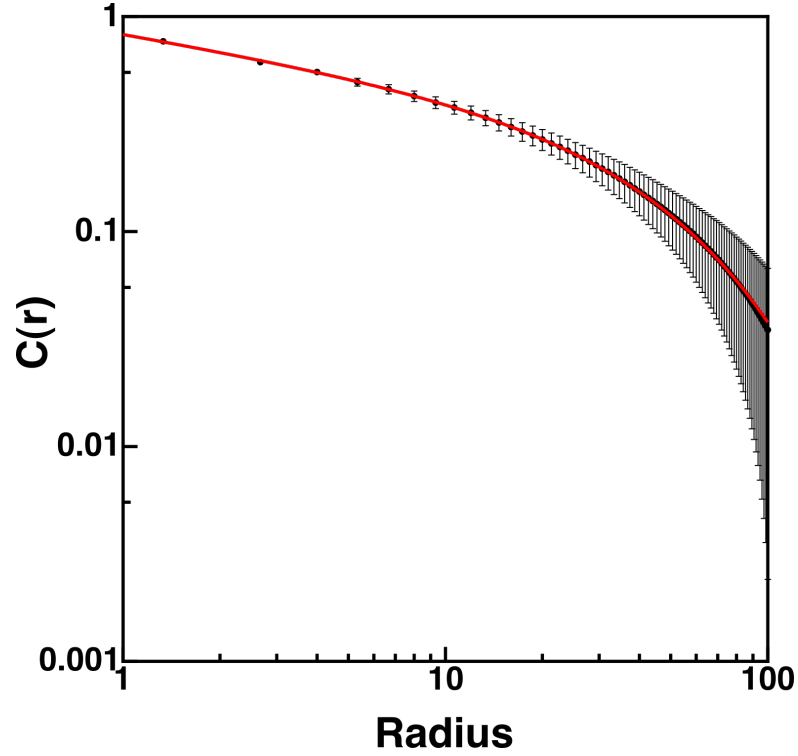


**Figure 3.2: Power-law decay of the spatial autocorrelation function in simulated ferromagnetic populations.** sACF of simulated populations with ferromagnetic interactions at the critical value of  $T$  ( $T = T_c$ ). The sACF showed to follow a power-law decay with a critical exponent  $\eta = 0.2518$ . Black dots and error bars correspond to the mean  $\pm$  the standard deviation of the sACF of 50 simulations at  $T = T_c$ , and the red line correspond to the best fit of the data to the curve  $C(r) = A \frac{\exp(-r/B)}{r^C}$ , where  $C$  correspond to the critical exponent of the autocorrelation function  $\eta$ . The radius is in pixels

# Chapter 4

## Two-state and coupled bacterial systems

### 4.1 Design and construct synthetic bacterial systems that exhibit two states and coupling between them

#### 4.1.1 Generation of coupled two-state gene networks in bacteria

To test the predictions of CP-IM simulations (Section 3.2.1), we constructed in *E. coli* two synthetic genetic circuits that exhibit two states and chemical coupling between their states (Fig. 4.1). As in the Ising model, we name these systems ferromagnetic if cells can induce the same state in neighbouring cells, or anti-ferromagnetic if cells induce the opposite state (Fig. 4.1A). Each system is composed of three main functions (Fig. 4.1A top left): *i*) a cellular state reporter function, responsible for the synthesis of red (mCherry2) or green (sfGFP) fluorescent proteins to report the state of cells, *ii*) a switch function, composed of two repressors (LacI and TetR) that mutually repress each other expression (as in

a genetic toggle switch [45]) allowing cells to adopt only one of the two possible cellular states at a time, and *iii*) a coupling function, which, depending on the state of the cell, allows the production of one of the two coupling molecules for each state (3-oxo-C6-homoserine lactone (C6HSL), synthesised by LuxI from *V. fischeri*, or 3-oxo-C12-homoserine lactone (C12HSL), synthesised by LasI from *P. aeruginosa*).

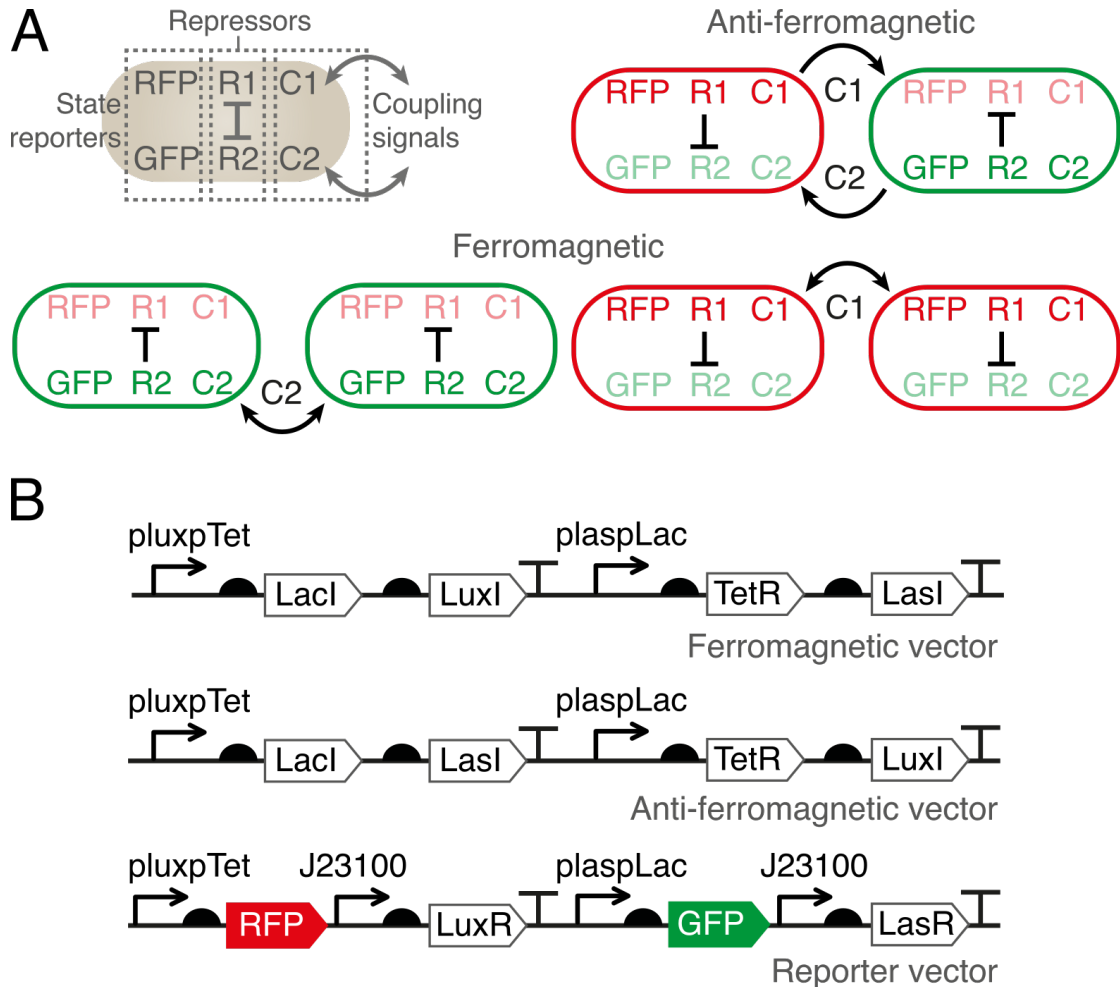


**Figure 4.1: Two-state and coupled SGNs.** (A) Schematic illustration of ferromagnetic and anti-ferromagnetic systems on two neighbouring cells, highlighting the capability of each cell to acquire any of the two states, red or green, defined by the synthesis of a red (RFP) or green (GFP) fluorescent protein. These states are determined by mutually inhibiting repressors R1 and R2, and connected by coupling signals C1 and C2. (B) Genetic network arrangement of the reporter vector and the Ising ferromagnetic and anti-ferromagnetic vectors. Ferromagnetic and anti-ferromagnetic systems are composed of the ferromagnetic or the anti-ferromagnetic vector along with the reporter vector.

In both systems, these functions are contained in two vectors: the reporter vector, which contains the cellular state reporter function, and the Ising ferromagnetic or anti-ferromagnetic vectors, which contain the switch and coupling functions (Fig. 4.1B). The reporter vector also allows the constitutive expression of genes encoding the transcriptional activators LuxR and LasR, which bind C6HSL and C12HSL as ligands, respectively, to activate the expression of genes through the binding to their respective promoters. To construct these vectors, we used a combination of the Golden Gate [84] and Gibson Assembly [85] molecular cloning methods (see Chapter 2, subsection 2.3.5), which allowed us to construct different vectors with different combinations of Transcriptional Units (TUs). In these vectors, the expression of genes encoding the repressors, red/green fluorescent protein, and C6HSL and C12HSL biosynthetic enzymes are under a pair of inducible/repressible promoters: the pLux76pTet promoter, which is induced by C6HSL and repressed by TetR, and the pLas81pLac promoter, which is induced by C12HSL and repressed by LacI. Thus, the state of each cell that carries these systems is determined by the concentration of the coupling molecule they can sense, and the coupling molecule with which they respond depends on the Ising vector they carry. In the ferromagnetic vector, *LuxI* and *LasI* are under the control of the pLux76pTet and pLas81pLac promoters, respectively, allowing cells to synthesize the same coupling molecule they sense and induce the same state in neighbouring cells. In the anti-ferromagnetic vector, on the other hand, *LasI* and *LuxI* are under the control of the pLux76pTet and pLas81pLac promoters, respectively, allowing cells to synthesize the opposite coupling signal they sense and therefore induce the opposite state in neighbouring cells. In both systems, repressors *LacI* and *TetR* are under the control of the pLux76pTet and pLas81pLac promoters, respectively, ensuring that the production of one coupling signal is accompanied by the inhibition of the production of the other.



### 4.1.2 Behaviour of ferromagnetic and anti-ferromagnetic populations in a well-mixed environment

To test the two-state condition and coupling properties of ferromagnetic and anti-ferromagnetic systems, we measured the fluorescence of mCherry2 and sfGFP during the growth of liquid cultures of *E. coli* cells carrying these systems under different concentrations of the coupling signals C6HSL and C12HSL. Using this data, we calculated the red and green fluorescent protein synthesis rate for each concentration of the coupling signal as previously reported [97] (Fig. 4.2). To model the behaviour of the systems in liquid culture, we considered a simplified model in which each dual promoter (pLux76pTet and pLas81pLac) has two activity states: an active state that allows the expression of the genes coding the fluorescent proteins (ON state), and an inactive state in which there is no expression of these genes (OFF state). This consideration implies a total of four free-energy states for each promoter based on the combination of active and inactive states with or without a ligand bound [98]: ON without ligand bound, ON with ligand bound, OFF without ligand bound, and OFF with ligand bound. In our systems, the ligand represents the concentrations of the coupling signals C6HSL and C12HSL, which are assumed to be present at local concentration  $L$  in the medium, and bind to its promoter through the transcriptional activators LuxR and LasR. At equilibrium, the probability  $P$  of finding a promoter in the active state is:

$$P_{on} = \left( 1 + \left[ \frac{1 + [L] / K_d^{off}}{1 + [L] / K_d^{on}} \right]^n \cdot e^{-n\beta\Delta E} \right)^{-1} \quad (4.1)$$

where  $\Delta E = E_{off} - E_{on}$  represents the energy difference between inactive and active promoter without ligand bound,  $K_d^{on}$  and  $K_d^{off}$  are the dissociation constants that characterize the binding of ligands to active and inactive promoters, respectively, and  $n$  is a Hill exponent to represents cooperative binding. All energies are in thermal energy units  $k_B T$ . Equation 4.1 shows that the probability of finding a promoter in the active state depends on a few biological variables: the energy difference between the OFF and ON states of the promoter in absence of

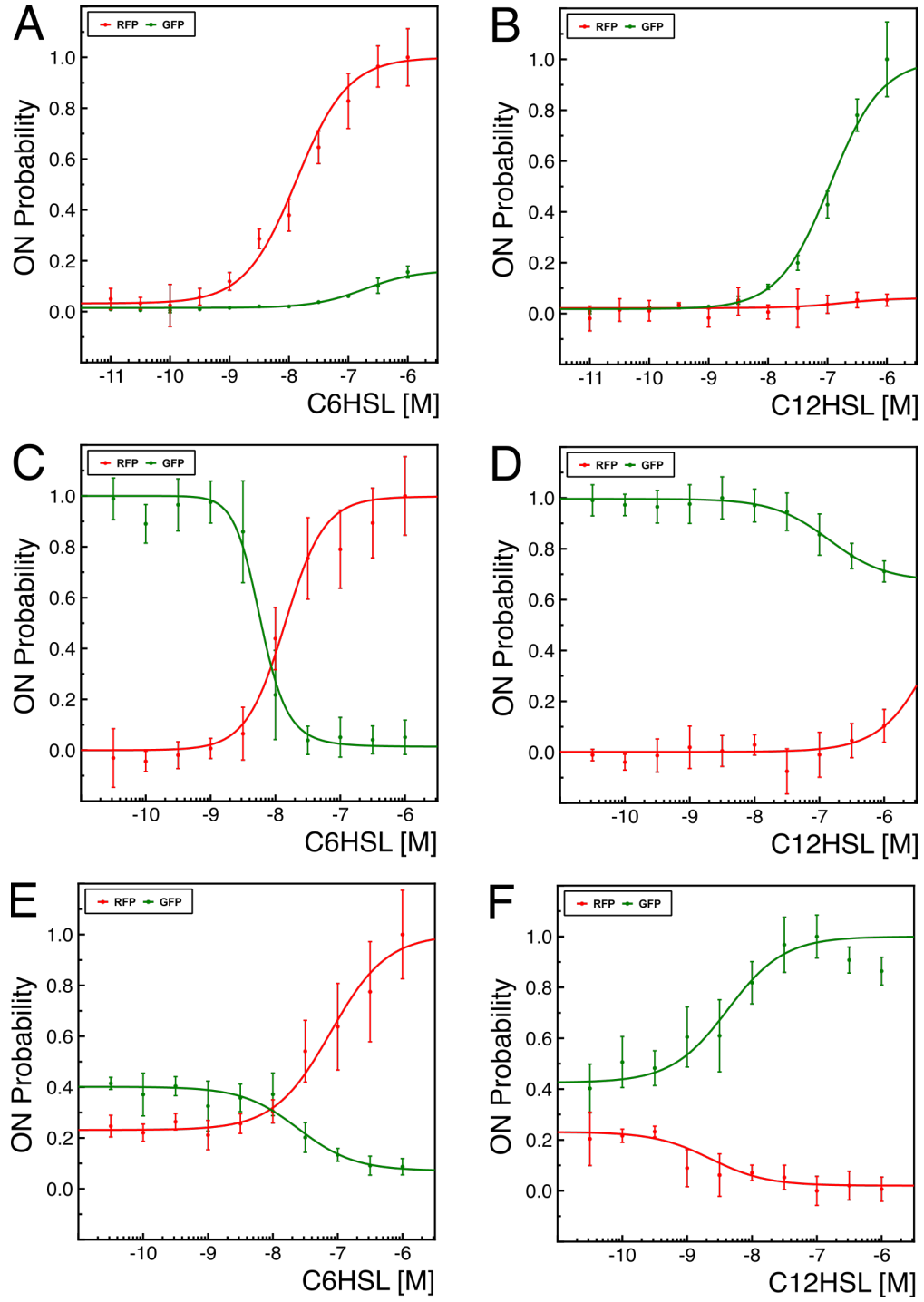


**Figure 4.2: Behaviour of the two-state and coupled SGNs in a well-mixed population.** Red and green fluorescent protein synthesis rate of *E. coli* cells carrying the reporter vector (A, B), ferromagnetic (C, D) and anti-ferromagnetic (E, F) systems grown in liquid M9-glucose medium supplemented with different concentrations of the coupling signals C6HSL (left) and C12HSL (right). Points and error bars correspond to the mean of the fluorescent protein synthesis rates normalized by its maximum value reached in each system  $\pm$  the standard deviation of 4 biological replica, while solid lines correspond to the best fit of the data to Equation 4.1. Values on x-axis are the  $\log_{10}$  of the C6HSL and C12HSL concentrations.

coupling signal, the affinity of the coupling signal for the ON and OFF states of the promoter, and the concentration of the coupling signal  $L$ . In the ferromagnetic and anti-ferromagnetic systems, the binding of a ligand to its promoter favors its activation, while in turn it also favors the inactivation of the other promoter through the synthesis of its repressor (Fig. 4.1B). This means that the binding of a ligand to its promoter favors the ON state of that promoter ( $K_d^{on} \ll K_d^{off}$ ), and, indirectly, the same ligand favors the OFF state of the other promoter ( $K_d^{on} \gg K_d^{off}$ ). Equation 4.1 also predicts that the probability of finding the promoters in the ON or OFF state in absence of coupling signals depends on the value of  $\Delta E$ : if  $\Delta E < 0$  ( $E_{off} < E_{on}$ ), the OFF state is favored, while if  $\Delta E > 0$  ( $E_{off} > E_{on}$ ), the ON state is favored. Thus, the values of  $\Delta E$ ,  $K_d^{on}$  and  $K_d^{off}$  characterize the binding of the inducers C6HSL and C12HSL to the promoters that control the expression of the red and green fluorescent proteins in each system.

To obtain the values of  $\Delta E$ ,  $K_d^{on}$ ,  $K_d^{off}$ , and  $n$ , we fitted to Equation 4.1 the data of the red and green fluorescent protein synthesis rate of liquid cultures of *E. coli* cells carrying these systems under different concentrations of the inducers (Fig. 4.2). The values of these parameters for each system are shown in Tables 4.1, 4.2, and 4.3.

As expected, in a population of cells carrying only the reporter vector (along with an empty Ising vector), there are almost no synthesis of red and green fluorescent proteins at very low concentrations (and in absence) of the inducers (Fig. 4.2A and B). Increasing the concentration of C6HSL in the medium induces an increase in the synthesis rate of mCherry2 (Fig. 4.2A), while an increase in C12HSL induces an increase in the synthesis rate of sfGFP (Fig. 4.2B). This means that the probability of finding the promoters that control the expression of *mCherry2* (*mCherry2* promoter) and *sfGFP* (*sfGFP* promoter) active in absence of their inducers C6HSL and C12HSL is close to zero, and this probability increases as the concentration of its inducer increases. The behavior of a population of cells carrying only the reporter vector is reflected in the values of the parameters that characterize the binding of C6HSL and C12HSL (Table 4.1): *i*) the negative value of  $\Delta E$  indicates that the energy of the inactive promoter is smaller than the

	C6HSL		C12HSL	
	<i>mCherry2</i> P	<i>sfGFP</i> P	<i>mCherry2</i> P	<i>sfGFP</i> P
n	1.00	1.00	1.00	1.00
E [k <sub>B</sub> T]	-3.40	-4.20	-3.80	-4.00
Kdoff [M]	1.60E-05	2.20E-07	1.80E-07	1.00E-04
Kdon [M]	4.30E-10	1.70E-08	6.20E-08	2.00E-09

**Table 4.1: Reporter vector.** Biological parameters that characterize the binding of C6HSL and C12HSL to the *mCherry2* and *sfGFP* promoters in cells carrying the reporter vector.

	C6HSL		C12HSL	
	<i>mCherry2</i> P	<i>sfGFP</i> P	<i>mCherry2</i> P	<i>sfGFP</i> P
n	1.45	2.50	1.00	1.00
E [k <sub>B</sub> T]	-6.60	6.20	-6.60	5.60
Kdoff [M]	1.00E-06	1.00E-11	4.50E-04	1.60E-09
Kdon [M]	1.90E-11	2.70E-08	1.20E-08	2.10E-07

**Table 4.2: Ferromagnetic system.** Biological parameters that characterize the binding of C6HSL and C12HSL to the *mCherry2* and *sfGFP* promoters in cells carrying the ferromagnetic system.

	C6HSL		C12HSL	
	<i>mCherry2</i> P	<i>sfGFP</i> P	<i>mCherry2</i> P	<i>sfGFP</i> P
n	1.00	1.00	1.00	1.00
E [k <sub>B</sub> T]	-1.20	-0.40	-1.20	-0.30
Kdoff [M]	9.00E-04	1.60E-08	1.80E-09	1.00E-05
Kdon [M]	1.80E-08	1.40E-07	2.60E-08	1.80E-09

**Table 4.3: Anti-ferromagnetic system.** Biological parameters that characterize the binding of C6HSL and C12HSL to the *mCherry2* and *sfGFP* promoters in cells carrying the anti-ferromagnetic system.

energy of the active promoter (without ligand bound) ( $E_{off} < E_{on}$ ), and thus the OFF state is favored in absence of inducer, and *ii*) the dissociation constant that characterize the binding of the inducer to its active promoter is much smaller than the dissociation constant of the inactive promoter ( $K_d^{on} \ll K_d^{off}$ ), which means that the binding of the inducer to its promoter induces the ON state (Eq. 4.1).

Figure 4.2C and D show that a population of cells carrying the ferromagnetic system is in the green state at very low concentrations (or in absence) of the inducers, indicating that under this condition ferromagnetic cells only synthesize *sfGFP*. This means that the probability of finding the *sfGFP* promoter active is 1, while the probability of finding the *mCherry2* promoter active is 0, which is

reflected in the positive value of  $\Delta E$  for the *sfGFP* promoter and the negative value for the *mCherry2* promoter (Table 4.2). This result suggest that the system is biased towards the production of C12HSL, the inducer of the *sfGFP* promoter. Accordingly, the pLas promoter, which directs the expression of *LasI* in this system, has shown to have a higher basal expression than the pLux promoter [74, 99], which directs the expression *LuxI* (Fig. 4.1B). This higher basal expression drives cells to produce basal amounts of C12HSL, which accumulates in the medium and induces the same state in other cells, resulting in a population of cells in the same (green) state. The C12HSL bias also explains why the external addition of C12HSL did not induce major changes in the synthesis rates of fluorescent proteins (Fig. 4.2D). Around  $10^{-8}$  M of C6HSL (the inducer of the *mCherry2* promoter) there is a drastic decrease in the probability of finding the *sfGFP* promoter active, accompanied by an increase in the probability of finding the *mCherry2* promoter active (Fig. 4.2C). This behaviour is reflected in the values of the dissociation constants that characterize the binding of this inducer to its promoter: C6HSL favors the ON state of the *mCherry2* promoter ( $K_d^{on} \ll K_d^{off}$ ), which leads to an increase the red fluorescence, while at the same time it favors the OFF state of the *sfGFP* promoter ( $K_d^{on} \gg K_d^{off}$ ), leading to a decrease in the green fluorescence (Table 4.2). A further increase in the concentration of C6HSL produces a population of cells found only in the red state. This means that, depending on the concentration of C6HSL in the medium, a population of cells carrying the ferromagnetic system can be in one of 3 states: all cells in the green state (low C6HSL), all cells in the red state (high C6HSL), or a mix of red and green cells (around  $10^{-8}$  M of C6HSL). Microscope analysis of cells in the mixed state revealed that there is no “yellow” cells (data not shown), indicating that individual cells can only be in one state at a time: red or green. These results suggest that a population of ferromagnetic cells can change between red and green states, and that this change depends on the concentration of C6HSL in the medium.

On the other hand, in a population of cells carrying the anti-ferromagnetic system, the probability of finding the *sfGFP* and *mCherry2* promoters active is different from zero at very low concentrations of inducers (Fig. 4.2E, F). This

behaviour is reflected in the values of  $\Delta E$  for both promoters, which are closer to zero compared to the values of the ferromagnetic system (Table 4.3). Thus, in this condition, a population of anti-ferromagnetic cells is in a mixed state, with red and green cells. In this system, *LuxI* is under the control of the pLas promoter, allowing cells to produce a basal amount of C6HSL. Contrary to ferromagnetic system, C6HSL induces the opposite state in other cells, allowing them to produce C12HSL and leading to a balance in the production of both coupling signals. As reflected in the values of  $K_d^{on}$  and  $K_d^{off}$  (Table 4.3), increasing the concentration of C6HSL in the medium induces an increase in the probability of finding the *mCherry2* promoter active and a decrease in the probability of finding the *sfGFP* promoter active (Fig. 4.2E). Increasing the concentration of C12HSL (the inducer of the *sfGFP* promoter) produces the opposite effect, i.e. an increase in the probability of finding the *sfGFP* promoter active and a decrease in the probability of finding the *mCherry2* promoter active (Fig. 4.2F). These results show that a population of anti-ferromagnetic cells can change from an initially mixed state to a population in a red or green state depending on the concentration of the coupling signals in the medium.

Taken together, these results suggest that both ferromagnetic and anti-ferromagnetic systems exhibit two states and that there is a coupling between them in well-mixed populations. These properties are necessary to test the existence of long-range spatial correlations like the ones observed in the simulations (Fig. 3.1).

## 4.2 Study of spatial patterns generated by the two-state coupled systems in bacterial colonies

### 4.2.1 Ising-like patterns emerge in bacterial colonies of ferromagnetic and anti-ferromagnetic rod-shaped cells

To test whether the SGNs were able to achieve Ising-like patterns of gene spatial correlation such as those observed in the CP-IM simulations, we studied the fluorescent patterns that emerge in colonies of ferromagnetic and anti-ferromagnetic *E. coli* cells growing on solid medium. In order to discard any bias related to the properties of the reporters, we constructed a second version of the reporter vector, in which the promoters that direct the expression of the red and green fluorescent proteins were swapped (Fig. 4.3). Figure 4.3 show images of the fluorescence of colonies generated from cells carrying the different variants of the reporter vectors (along with the same backbone of the ferromagnetic and anti-ferromagnetic vector without insert) grown on solid M9-glucose medium supplemented with different concentrations of C6HSL. As expected, an increase in the concentration of C6HSL in the medium only produces an increase in the red fluorescence in colonies of cells carrying the reporter vector 1 (Fig. 4.3A), while an increase in concentration of the same inducer only increases the green fluorescence in colonies of cells carrying the reporter vector 2 (Fig. 4.3B).

To counteract the higher basal expression of the promoter induced by C12HSL (pLas promoter) and make red and green states equally likely, ferromagnetic and anti-ferromagnetic cells were grown on solid medium supplemented with different concentrations of C6HSL. As observed in liquid cultures, ferromagnetic colonies were found to be only in one state in absence (or at very low concentrations) of C6HSL: green for the reporter vector 1 and red for the reporter vector 2 (Fig. 4.4A, 0 M C6HSL). This is explained by the fact that cells produce basal amounts of C12HSL, which accumulates in the medium and induces the same state in other cells, generating colonies in only one state. A high concentration of

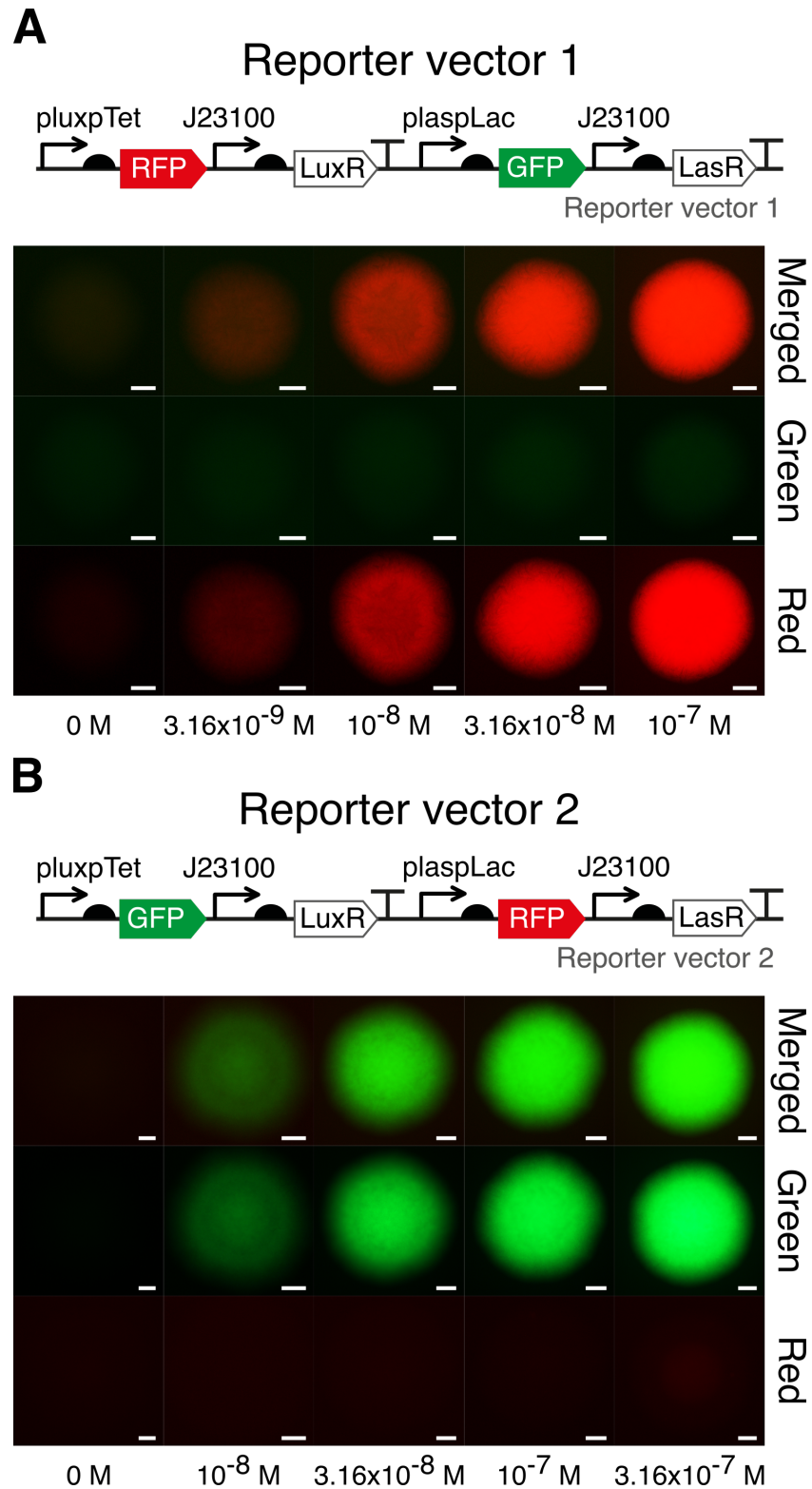


**Figure 4.3: Induction of red and green fluorescence by C6HSL in colonies of rod-shaped cells carrying different versions of the reporter vector.** Red and green fluorescence of colonies of cells carrying the reporter vector 1 (A) and reporter vector 2 (B) grown on solid M9-glucose medium supplemented with different concentrations of C6HSL. Genetic network arrangement of reporter vector 1 and 2 is included for comparison. Images were taken 14 hours after inoculation. Scale bars 100  $\mu$ m.



C6HSL ( $10^{-7}$  M) also produces colonies in only one state, but opposite to the state of colonies grown at low concentrations of this inducer (red for the reporter vector 1 and green for the reporter vector 2). At this point, global exogenous concentration of C6HSL appears to dominate the system over the endogenous, short-range coupling effects between networks. However, growing ferromagnetic cells on solid medium supplemented with  $10^{-8}$  M of C6HSL leads to the emergence of spatial patterns of red and green cellular state domains in the colonies, in accordance with the state transition found in liquid cultures (Fig. 4.2C). This result suggest that a concentration around  $10^{-8}$  M of C6HSL is able to balance the basal production of C12HSL in solid medium. The behaviour observed in colonies of ferromagnetic cells showed to be independent of the reporter vector used, since the same type of patterns emerge in colonies of cells carrying the ferromagnetic vector along with the reporter vector 1 or 2 at each concentration of C6HSL tested (4.4A).

Colonies of anti-ferromagnetic cells, on the other hand, showed a spatial pattern with red and green domains of cells in absence (and at very low concentrations) of C6HSL (Fig. 4.4B), in accordance with the mixed state observed in liquid cultures (Fig. 4.2E, F). Under this condition, the center of the colonies is dominated by cells in green (reporter vector 1) or red (reporter vector 2) state, while the periphery is mainly composed of cells in the opposite state, generating a zone with a mix of red and green cellular state domains in between. As in ferromagnetic colonies, the cellular state patterns that emerge in anti-ferromagnetic colonies in absence of external inducers can be attributed to the higher basal expression of one of the promoters, which is only counteracted in the zone dominated by an equal mix of red and green cellular domains. At this region, the concentration of C6HSL accumulated in the medium during the growth of the colony reaches a critical concentration that allows cells to change states regardless the basal expression of the promoter (see Chapter 6 for a more detailed discussion). At  $10^{-8}$  M of C6HSL (a concentration that counteracts the bias introduced by the basal expression of promoter induced by C12HSL), red and green cellular state domains emerged across the whole colony. Compared to those emerging in ferromagnetic colonies at the same C6HSL concentration, the red and green domains generated in

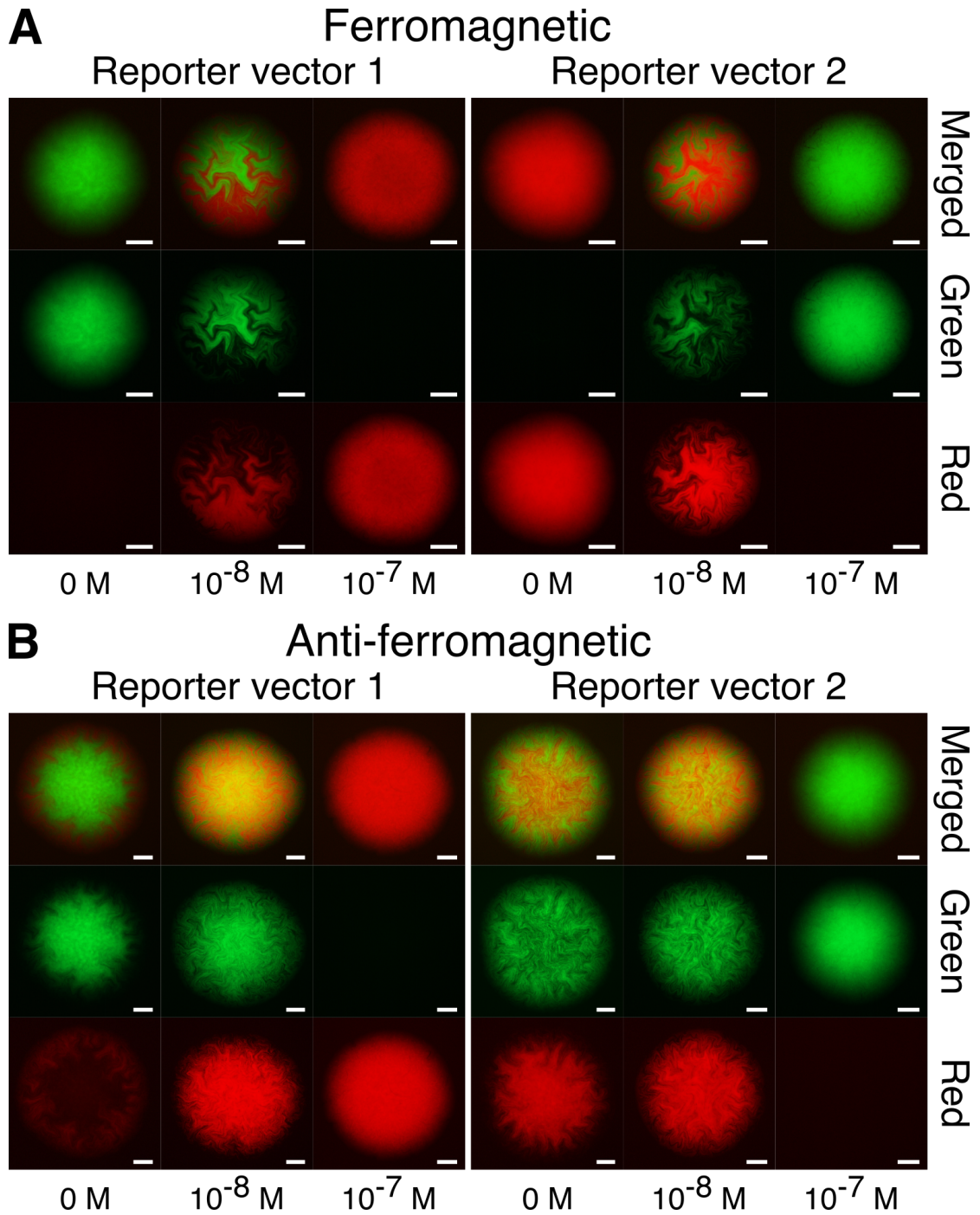


**Figure 4.4:** Self-organized patterns of red and green cellular states generated in colonies of ferromagnetic and anti-ferromagnetic rod-shaped cells. Representative images of red and green fluorescent protein patterns that emerge in colonies of rod-shaped *E. coli* cells carrying the ferromagnetic (A) or anti-ferromagnetic (B) vector along with the reporter vector 1 (left) or 2 (right). Cells were grown on solid M9-glucose medium supplemented with different concentrations of C6HSL. Images were taken approximately 14 hours after inoculation. Scale bars 100  $\mu$ m

anti-ferromagnetic colonies seem to be much smaller. As in ferromagnetic colonies, further increasing the concentration of the inducer in the medium ( $10^{-7}$  M) only produced colonies in the red (reporter vector 1) or green (reporter vector 2) state (Fig. 4.4B).

Taken together, these results showed that anti-ferromagnetic and ferromagnetic SGNs allowed the self-organization of distinctive patterns in *E. coli* colonies, as partially anticipated by the simulations (Fig. 3.1). However, the formation of fractal-like jagged patterns, characteristic of rod-shaped non-motile *E. coli* cells, made these patterns visually different from those observed in the simulations. The fractal patterns that emerge in ferromagnetic and anti-ferromagnetic colonies are the result of SGNs combined to the jagged patterns created by mechanical instabilities generated by the polar shape of cells, which propagate due to the uniaxial growth and division [100].

#### 4.2.2 Ising-like patterns in bacterial colonies of ferromagnetic and anti-ferromagnetic spherical cells

In order to analyze the pattern generated by ferromagnetic and anti-ferromagnetic SGNs without the influence of mechanical interactions described above, we used the *E. coli* mutant strain KJB24 that forms spherical cells due to a mutation in *RodA* [83]. As observed in rod-shaped cells (Fig. 4.3), increasing the concentration of C6HSL in the medium increases either the red fluorescence in colonies carrying the reporter vector 1 (Fig. 4.5A) or green fluorescence in colonies carrying the reporter vector 2 (Fig. 4.5B).

Next, we tested ferromagnetic and anti-ferromagnetic systems. To balance the effects of the higher basal expression of the promoter induced by C12HSL, spherical *E. coli* cells carrying the ferromagnetic and anti-ferromagnetic systems were also grown on solid medium supplemented with C6HSL. In accordance with the findings on colonies of rod-shaped cells, ferromagnetic colonies of spherical cells produced ferromagnetic Ising-like patterns when they were grown in the range of

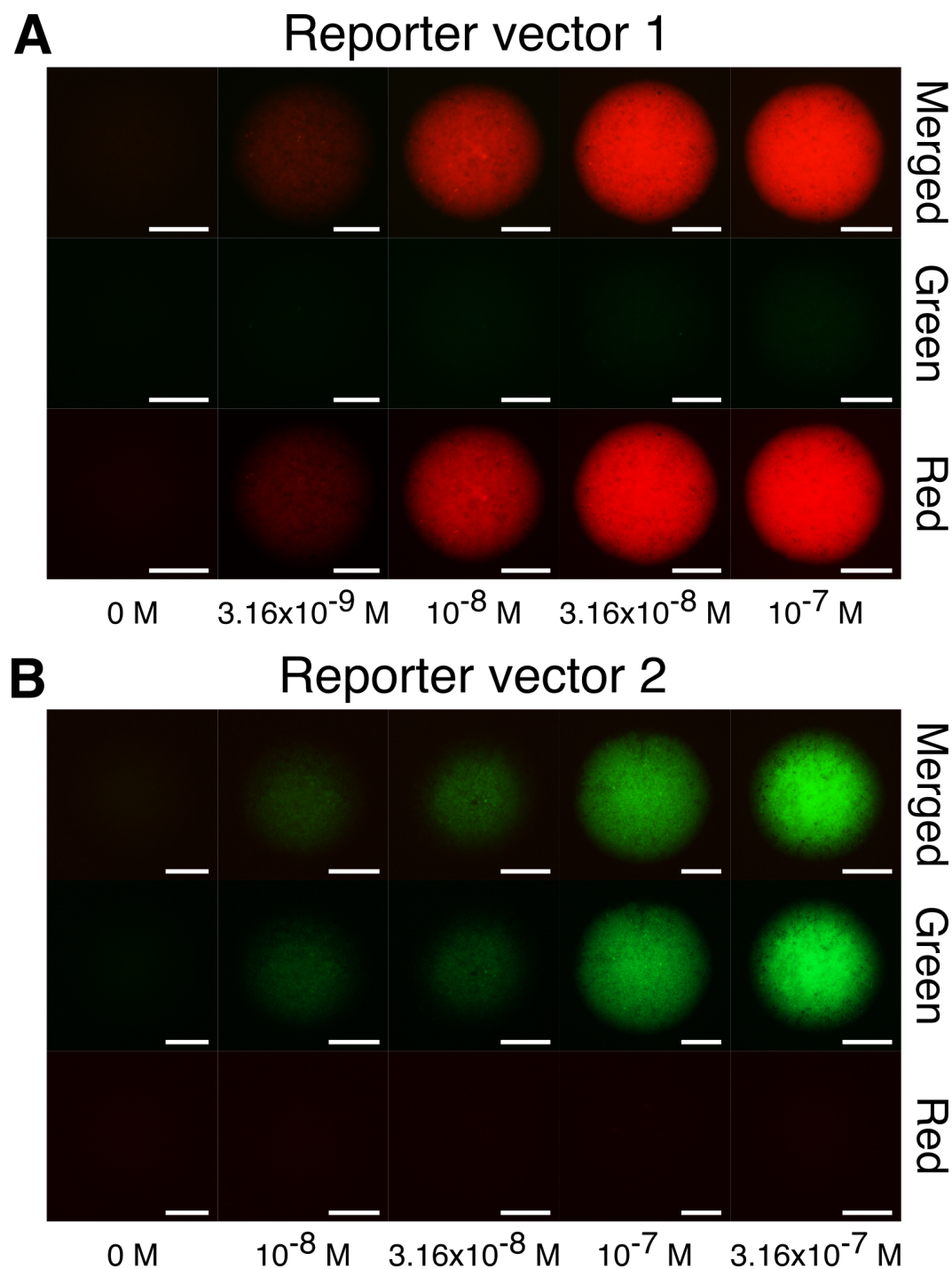


**Figure 4.5: Induction of red and green fluorescence by C6HSL in colonies of spherical cells carrying different versions of the reporter vector.** Red and green fluorescence of colonies generated from spherical cells carrying the reporter vector 1 (A) and reporter vector 2 (B) grown on solid M9-glucose medium supplemented with different concentrations of C6HSL. Images were taken approximately 18 hours after inoculation. Scale bars 100  $\mu$ m.

$10^{-8}$  M of C6HSL, regardless of the reporter vector used (Figure 4.6A). Since spherical cells are not affected by cell polarity-driven mechanical coupling observed in colonies of rod-shaped cells, the patterns that emerge in colonies of spherical cells look qualitatively more similar to the simulated colonies using the lattice model.

To compare the cellular state patterns that emerge in ferromagnetic colonies of spherical cells and the patterns observed in ferromagnetic populations of the CP-IM simulations, we calculate the Hamming distance between them (Fig. 4.7). The Hamming distance between two images of equal size is the number of pixel positions at which the value of those pixels are different. Therefore, the smaller the Hamming distance between two images, the more similar those images are. Regardless of this simple approach, the Hamming distance allows us to directly compare a set of experiments to a set of simulations. To test if ferromagnetic colonies are more similar to simulated ferromagnetic populations at the critical point, we calculated the Hamming distance between the colonies and simulated populations around the critical value of  $T$  (between  $T = 2.0$  and  $T = 2.54$ , with  $T_c = 2.27$ ) (Fig. 4.7A, red dots). Before the calculation of the Hamming distance, the images of the colonies were binarized and scaled to have the same size of the simulations. As observed before, a strong coupling between cells ( $T < T_c$ ) leads to the generation of populations with large homogeneous patches of cells in the same state. At this point, the probability of finding populations mostly in the red or green state is the same (Fig. 4.7B). This explains the great variability observed in the Hamming distance between ferromagnetic colonies and simulated populations below the critical value of  $T$  (Fig. 4.7C). Interestingly, Figure 4.7C shows that the smallest average Hamming distance is found by comparing ferromagnetic colonies of spherical cells with simulated populations close to the critical value of  $T$ . These results suggest that ferromagnetic colonies of spherical cells are more similar to the simulated populations around the critical transition, where cells located at far regions in the colonies are correlated.

Anti-ferromagnetic colonies of spherical cells, on the other hand, showed a characteristic pattern of smaller domains of red and green states at  $10^{-8}$  M of C6HSL (Figure 4.6B). Although the patterns observed in anti-ferromagnetic



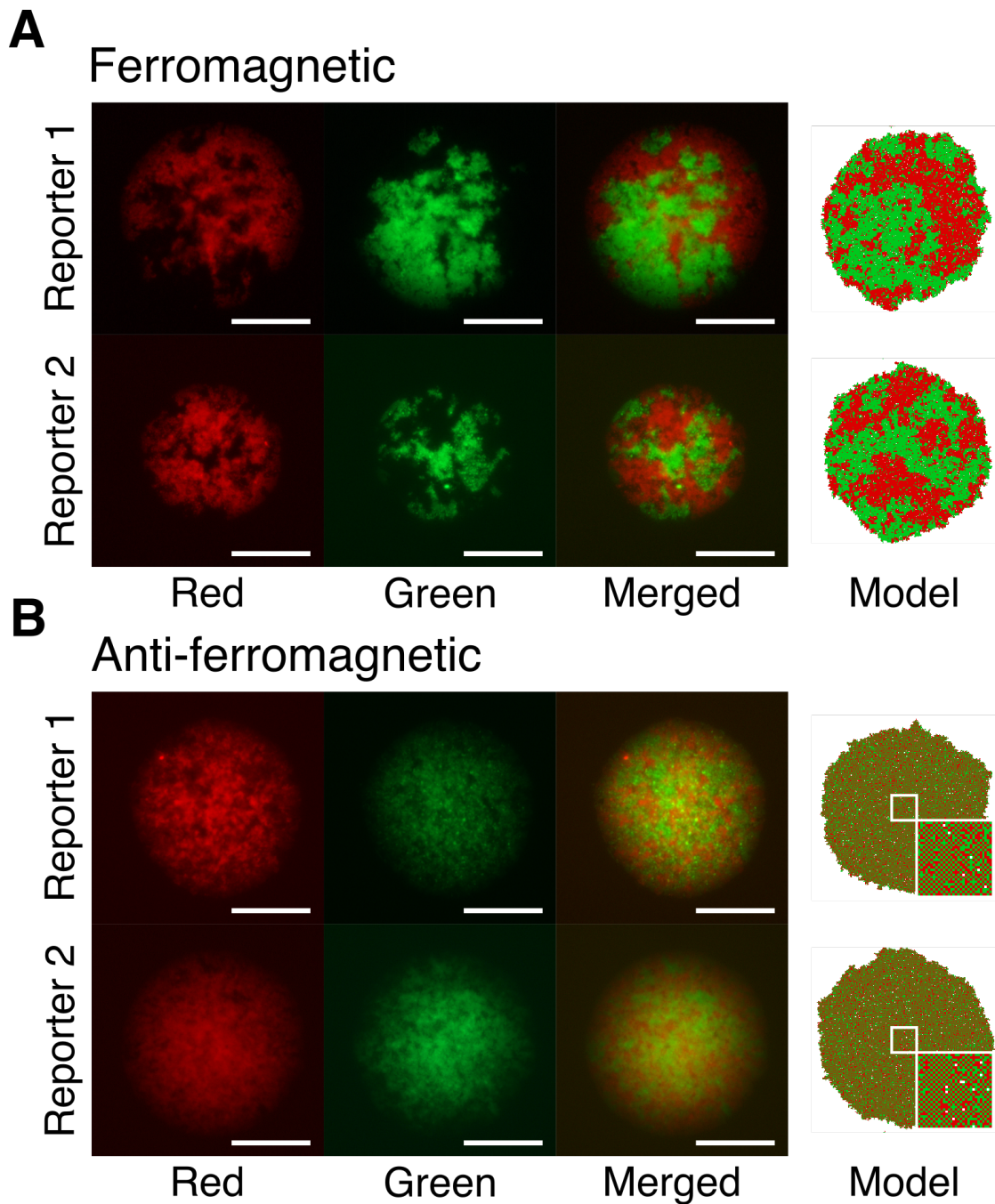


**Figure 4.6: Ising-like patterns generated in colonies of spherical cells carrying the ferromagnetic and anti-ferromagnetic gene networks.** Representative images of red and green fluorescent protein patterns that emerge in colonies of spherical *E. coli* cells carrying the ferromagnetic (A) or anti-ferromagnetic (B) vector along with the reporter vector 1 (top) or 2 (bottom). Cells were grown at a concentration of C6HSL that counteracts the bias introduced by the basal expression of the promoter induced by C12HSL. Images were taken approximately 18 hours after inoculation. Images obtained from the simulation of the Ising model during the growth of a colony are included for comparison. Scale bars 100  $\mu\text{m}$

colonies differ from those observed in CP-IM simulations (one cell in a particular state surrounded by four cells in the opposite state), the anti-ferromagnetic SGN allowed the generation of small clusters of cells (compared with those observed in ferromagnetic colonies) in the same state surrounded by clusters of cells in the opposite state. Figure 4.8 shows a summary of the patterns observed in colonies of rod-shaped and spherical cells carrying the coupled two-state systems and in populations of cells obtained with the CP-IM simulations.

As shown in Figure 4.9, the cellular state patterns observed in ferromagnetic and anti-ferromagnetic colonies of spherical cells are qualitatively different from the patterns that emerge in a population of spherical *E. coli* cells dominated only by a segregation mechanism [101], where there is no coupling between the states of cells. In these colonies, the first cell that originates the colony contains two plasmids: one with a gene encoding a red fluorescent protein, and another with a gene encoding a green fluorescent protein. The patterns generated in these colonies are the result of the segregation of these plasmids during cell division: once a cell loses one of these plasmids, its cellular state and the cellular state of all its progeny are fixed, generating sharp boundaries between the cellular state domains. These results support the idea that the patterns observed in ferromagnetic and anti-ferromagnetic colonies are the result of the bi-stability and local interactions generated by the SGNs.

To test the ability of the ferromagnetic system to act as a toggle-switch [45] in solid medium, which means the ability to turn ON one cellular state while turning OFF the other depending on the repressor produced, we grew ferromagnetic cells in solid medium supplemented with the coupling signals C6HSL or C12HSL and the inhibitors of the repressors TetR (ATC) and LacI (IPTG). These inhibitors bind to the repressors, preventing them from inhibiting the expression of genes. Thus, depending on the inhibitor present in the medium, one state cannot be repressed, resulting in the eventual repression of the other state. This allowed us to push the system toward one or the other cellular state. Figure 4.10A shows that growing ferromagnetic rod-shaped cells in the presence of IPTG leads to the generation of colonies in green (reporter vector 1) or red (reporter vector 2) state,

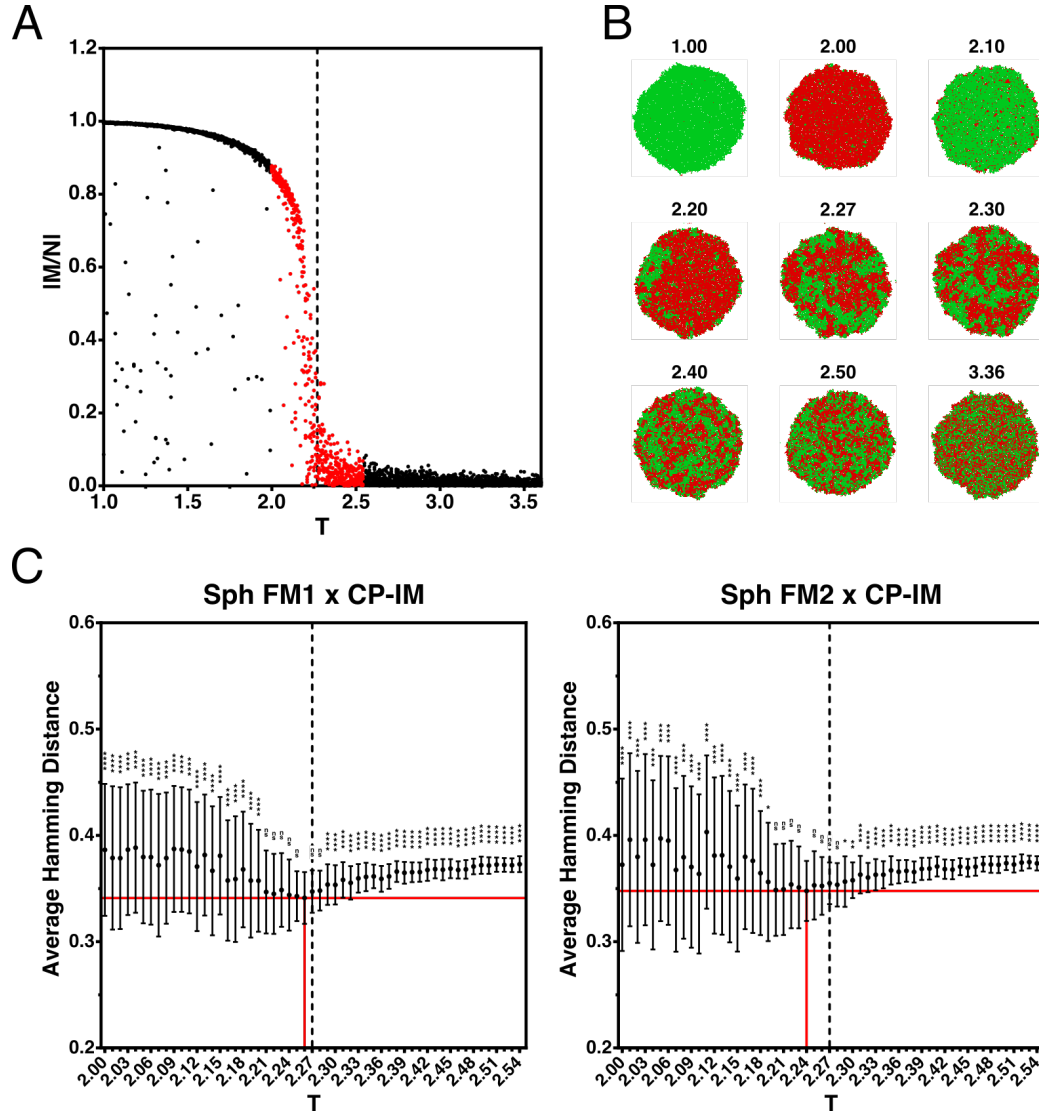


**Figure 4.7: Hamming distance between ferromagnetic colonies of spherical cells and ferromagnetic populations obtained from CP-IM simulations.** (A) Magnetization per site  $|M/N|$  as a function of  $T$  for simulated ferromagnetic populations. Dotted vertical line marks the critical value of  $T$  ( $T_c = 2.27$ ). Red dots correspond to the simulations used to calculate the Hamming distance in C. 10 simulations per each value of  $T$  (B) Images of simulated ferromagnetic populations at different values of the control parameter  $T$ , highlighting that the probability of finding populations in the red or green state below  $T_c$  is the same. (C) Hamming distance calculated between ferromagnetic colonies of spherical (Sph) cells carrying the reporter vector 1 (left, FM1) or 2 (right, FM2) and the ferromagnetic populations of the CP-IM simulations (CP-IM) around  $T_c$ . Black dots and error bars correspond to the mean  $\pm$  the standard deviation of the Hamming distance calculated between the colonies (42 ferromagnetic 1 and 65 ferromagnetic 2 colonies) and 10 simulated populations for each value of  $T$ . The value of the Hamming distance was divided by the total number of pixels. Dotted vertical lines mark the critical value of  $T$ , and red solid lines mark the smallest average value of the Hamming distance. To compare the smallest average value of the Hamming distance with each other value, statistical analysis was performed using an ordinary One-Way ANOVA, followed by Dunnett's multiple comparisons test. ns (not significant):  $P > 0.05$ , \*:  $P \leq 0.05$ , \*\*:  $P \leq 0.01$ , \*\*\*:  $P \leq 0.0001$ .



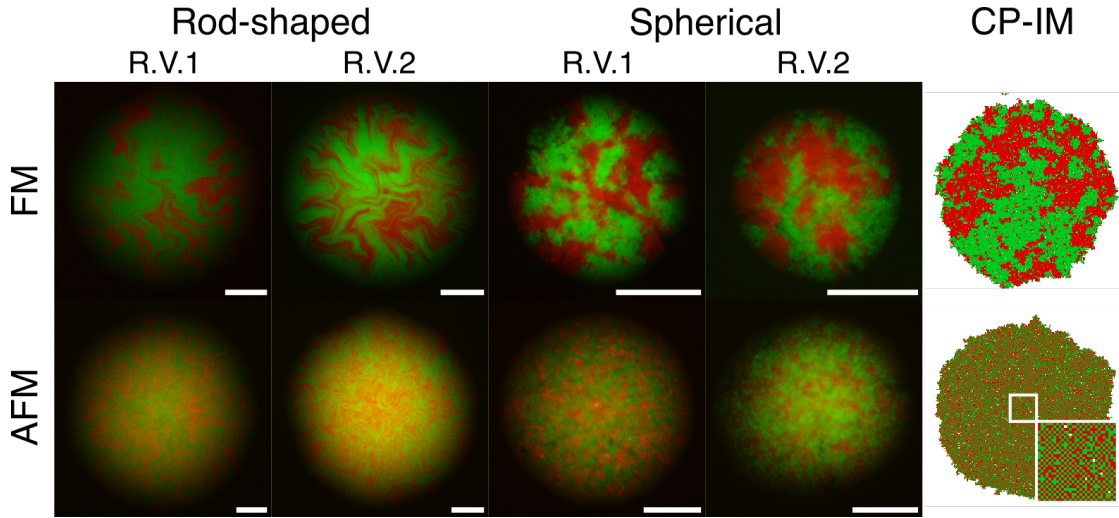


**Figure 4.8: Cellular state patterns generated by the coupled two-state systems.** Representative images of the fluorescent patterns generated in colonies of rod-shaped and spherical *E. coli* cells carrying the ferromagnetic (FM) or anti-ferromagnetic (AFM) systems with the reporter vector 1 (R.V.1) or 2 (R.V.2). Cells were grown on solid medium supplemented with a concentration of C6HSL that counteracts the bias introduced by the basal expression of the promoter induced by C12HSL. Images were taken approximately 14 (rod-shaped cells) and 18 (spherical cells) hours after inoculation. Scale bars 100  $\mu\text{m}$ . Images of population with ferromagnetic or anti-ferromagnetic interactions obtained from the CP-IM simulations are included for comparison. Insets show a detail of the checkerboard-like pattern generated in anti-ferromagnetic populations.

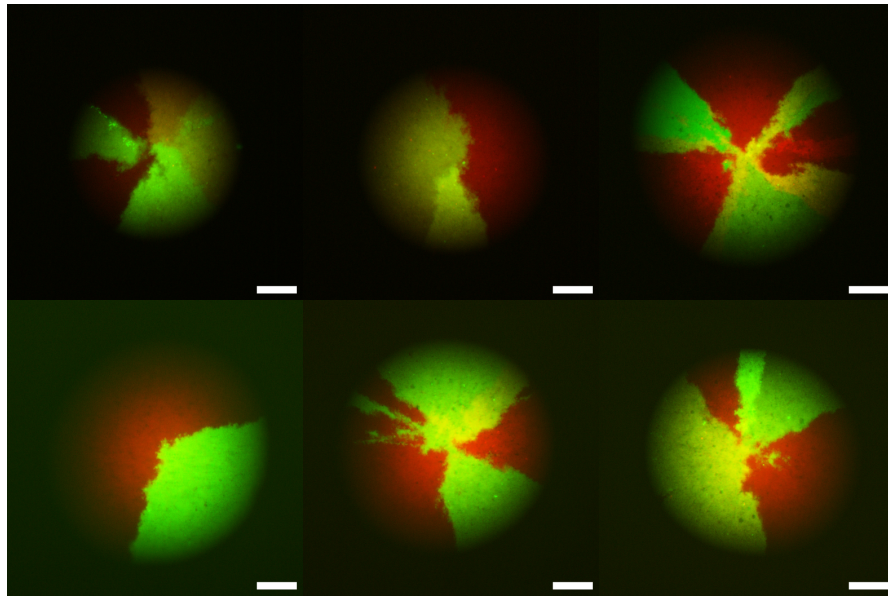


**Figure 4.9: Sharp boundaries generated between cellular state domains in colonies of spherical cells without a coupling between them.** Fluorescent patterns that emerge in colonies of spherical *E. coli* cells due to the segregation of cellular states. Each cell that gives rise to a colony contains two plasmids with genes encoding different fluorescent proteins, which segregate during the growth of the colony. Scale bars 100  $\mu\text{m}$ .

while growing cells in the presence of ATC produces the opposite effects, i.e. the generation of colonies in red (reporter vector 1) or green (reporter vector 2) state. The cellular state of colonies grown in the presence of these inhibitors showed to be independent of the coupling signal present in the medium, since the state of the colonies remained the same regardless of the coupling signal in which they were grown. These results suggest that the repressors are effectively fixing the state of cells when they are being produced, allowing the generation of a bi-stable system in solid medium. Growing cells in the presence of both inhibitors, and thus blocking both repressors at the same time, allowed cells to adopt the cellular state induced by the coupling molecule present in the medium. This result showed that, in absence of repressors, cells adopt the state dictated by the coupling signals they sense. The same results observed in ferromagnetic colonies of rod-shaped cells are reproduced in ferromagnetic colonies of spherical cells (Fig. 4.10B), suggesting that the behaviour of the SGNs is the same in both strains.

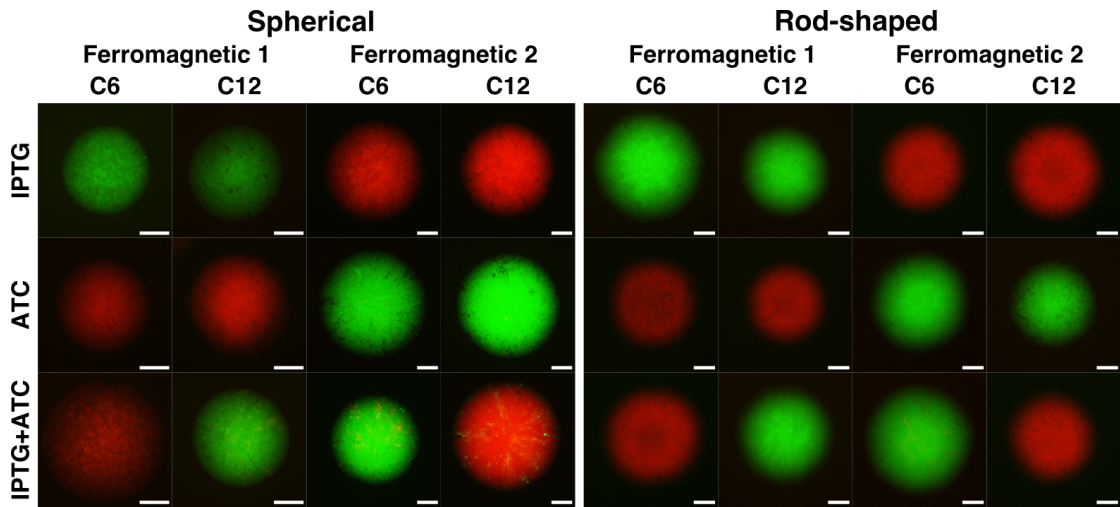


**Figure 4.10: Cellular state switch in ferromagnetic colonies grown on solid medium supplemented with the inhibitor of the repressors.** Representative images of ferromagnetic colonies of spherical and rod-shaped cells that carry the reporter vector 1 (Ferromagnetic 1) or the reporter vector 2 (Ferromagnetic 2). Cells were grown on M9-glucose solid medium supplemented C6HSL or C12HSL and with IPTG, ATC or both inhibitors. Scale bars 100  $\mu\text{m}$ .

Taken together, these results suggest that the two-state and coupled genetic networks allow the self-organization of patterns of short- and long-scale domains similar to those observed in the simulations of the two-dimensional Ising

model, in which the size of the domains of red and green cellular state depend on the type of interactions, ferromagnetic or anti-ferromagnetic.

### 4.2.3 Spatial correlations in ferromagnetic and anti-ferromagnetic bacterial colonies

To quantitatively compare the patterns generated in anti-ferromagnetic and ferromagnetic colonies of rod-shaped and spherical cells, we calculated the spatial autocorrelation function (sACF) [90] of these colonies (Fig. 4.11A). The sACF is a measure of the order in a system since it describes how the correlation between any two microscopic variables (for instance, the state of each cell in a colony) changes on average as the separation between these variables changes [102]. A value of 1 of the sACF means a perfect correlation, a value  $-1$  means a perfect anti-correlation, while a value of 0 means no correlation between the variables. Since the sACF allows the calculation of the average distance at which the correlation between the two variables becomes 0, it allows to determine the characteristic size of the cellular state domains that emerge in the colonies carrying the two-state and coupled gene networks.

In rod-shaped cells, the correlation function curve of anti-ferromagnetic colonies decays much faster than the curve of ferromagnetic colonies (Fig. 4.11A top), suggesting that the average distance at which two cellular states correlates is shorter in the anti-ferromagnetic colonies. This difference in the decay of the curves is the same regardless of the reporter vector used, suggesting that this behaviour is an intrinsic property of the systems. The same difference in the decay behaviour observed in colonies of rod-shaped cells is also observed between the correlation curves of ferromagnetic and anti-ferromagnetic colonies of spherical cells (4.11B). Individual analysis of anti-ferromagnetic colonies of rod-shaped and spherical cells revealed that most of the colonies show negative values on the correlation curve, suggesting the existence of short-range anti-correlations (inset of Fig. 4.11). However, this oscillatory behaviour with positive and negative values is lost when the data is averaged. Interestingly, the shape and decay behaviour

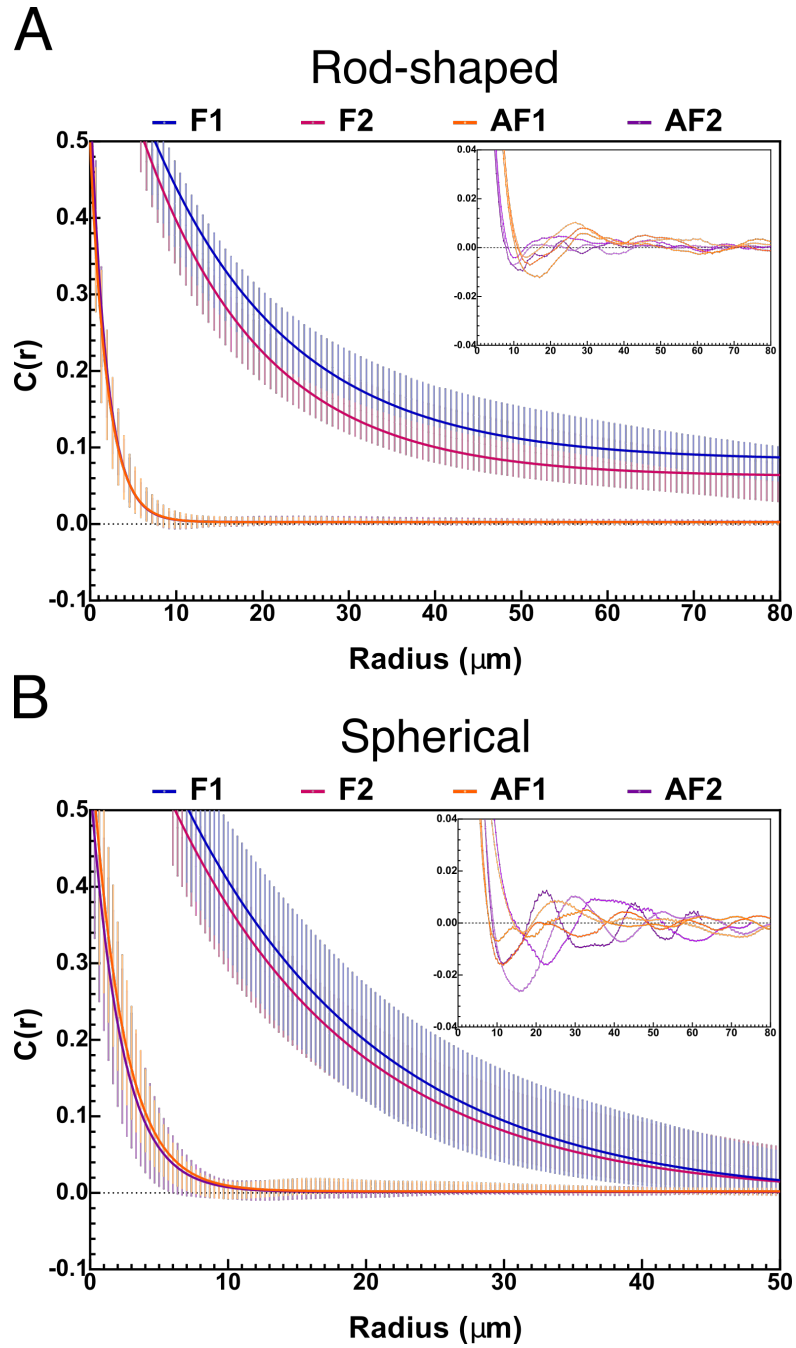


**Figure 4.11: Spatial autocorrelation function of colonies carrying the two-state and coupled gene networks.** Difference in the decay behaviour of the sparial autocorrelation function  $C(r)$  of the images of colonies generated from rod-shaped (A) and spherical (B) *E. coli* cells carrying the ferromagnetic and anti-ferromagnetic systems. Points and error bars correspond to the mean  $\pm$  the standard deviation of around 40 colonies for each system, and lines correspond to the best fit of the exponential decay equation  $y = y_0 \exp(-x/b) + C$  to the data. Insets correspond to a magnification around zero of the sACF of some individual anti-ferromagnetic colonies showing its oscillating behaviour with negative and positive values that is lost when the data is averaged. AF1 and AF2: Anti-ferromagnetic systems with reporter vectors 1 and 2; F1 and F2: Ferromagnetic system with reporter vectors 1 and 2; LM: Lattice model.

of the sACF curves of colonies generated from rod-shaped and spherical *E. coli* cells are similar, suggesting that the mean size of the cellular state domains that emerge in the colonies is not affected by cell shape. To obtain the mean size of the cellular state clusters generated in these colonies, we fitted the exponential decay equation  $y = y_0 \exp(-x/b) + C$  to the data obtained from the computation of the sACF of the colonies. In this equation,  $b$  correspond to the length constant, which is an estimation of the mean size of the cellular states patches generated in the colonies.

	Anti-ferromagnetic		Ferromagnetic	
	R.V.1	R.V.2	R.V.1	R.V.2
Rod-shaped	$1.96 \pm 0.54$	$1.85 \pm 0.38$	$15.82 \pm 2.86$	$14.21 \pm 2.83$
Spherical	$2.23 \pm 0.46$	$2.12 \pm 0.62$	$15.05 \pm 5.11$	$14.06 \pm 3.87$

**Table 4.4:** Length constants of ferromagnetic and anti-ferromagnetic colonies of rod-shaped and spherical *E. coli* cells. Values correspond to the mean  $\pm$  the standard deviation (in  $\mu\text{m}$ ) of the sACF of around 40 colonies for each system.

Table 4.4 shows the values of the length constants calculated using the sACF of ferromagnetic and anti-ferromagnetic colonies of rod-shaped and spherical cells. As suggested by the patterns observed in colonies of cells carrying the SGNs, the mean size of the cellular state clusters that emerge in ferromagnetic colonies is larger than the mean size of the clusters that emerge in anti-ferromagnetic colonies. This difference in the mean size showed to be independent of the reporter vector (R.V.) used: in colonies of rod-shaped cells, the mean size of the clusters in ferromagnetic colonies is approximately 8.1 (R.V.1) and 7.7 (R.V.2) times larger than the mean size of clusters in anti-ferromagnetic colonies, while in colonies of spherical cells is approximately 6.7 (R.V.1) and 6.6 (R.V.2) times larger. Interestingly, as the shape of the correlation curves and simulations suggested, a t-test revealed that there are no significant differences between the values of the length constants of ferromagnetic colonies generated from rod-shaped and spherical cells. This result suggest that the mean size of the cellular state domains emerging in ferromagnetic colonies is independent of the shape of the cells.

Taken together, these results show that the ferromagnetic system allows the generation of spatial correlations on larger scales than those generated by the

anti-ferromagnetic system, and that the emergence of spatial correlations of gene expression in a spatially arranged population are independent of the cell shape and the underpinning mechanical forces, depending only on the type of interactions (ferromagnetic or anti-ferromagnetic), as observed in the simulations.

#### 4.2.4 Percolation theory

To further characterize the behaviour of the ferromagnetic system, we analyzed the distribution of the size of cellular state clusters that emerge in colonies of cells carrying this system. As seen in Figure 4.12, the probability distribution  $P(S)$  of cluster size  $S$  for ferromagnetic colonies of rod-shaped and spherical cells shows a scale invariant distribution with a noisy tail of the form  $P(s) \sim s^{-\gamma}$ . The values of the scaling exponent  $\gamma$  calculated for the ferromagnetic systems showed to be consistent with the exponent of the distribution of cluster sizes near the critical percolation threshold, which follows a power-law decay with an exponent of 2.055 [103] (Rod-shaped: R.V.1 = 2.18, R.V.2 = 2.09. Spherical: R.V.1 = 2.13, R.V.2 = 1.87). The scaling exponent of the colonies also showed to be consistent with the value of  $\gamma$  calculated from ferromagnetic populations simulated with the lattice model at  $T = T_c$  ( $\gamma = 1.96$ ). Percolation theory describes the transition of a system from having only localized short-range connections to the emergence of a connected cluster that spans the entire system at and above the critical percolation threshold. Thus, the values of the scaling exponent found in ferromagnetic colonies suggest that there is always a probability of finding a very large cluster of a cellular state spanning the whole colony [104]

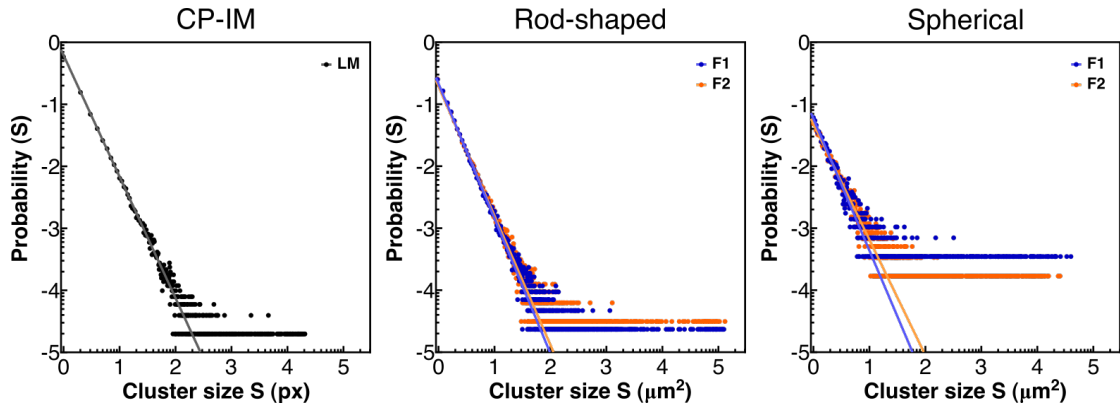


**Figure 4.12: Ferromagnetic system at the percolation threshold.** Probability distribution  $P(S)$  ( $\log_{10} - \log_{10}$  plots) of the cluster size  $S$  (in pixels for the CP-IM simulations and  $\mu\text{m}^2$  for the colonies) for ferromagnetic populations obtained from the CP-IM simulations (left) and ferromagnetic colonies of rod-shaped (middle) and spherical (right) cells. Solid lines correspond to the best fit of the data to equation  $P(s) = A * s^{-\gamma}$ . Values on x-axis and y-axis are the  $\log_{10}$  of the values of the cluster size. F1 and F2: ferromagnetic system with reporter vectors 1 and 2; CP-IM: CP-IM simulations

# Chapter 5

## Microfluidics

### 5.1 Dynamics of the two-state and coupled systems in micro-fabricated environments

#### 5.1.1 The classic mother machine and the addition of side channels

In order to study the dynamics of ferromagnetic and anti-ferromagnetic systems at single cell level we used a microfluidic device known as "the mother machine". This device was designed to follow steady-state growth and division of a large number of cells [105]. The design and fabrication of the mother machine was carried out in the laboratory of Dr. Peter Galajda at the Biological Research Center in Szeged, Hungary, with the help of his research group members. The mother machine consists of 3000 dead-end growth channels of approximately  $25\ \mu\text{m}$  in length,  $1\ \mu\text{m}$  in width and  $1\ \mu\text{m}$  in height, which are connected at right angles to a central channel of 3 cm in length and  $100\ \mu\text{m}$  in width (Fig. 5.1). This central channel allows the injection of a constant flow of liquid medium, resulting in the diffusion of fresh medium into the growth channels and the removal of waste and cells that emerge from the growth channels. The design of the mother machine allows the growth of only one row of cells in each growth channel, which is ideal to study the



dynamics of the adoption of cellular states in one dimension. The construction of the microfluidic devices was carried out by soft lithography technique (Section 2.7). Figure 5.1B and 5.1C shows scanning electron microscopy images of a device constructed in this way.

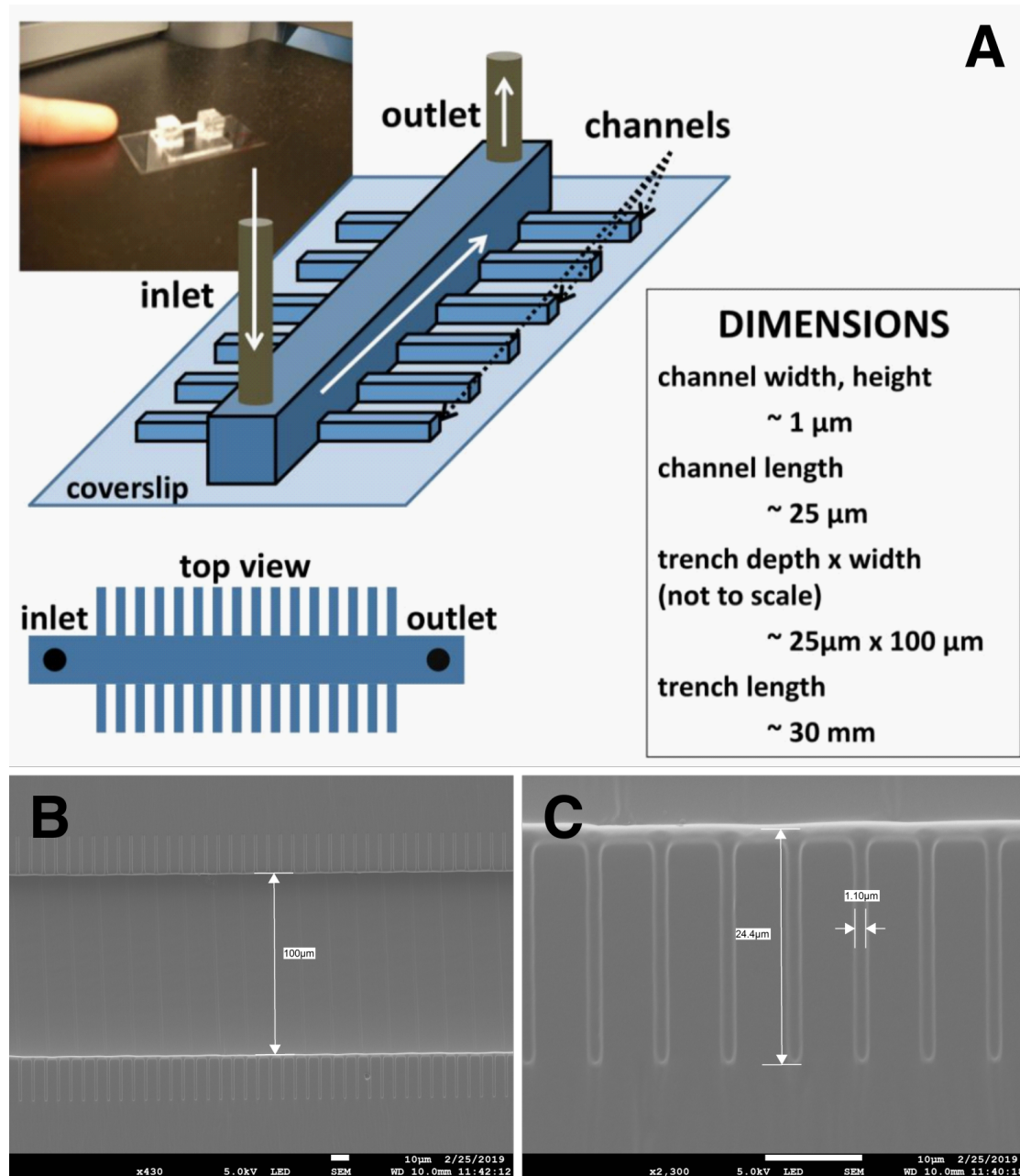


**Figure 5.1: The mother machine.** (A) Design and dimensions of the original mother machine. Images were taken from [105]. (B-C) Scanning Electron Microscopy images of the mother machine we built with the help of Dr. Peter Galajda and his research group members. The images show growth channels connected to the central channel of 100  $\mu\text{m}$  in width (B) and a detail of the growth channels of approximately 25  $\mu\text{m}$  in length and 1  $\mu\text{m}$  in width (C). These images correspond to the surface of the PDMS after being removed from the wafer mold that contains the design of the mother machine.

To study the behaviour of our synthetic genetic networks (SGNs) at single cell level, ferromagnetic and anti-ferromagnetic *E. coli* rod-shaped cells were injected into the devices using a syringe. However, we were not able to introduce cells into the growth channels of the mother machine. In response to this, we constructed another version of the mother machine adding two side channels (Fig. 5.2A). These side channels are also connected to the growth channels (Fig. 5.2B), but the opening that connects the growth channels with side channels is smaller than the opening that connects the growth channels with the central channel ( $0.8 \mu\text{m}$  in width for growth-side channel compared to  $1.2 \mu\text{m}$  in width for growth-central channel) (Fig. 5.2C). This device was constructed in the same way as the classic mother machine. Figure 5.3 shows scanning electron microscopy images of this version of mother machine.

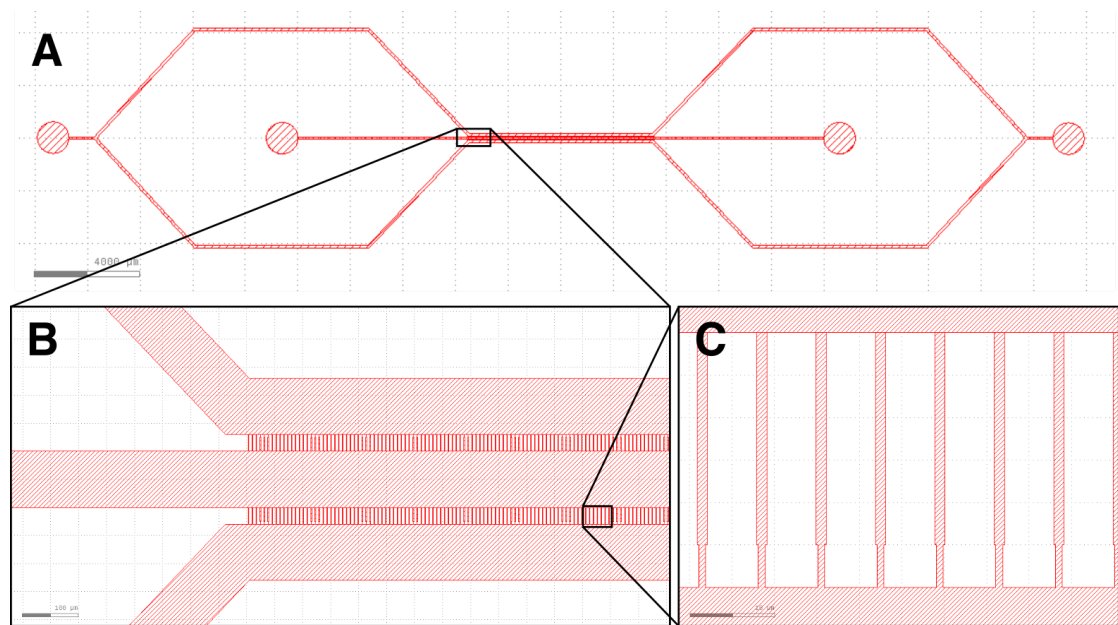


**Figure 5.2: The mother machine with two side channels.** Design of a new version of the mother machine with the addition of two side channels. The design was drawn using the Klayout software. (A) Full view of the design. (B) Detail of the design showing the connections between the central, growth and side channels. (C) Detail of the growth channel connected to the central channel (top) and the side channel (bottom). The growth channels are connected to the side channels through an opening of  $0.8 \mu\text{m}$  in width, smaller than the opening that connects them to the central channel.

With this design, we were able to easily introduce cells into each growth channel of the device using a syringe loaded with a low-density suspension of cells ( $\text{OD}_{600}$  0.2). To grow cells at  $37^\circ\text{C}$  under the microscope, we built a temperature

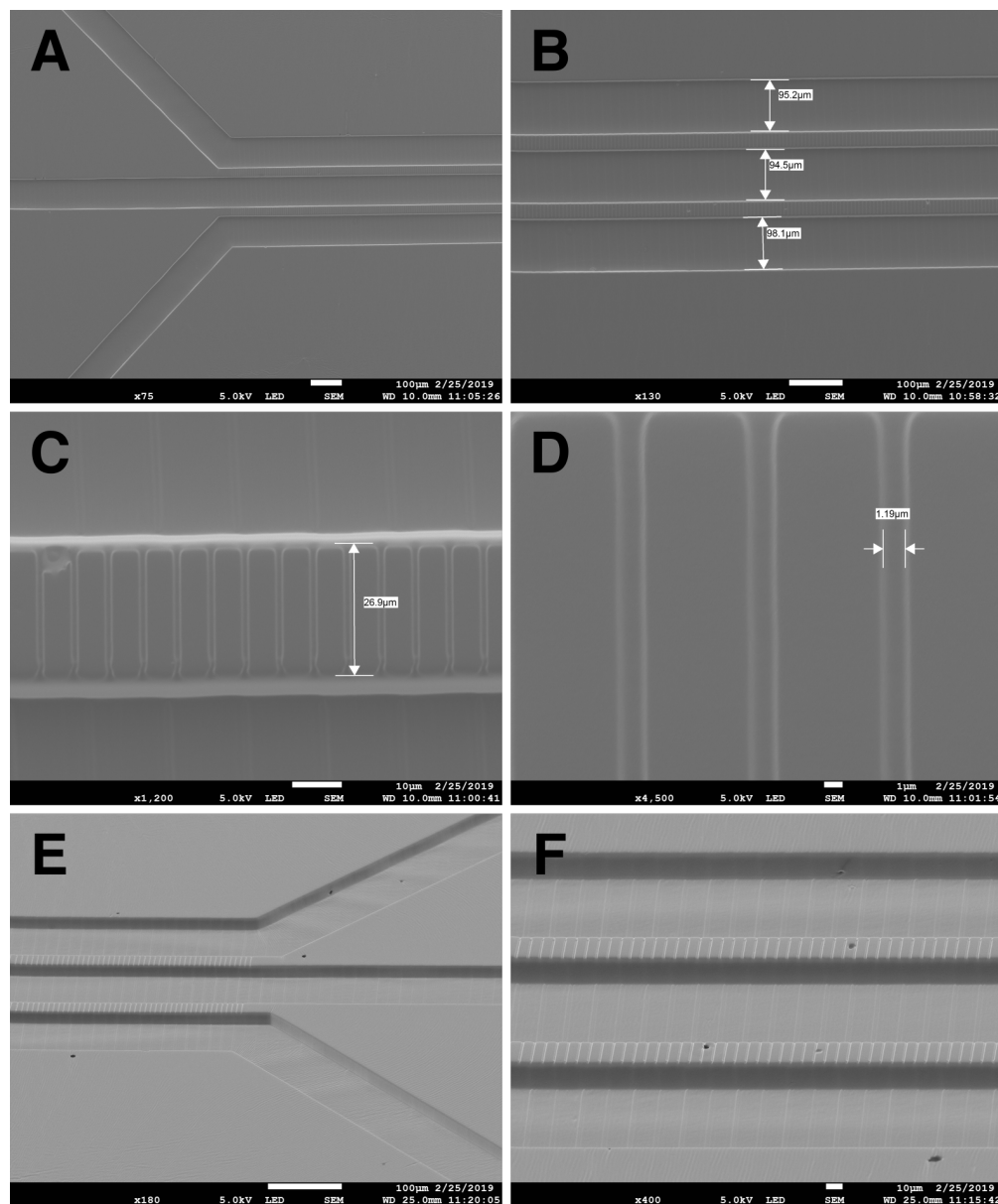


**Figure 5.3: Scanning Electron Microscopy images of the mother machine with side channels.** The images show in different detail the central channel and the side and growth channels of the modified version of the classic mother machine. (A-D) Images of a top views of the device. (E-F) Images of a device tilted 60 degrees.

control system with the help of Dr. Timothy Rudge that allows heating a sheet of glass to the desired temperature. The devices loaded with cells were deposited on this glass sheet heated at 37 °C and the tubes that allow the entry of fresh medium and the exit of the wastes were connected to the inlet and outlet of the device. To observe the growth and fluorescence of cells within the growth channels, time-lapse microscopy experiments were performed, taking pictures every 10 minutes. Figure 5.4 shows some examples of ferromagnetic (Fig. 5.4A) and anti-ferromagnetic (Fig. 5.4B) cells growing in the growth channels of the modified version of the mother machine at different concentrations of the inducer C6HSL. Each image is a YZ orthogonal view of the time-lapses created with Imagej. This means that the Y-axis of each image corresponds to the Y-axis of the images of the time-lapse (which is parallel to the growth channels) and the X-axis corresponds to the time of the experiment. Thus, each image is a temporal montage (composed of several slices corresponding to each time step of the time-lapse) of a single growth channel of the device showing the growth and division of cells within that channel. While the addition of side channels to the classic mother machine allowed cells to easily enter almost every growth channel in the device, during the course of the experiments, cells were also able to exit the growth channels through the opening that connects these channels with the side channels. Thus, this device allowed cells to exit the growth channels on both sides, i.e. cells are able to emerge from the growth channels towards the central and side channels, as can be seen for both ferromagnetic and anti-ferromagnetic cells growing in the modified version of the mother machine in Figure 5.4 (cells crossing both dotted lines).

Although the exit of cell from both sides of the growth channels made difficult the interpretation of the data obtained from cells growing in the mother machine with side channels, it allowed us to make two interesting observations: *i*) even at high concentrations of C6HSL, ferromagnetic cells cannot change states in the conditions tested (Fig. 5.4A), and *ii*) the probability that anti-ferromagnetic cells can change state depends on the concentration of C6HSL added to the medium (Fig. 5.4B). This last observation was particularly interesting because the behaviour of cells within the growth channels suggested that *i*) in absence of C6HSL

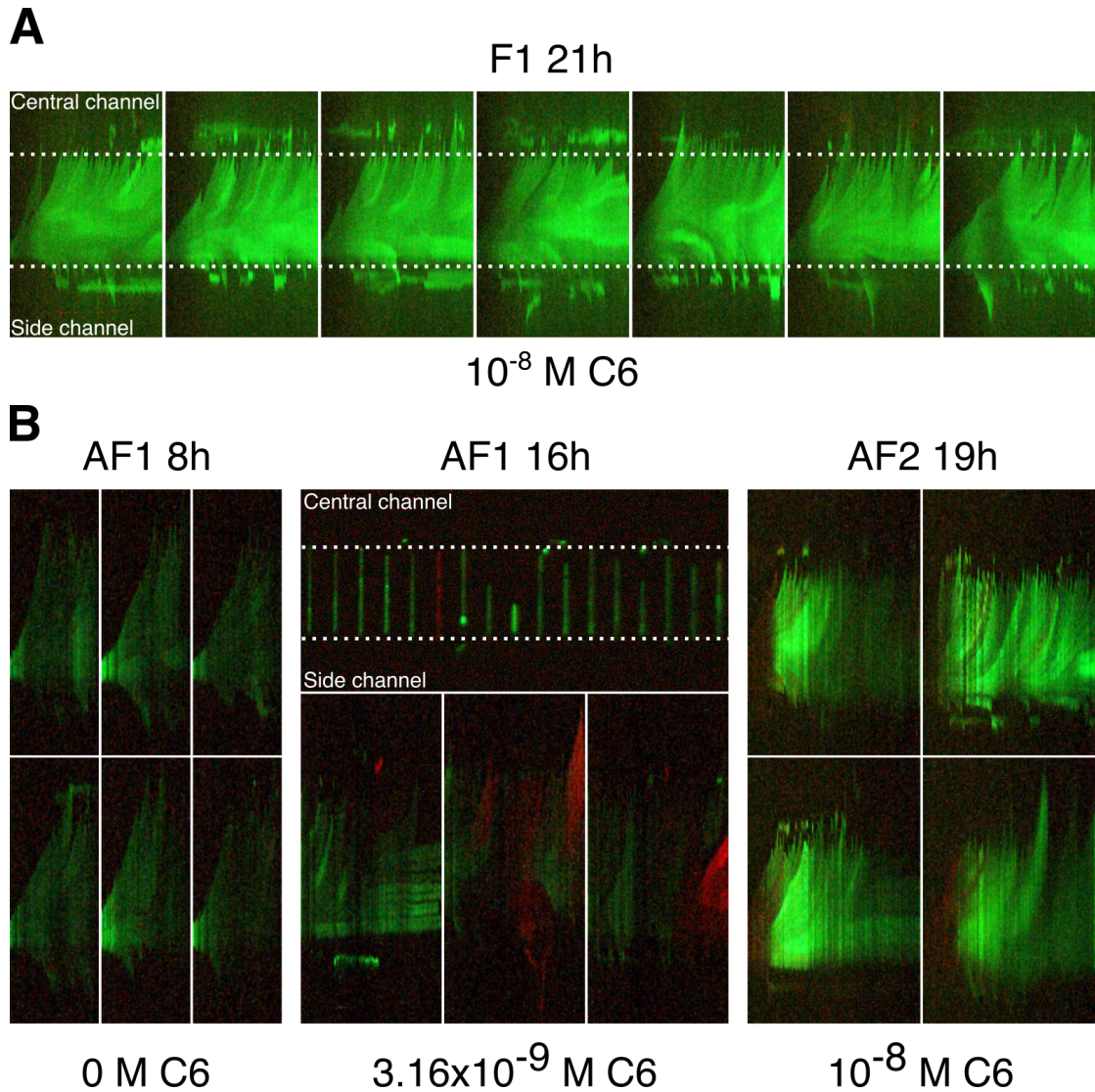


**Figure 5.4: Behaviour of ferromagnetic and anti-ferromagnetic cells in the mother machine with side channels.** Temporal montages of single growth channels of the modified version of the mother machine showing ferromagnetic (A) and anti-ferromagnetic (B) cells growing at different concentrations of the coupling signal C6HSL (C6). Dotted white lines mark the boundary between the growth channels and the central (top dotted lines) and side (bottom dotted lines) channels (see image 5.3C for a reference), showing that cells exit the growth channels on both ends. The middle-top image in B shows the growth channels of a device filled with cells at the beginning of the experiment. F1: Ferromagnetic system with reporter vector 1; AF1 and AF2: Anti-ferromagnetic systems with reporter vectors 1 and 2. Photographs were taken every 10 minutes for the time indicated in each image. The montages were created using the Fiji [88] distribution of ImageJ.



(0 M C6HSL), anti-ferromagnetic cells cannot change state (Fig. 5.4B left), *ii*) a high concentration of C6HSL ( $10^{-8}$  M C6HSL) allows cells to change state only once, and then they remain in the state dictated by the inducer (Fig. 5.4B right), and *iii*) an intermediate concentration of C6HSL ( $3.16 \times 10^{-9}$  M C6HSL) allows cells to show both previous behaviours, but they can also change state multiple times during the course of the experiment (Fig. 5.4B middle). However, since the use of this device resulted in the loss of the mother cells (the cells at the end of the growth channels), it is difficult to determine if it is the same cell that can change state several times during the course of the experiment or if it is the daughters who are changing state. Therefore, we decided to try again with the classic mother machine.

After several attempts, we were able to fill a good number of growth channels with cells (approximately 80% of the channel with at least one cell) using a syringe loaded with an overnight culture concentrated 50 times. To prevent the adhesion of cells to the PDMS surface, 0.1% of bovine serum albumin (BSA) was added to the overnight culture before the concentration of cells. Unfortunately, not all cells loaded into the mother machine in this way were able to grow within the growth channels, limiting the amount of data we were able to acquire. However, the data obtained from the experiments with the classic mother machine confirmed the behaviour observed in the mother machine with lateral channels: ferromagnetic cells cannot change states even at high concentrations of C6HSL (Fig. 5.5A), and the concentration of C6HSL added to the medium determines the probability with which anti-ferromagnetic cells can change states (Fig. 5.5B and C).

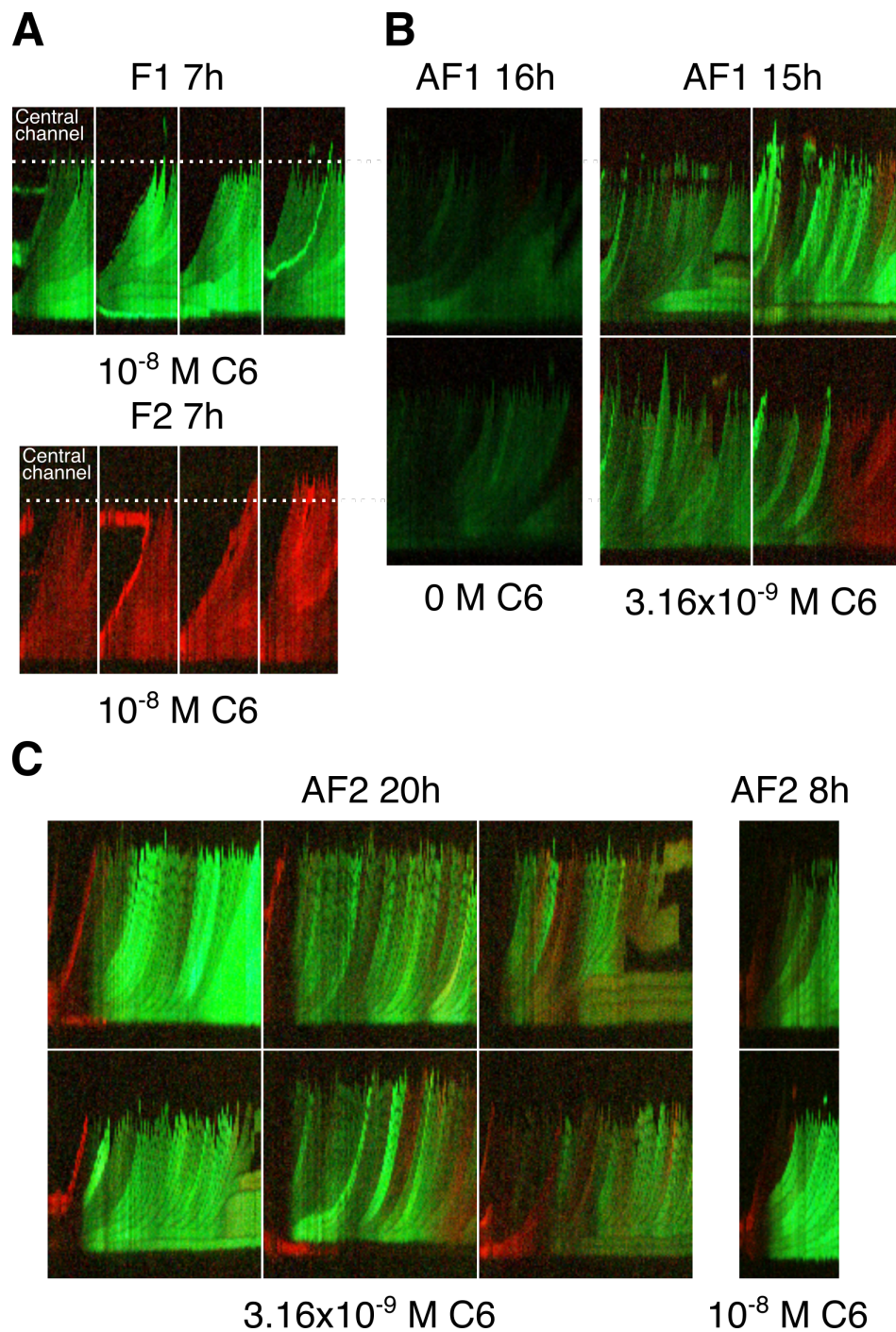


**Figure 5.5: Ferromagnetic and anti-ferromagnetic cells growing inside the growth channels of the classic mother machine.** Temporal montages of single growth channels of the mother machine showing ferromagnetic (A) and anti-ferromagnetic (B-C) cells growing at different concentrations of the C6HSL (C6). Dotted lines mark the boundary between the growth channels and the central (see image 5.1C for a reference). F1 and F2: Ferromagnetic systems with reporter vector 1 and 2; AF1 and AF2: Anti-ferromagnetic systems with reporter vectors 1 and 2. Photographs were taken every 10 minutes for the time indicated in each image. The montages were created using the Fiji [88] distribution of ImageJ.

# Chapter 6

## Discussion and Conclusions

### 6.1 Short-range two-state coupling

Due to the crucial role that it plays in the self-organization of biofilms, tissues and other spatially arranged cellular systems, the understanding of how gene expression correlations emerge from local gene network dynamics has been a fundamental problem in biology. In addition to organogenesis and morphogen-based patterns that emerge during the development, more elementary mechanisms such as ecological interactions and metabolic coupling can also give rise to ordered structures in spatially-distributed microbial populations [10–14, 61]. The work described here provides resources and a theoretical framework that captures the principles of how both short- and long-range correlations are able to self-organize from locally-interacting networks. Using the CP-IM simulations, we showed that cells following Ising-like rules (two cellular states coupled through short-ranged interactions) are able to generate self-organized patterns of gene spatial correlations in a bi-dimensional space. In absence of external perturbations, the simulations showed that the patterns that emerge in a population depend on the type of interaction and the coupling strength between cells, but not on the cell-shape. A system with ferromagnetic-like interactions (neighbours stabilizing the same phenotypes) allows the generation of positive gene spatial correlations, while



anti-ferromagnetic-like interactions (neighbours stabilizing different phenotypes) allow the emergence of negative spatial correlations. In both cases, the coupling strength between cells allow the exploration of different spatial configurations of gene expression. It has recently been shown that short-ranged interactions (on the order of a few cell lengths) govern the dynamics of microbial communities [27], suggesting that metabolic coupling between cellular states is a mechanism commonly used in bacteria. As showed by the simulations, localized interactions between individual cells can propagate in space to determine the properties of the whole community.

Although the use of a more complex versions of the classical Ising model, such as a dynamical Ising model with memory [106], has shown to be useful to study the dynamics of the behaviour of metapopulations, our model does not take into account any particular mechanism that underlays the generations of patterns, but simply shows the emergence of a macroscopic behaviour based on local interactions. These findings suggest that bi-stability and local coupling are sufficient for the emergence of global coherent structures reminiscent of the scale-invariant (ferromagnetic) and "checkerboard-like" (anti-ferromagnetic) patterns observed in 2D Ising model simulations at phase transitions, supporting the critical role that bi-stability and coupling play in the emergence of self-organized patterns of gene expression [107].

As predicted by the model, the construction of synthetic genetic network (SGNs) in bacteria that contains the two essential features incorporated in the simulations, that is, the generation of two different cellular states and the coupling between these states through short-ranged chemical signals, allowed the emergence of gene spatial correlation at the population level. As observed in the simulations, these patterns depend on the type of interaction: ferromagnetic or anti-ferromagnetic. These findings support the idea that only two simple rules are sufficient for the emergence of global coherent structures such as those observed in the simulations of the 2D Ising model at phase transitions: two-states and a short-range coupling between them. In this sense, it has been argued that regulatory interactions that lead to a dipole-like behaviour and couple each state

with the surrounding cells are prone to undergo a phase transition that coordinates the behaviour of cell populations [38]. An open question is whether two state metabolic switches that are locally coupled by metabolic signals can give rise to long-range coherence of states such as those seen here. Can, for instance, syntrophic interactions between bistable networks in neighbouring cells give rise to Ising-like long range correlations in cell populations? Would cells exploit these mechanisms to organize processes across different scales?. It remains to be seen whether long-range correlations generated from local coupling, such as those observed in ferromagnetic colonies, are exploited by natural systems to shape the dynamics of a population.

In addition to the simulation of the Ising model during the expansion of a cell population, we also consider a model that accounts for the induction and repression of the genetic circuits. While the CP-IM simulations consider only the change of the state of a cell (or a cell territory) from red to green and vice versa, the model of the induction of reporter genes allowed to study how the binding of the inducers to their promoters (through their respective transcriptional activators) affects the probability that a cell/cell territory is in a particular state. This model, which is based on the model used to study the chemotaxis network in *E. coli* [98], proved to be useful for modeling the behaviour of the SGNs in liquid culture, and allowed us to understand how ferromagnetic and anti-ferromagnetic populations achieve the properties of bi-stability and coupling in well-mixed populations. As observed in the patterns emerging in the colonies, these two properties were found to be necessary and sufficient to generate long- and short-range spatial correlations in spatially arranged populations. Since this model takes into account the local concentration of inducers in the population context where cells are growing and, therefore, can account for the diffusion of the inducers, it could also be useful to model the induction of the SGNs as a reaction-diffusion system during the growth of a cell population.

## 6.2 SGNs that generate Ising-like interactions in bacteria

As in the Ising model, biological systems across different scales show properties consistent with phase transitions, suggesting that they are near critical points that lays on the boundary that separates order from disorder [104, 108, 109]. These critical points could be reached by fine-tuning a control parameter that can be controlled experimentally (such as the temperature in the Ising model), which directly influences the state of a macroscopic variable of the system (the order parameter). The simulations of the Ising model during the growth of a population of cells showed that changing the strength with which cells are coupled allows the transition between ordered and disordered configurations. In ferromagnetic and anti-ferromagnetic colonies, we use the coupling signal to balance the basal expression of the promoters, but we did not explore how a change in the strength of the interaction between cells to influence the emergence of cellular state domains. Thus, it seems relevant to find a biological control parameter equivalent to the temperature of the Ising model (such as the coupling) that can be controlled to explore the emergence of different configurations in a population of cells.

The behaviour of cells carrying the SGNs constructed to emulate Ising-like interactions in bacteria is marked by the higher basal expression of one of the promoters [74, 99]. Depending on the system, this higher basal expression leads to a higher basal production of one of the coupling signals over the other. Although it is possible, at least in theory, to attenuate the effects of this basal expression by, for example, including additional regulatory elements in the genetic network [110] or changing the signaling system used [111], it was easier and less time-consuming to grow cells in a medium supplemented with the inducer of the promoter with lower basal expression to counteract the effects of the other promoter.

A recent study has shown how gene copy number affects the decision-making in a bi-stable gene network, which changes from deterministic and slow at a high copy number ( $10^5$  copies per cell) to fuzzy and fast, with strong fluctuations

and state switching, at a low gene density (10 copies per cell) [112]. In this sense, the behaviour observed in our systems could be in part possible due to the low gene density regimes permitted by the vector backbones used in the SGNs, since both reporter and Ising vectors have a low copy number (Ising vector: pSC101  $\pm 5$  copies per cell, reporter vector: pDestBAC whose copy number can be controlled with arabinose from 1 to  $\pm 40$  copies per cell).

### 6.2.1 Ferromagnetic interactions

In a well-mixed environment, ferromagnetic interactions generate populations of cells that can be in one of three phases: two phases dominated by each of the cellular states, and one phase characterized by a mix of both cellular states. The phase in which a culture of ferromagnetic cells is found depends on the concentration of C6HSL in which they are grown, with high and low concentrations favoring the phases dominated by one of the two cellular states, while an intermediate concentration allows the coexistence of both cellular states. The higher basal production of C12HSL in this system dictates the cellular state that dominates the population in absence of external inducers. It also renders cells insensitive to the external addition of the same inducer, except at very high concentrations, at which HSLs show some degree of toxicity [113] and cross-talk interactions [99]. A population of ferromagnetic cells is characterized by a rapid transition between the single-state phases, where the mixed phase was only achieved at one of the C6HSL concentration tested. These results show that cells in a populations governed by ferromagnetic interactions can change collectively their states. Since in this system the adoption of a particular state stabilize the same states in other cells, this positive loop of induction can spread to the entire population. Specifically, in a well-mixed environment, this means a rapid increase in the concentration of the inducer in the medium, triggering the collective change in the cellular state.

The same behavior observed in a well-mixed population is reflected in solid medium, where the same three phases were also observed in ferromagnetic colonies depending on the concentration of C6HSL in the medium: two phases with

colonies in only one state and one phase with spatial patterns of both states. At low concentrations of external C6HSL, the basal amount of C12HSL produced by cells quickly accumulates in the medium and induces the same state in neighbouring cells, blocking the population in only one state. A high concentration of C6HSL allows that all cells align their states with this inducer, also producing colonies in one state. The spatial patterns observed in ferromagnetic colonies only emerge when the concentration of the external inducer is able to counteract the basal production of C12HSL. At this concentration, the state of each cell within the colony depends mainly on the population context where it grows [19], which is determined by the balance between the coupling signals produced by neighbouring cells.

### 6.2.2 Anti-ferromagnetic interactions

In a well-mixed environment, a population of cells ruled by anti-ferromagnetic interactions grown at low concentrations of external inducers is characterized by a mixed phase with both cellular states. This balance between the cellular states found in a population of anti-ferromagnetic cells can be pushed towards a population dominated by cells in one state or the other depending on the external concentration of C6HSL or C12HSL in which cells are grown. In this system, the higher basal expression of one promoter allows a basal production of C6HSL, which induces the production of C12HSL in other cells, leading to a balance in the amount of coupling signals produced and thus explaining the initial mixed state. This means that a well-mixed population of anti-ferromagnetic cells is characterized by only two phases: a mixed phase with both states at low and intermediate concentrations of the external inducers, and a phase dominated by cells in one state (which depends on the external concentration of C6HSL or C12HSL). However, the transition from the mixed phase to one of the one-state phases is smoother than the transition observed from one phase to another in ferromagnetic cells. Contrary to ferromagnetic cells, anti-ferromagnetic cells respond producing the

opposite inducer they sense, explaining why the transition between phases is less sharp.

Although the same two phases observed in a well-mixed population can also be observed in anti-ferromagnetic colonies (a mixed phase at low and intermediate concentrations of C6HSL, and a phase dominated with cells in one state at high concentrations of this inducer), the spatial patterns that emerge in colonies of anti-ferromagnetic cells grown in absence and at intermediate concentrations of C6HSL are different. While both cellular states are present in absence of external inducers, they are spatially separated, with the center of the colonies dominated by cells in one state and the periphery dominated by cells in the opposite state. Between these two zones emerge a region with a mix of both cellular states. An explanation for this spatial pattern is that the first cells that give rise to the colonies are mostly in the same states due to the higher basal expression of one of the promoters. Although these cells produce basal amounts of C6HSL, it is not enough to induce the opposite state in neighbouring cells, generating a sector in the center of the colony dominated by one cellular state. At a given point during the growth of the colony there would be enough C6HSL in the medium to allow cells to change states regardless of the promoter basal expression, generating a sector with a mix of red and green cellular state domains. As cells continue to synthesize C6HSL, it accumulates to a concentration that trigger a ring of the opposite state in newly born cells in the periphery of the colony. The pattern observed in anti-ferromagnetic colonies in absence of external inducers recapitulates the behaviour observed in a well-mixed population of cells grown under different concentrations of C6HSL. At low concentrations of C6HSL, the probability of finding the *sfGFP* promoter active is approximately two-folds higher than the probability of finding the *mCherry2* promoter active (one state dominating the center of the colony). This difference is maintained until a critical concentration is reached, at which both promoters have the same probability of being active (the mixed region of the colony). Increasing the concentration of C6HSL beyond this critical point slowly increases the probability of finding the *mCherry2* promoter active and at the same time decreases in the probability of finding the *sfGFP*

promoter active (periphery of the colony dominated by cells in one state). On the other hand, growing anti-ferromagnetic cells in solid medium supplemented with an intermediate concentration of C6HSL allows the generation of colonies where the mix of both cellular states, which is only observed in the intermediate region of colonies in absence of external inducer, spans the whole colony. Since at this concentration of C6HSL the probability of finding active the promoters that direct the expression of genes encoding the fluorescent protein is the same, the state of each cell in the colony depends on the population context where it grows. As in ferromagnetic colonies, a high concentration of the external inducer only allows the generation of colonies with cells in only one state due to the alignment of cells with the inducer.

### 6.3 The Moran effect

The evidence that an increase in the concentration of the external coupling signal C6HSL above a critical value leads to the generation of colonies with all cells in the same state, both in ferromagnetic and anti-ferromagnetic systems, show that all cells can align their states due to the effect of a global exogenous force. This exogenous force can be seen as an externally applied magnetic field interacting with each cell in the colony, and thus, the effect of a high concentration of the external C6HSL in the medium can be represented by the second term in the Hamiltonian of the Ising model. In the Ising model, the total energy  $\mathcal{H}$  includes two contributions: the interaction energy between neighbouring spins ( $-J \sum_{\langle ij \rangle} \sigma_i \sigma_j$ ) and the effect of an applied magnetic field ( $-h \sum_i \sigma_i$ ), which acts on each individual spin on the lattice [114]. While the interaction energy favors the alignment between spins, the field energy favors the alignment of all spins with the external magnetic field. Thus, considering a non-zero value for the external magnetic field  $h$ , the total energy of the system is minimized when the spins align their orientations with this external field. In this sense, a high concentration of the external C6HSL increases the concentration of C6HSL that cells sense in the population context where they grow, counterbalancing the effect of local coupling interactions in the

regulation of gene spatial correlations and favoring that each cell align their state with the cellular state induced by this external coupling signal.

The cellular state patterns observed in the colonies grown on different concentrations of an external inducer illustrate the effects of a system dominated by the interaction energy or by the field energy of the Ising model. The interplay between these two energies determines the patterns that emerge in a spatially arranged system. Another example that shows how the Ising model captures the effects of these two energies on the emergence of spatial correlations has been observed in spatial ecology, in which the interplay between exogenous global fields and internal coupling interactions determines the spatial pattern of annual nut production in a pistachio orchard [20]. In this study, long-range correlations in the yield of pistachio trees (that emerge due endogenous forces such as root grafting) becomes homogeneous under global exogenous forces such as weather, a phenomenon widely known as the Moran effect [40]. The use of the Ising model in presence of an external magnetic field to study the emergence of global gene expression correlations in spatially arranged cellular systems could be useful to study the contribution of endogenous interactions that favors the alignments of cellular states compared to the effect of global exogenous forces that tend to synchronize the entire population.

## 6.4 Spatial autocorrelation

Visually, the patches of cellular states that emerge in ferromagnetic colonies are bigger than the ones observed in anti-ferromagnetic colonies. This observation was confirmed with the data obtained from the calculation of the spatial autocorrelation function, which showed that the average distance at which two cells have the same cellular state is greater in ferromagnetic colonies. Specifically, the mean size of the cellular state domains generated in colonies of rod-shaped and



spherical cells is approximately 6.6 to 8.1 times larger when cells exhibit ferromagnetic interactions compared to the domains that emerge in colonies with anti-ferromagnetic interactions. These results show that in bacterial populations, ferromagnetic interactions allow the generation of long-range spatial correlation, while anti-ferromagnetic interactions allow the generation of short-range spatial correlations. Thus, cells can self-organize at the population level using only short-ranged interactions, allowing the generation of different cellular state patterns depending on the type of interaction (ferromagnetic or anti-ferromagnetic) [18, 19, 27].

In densely populated and spatially structured microbial communities such as colonies, mechanical interactions between neighbouring cells are particularly significant, and cell morphology has a strong impact in the spatial patterning of these populations [115]. Specifically, as observed in the cellular states patterns that emerge in ferromagnetic and anti-ferromagnetic colonies, a population of rod-shaped cells is characterized by the emergence of fractal-like jagged patterns due to mechanical interactions generated locally by the polar shape of cells and uniaxial growth. On the other hand, a population of spherical cells, which divide in any direction, is characterized by the generation of smooth boundaries between the cellular state domains, without the self-similar jagged patterns found in colonies of rod-shaped cells [100]. Thus, the fluorescent patterns observed in colonies of rod-shaped cells emerge due to the combination of local coupling generated by the SGNs and local mechanical coupling generated by the shape of the cells. However, the computation of the spatial autocorrelation function showed that the mean size of the cellular state cluster emerging in colonies of rod-shaped cells is similar to the mean size of clusters in spherical cells. These findings suggest that the spatial correlations of gene expression that emerge in a spatially arranged population is independent of the morphology of the cells (rod-shaped or spherical), and only depend on the type of interaction (ferromagnetic or anti-ferromagnetic).

The calculation of the Hamming distance between colonies and simulations (i.e. the number of pixel positions at which the value of those pixels are different) showed that ferromagnetic colonies of spherical cells are more similar to the simulated ferromagnetic populations when the value of the coupling between

cells is around the critical value. At this critical point, the spatial autocorrelation function of the simulated ferromagnetic populations showed to follow a power-law decay of the form  $C(r) \sim r^{-\eta}$ , with a critical exponent  $\eta$  consistent with the value of the Ising model at the critical temperature. On the other hand, the value of the scaling exponent  $\gamma$  calculated for simulated ferromagnetic populations and ferromagnetic colonies showed to be close to the exponent of the cluster size distribution near the critical percolation threshold. At this critical point, the system moves from a regime of only localized short-range connections to one where clusters that span the entire system emerge. Taken together, these results suggest that the ferromagnetic system allows colonies to be positioned close to the point that separates order from disorder, implying that far regions in the colony are correlated. This means that ferromagnetic colonies could be near the critical point of phase transition, with no length scale in the system [95], and suggesting that they are in the Ising universality class.

#### **6.4.1 Behavior of the two-state and coupled systems in the mother machine**

The use of microfluidic devices allowed us to study the dynamics of ferromagnetic and anti-ferromagnetic systems at single cell level. The analysis of the patterns that emerged in colonies of cells carrying these systems gave us an idea of the final result of the interactions between cells, but not how these interactions affect the state of cells in time. In both versions of the mother machine, ferromagnetic cells did not change state during the course of the experiments. Even after using the highest concentration tested in experiments in liquid and solid medium, ferromagnetic cells remained in the same state in which they entered the growth channels (green for the ferromagnetic system with reporter vector 1 and red for reporter vector 2). This synthetic circuit allows cells to not only induce the cellular state in which they are in neighbouring cells, but also reinforce their own state through a positive feedback loop. We argue that cells may need a higher concentration of

the signaling molecule in the medium, or a period of time longer than the time cells remain in the growth channels, to produce a change in their state.

On the other hand, we observed that the ability of anti-ferromagnetic cells to change state depends on the concentration of the coupling signal added to the medium, and this behaviour is independent of the version of the mother machine used. In liquid medium without the external addition of signaling molecules, anti-ferromagnetic cells were unable to change state. Due to the characteristics of the SGNs used (higher basal expression of one of the promoters), one of the cellular states predominates in the population of cells injected into the devices, and thus the growth channels are initially filled with cells in that state. This cellular state is stable and resistant to change in the absence of a certain concentration of signaling molecules, which explains why cells did not change state during the course of the experiments. Growing cells at a high concentration of the coupling signal produced the same result observed in colonies and in liquid cultures: cells aligned their cellular state with the state induced by the coupling signal. However, the use of the microfluidic devices allowed us to observe that cells changed their state only once before aligning their states with the coupling signal. The data obtained from the classic mother machine allowed us to estimate the time that anti-ferromagnetic cells (with the reporter vector 2) take to change state, which is approximately 3 hours after the start of the experiment. One of the most interesting results, however, was obtained when we used liquid medium supplemented with an intermediate concentration of the signaling molecule ( $3.16 \times 10^{-9}$  M C6HSL). As observed in colonies and liquid cultures, an intermediate concentration allows the destabilization of the basal state of cells, which is product of the higher basal expression of one of the promoters. This destabilization of the basal state allowed cells to acquire either of the two possible cellular states. At this concentration, the adoption of a cellular state depends on the local concentration of the signaling molecules that cells can sense in the growth channels, which varies during the course of the experiment as cells adopt states and synthesize coupling molecules. Although the data suggest that a mother cell in a particular state can produce daughter cells in the same and opposite states, and also that mother cells

can change state in time, more data is needed to obtain an approximation of the time anti-ferromagnetic mother cells need to change state or produce daughter cells with different states.

In the experiments with microfluidic devices, the emergence of a "yellow" state was rarely observed, and when it did occur it was very short-lived. This is consistent with the observations made in liquid cultures, where a microscope analysis of ferromagnetic or anti-ferromagnetic populations in the mixed state did not reveal the presence of yellow cells. This suggests that the transition from one state to another is relatively fast. In the mother machine, even when anti-ferromagnetic cells were grown at a high concentration of the inducer (where cells change state only once), the transition between the red and green states was very sharp, without the appearance of cells in a yellow state. As in microfluidic and liquid culture experiments, we also did not observe yellow regions in colonies of ferromagnetic or anti-ferromagnetic cells. In ferromagnetic colonies of rod-shaped and spherical cells, where the cellular state domains are larger, there is a marked and clear boundary between the red and green domains, without the presence of yellow sectors. On the other hand, although some regions of anti-ferromagnetic colonies of rod-shaped cells appear to be yellow, this is mainly due to the small size of the domains, which favors the capture of fluorescence from cells below of them. A yellow sector in the colony would require a large number of cells with a well mixed combination of red and green fluorescent proteins, which is unlikely considering the observations in microfluidic and liquid culture experiments. This can be confirmed by observing the patterns that emerge in anti-ferromagnetic colonies of spherical cells, where, as in ferromagnetic colonies, there is a marked boundary between the red and green states, without the emergence of sectors of the colony in a yellow state. Interestingly, most of the time we observed a yellow state was in filamentous cells. These filamentous cells are formed when cells elongate and replicate their DNA, but do not divide normally, resulting in a multi-nucloid cell. This suggest that in filamentous cells the multiple genomes (and plasmids in our case) are in a different state, resulting in a yellow filamentous cell.

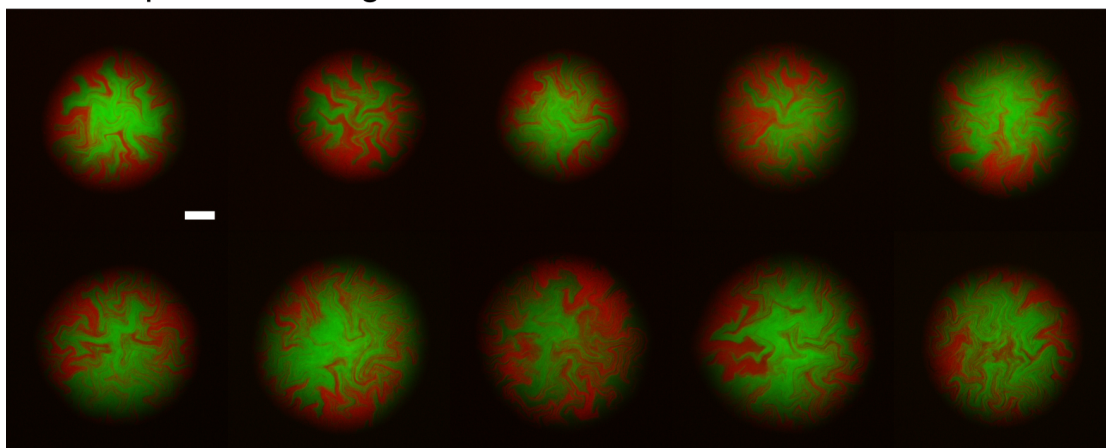
## 6.5 Conclusions

- The use of the CP-IM simulations with Ising-like interactions to study the generations of patterns during the growth of a cell population showed that two cellular states coupled through short-ranged interactions are enough to generate self-organized patterns of gene spatial correlations.
- As suggested by the Ising model, two-states and coupled synthetic gene networks allowed the self-organization of cells and the emergence of patterns of gene spatial correlation at the population level.
- The size of the cellular state domains that emerge in a bacterial colony depends on the type of interaction between cells, with ferromagnetic interactions allowing the generation of larger cellular state patches compared with the ones generated in colonies with anti-ferromagnetic interactions.
- Ferromagnetic colonies of spherical cells are more similar to the simulated ferromagnetic populations around the critical transition.
- The emergence of spatial correlations of gene expression in a spatially arranged cellular system is independent of the cell shape and the mechanical interactions between cells.

# Appendix A

Cellular state patterns generated  
in colonies of cells carrying the  
coupled two-state systems

## Rod-shaped Ferromagnetic 1



## Rod-shaped Ferromagnetic 2

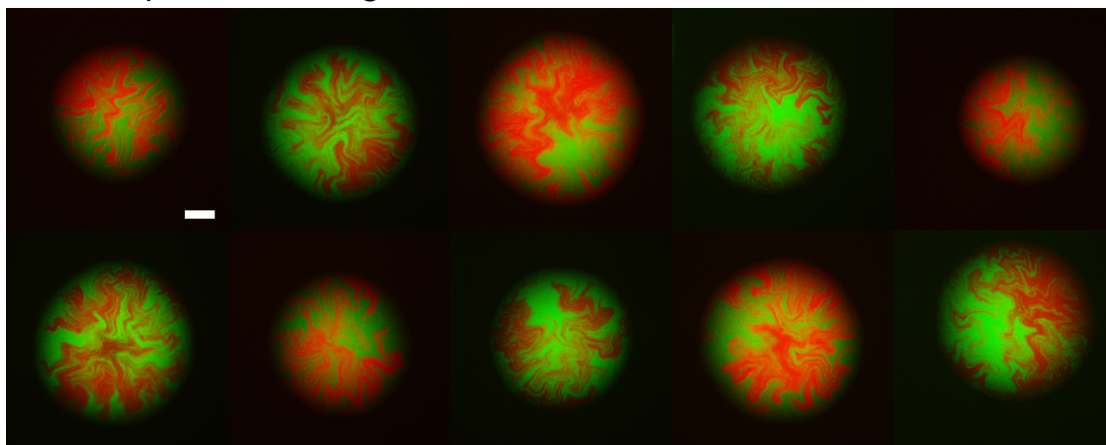
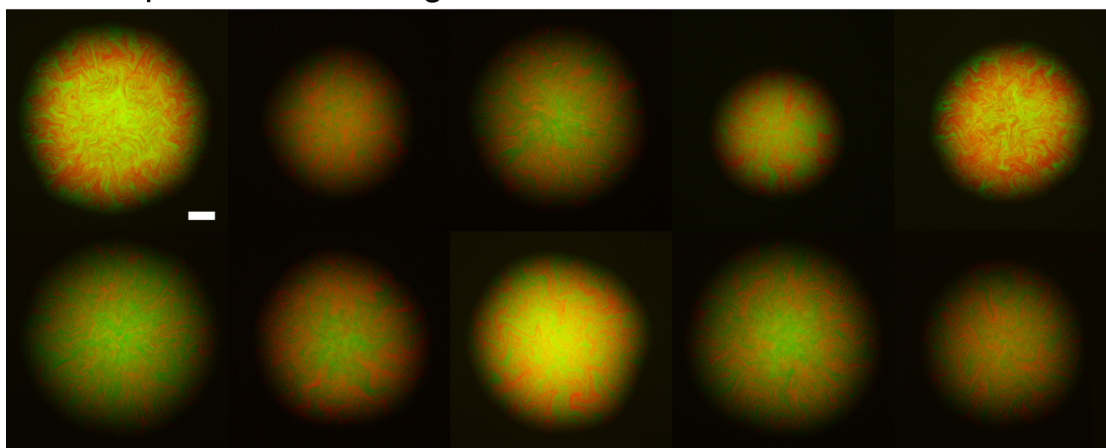


**Figure A.1:** Colonies of rod-shaped *E. coli* cells carrying the ferromagnetic system with reporter vector 1 or 2. Scale bars 100  $\mu\text{m}$ .

## Rod-shaped Anti-ferromagnetic 1



## Rod-shaped Anti-ferromagnetic 2

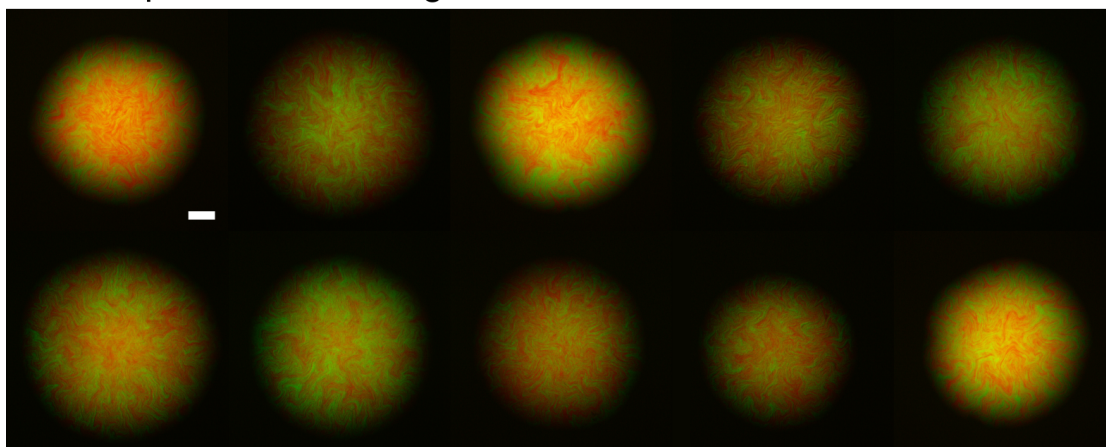
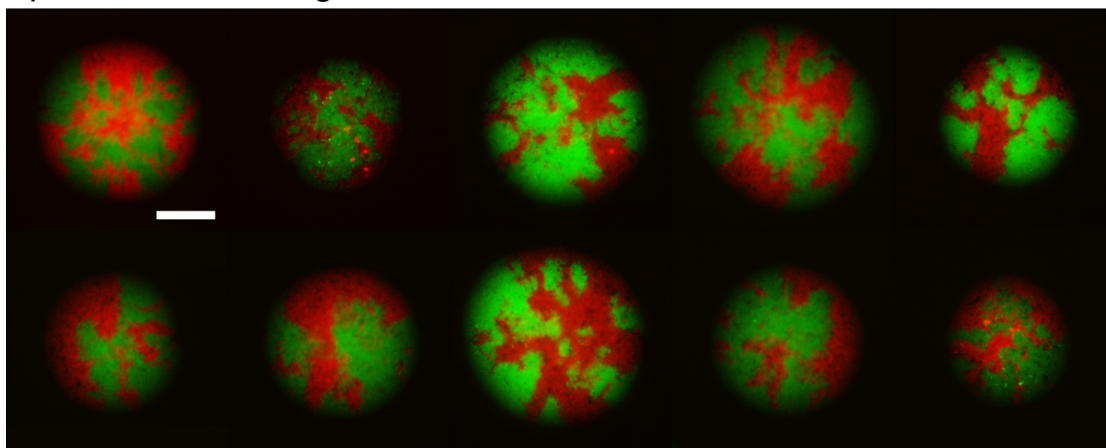


**Figure A.2:** Colonies of rod-shaped *E. coli* cells carrying the anti-ferromagnetic system with reporter vector 1 or 2. Scale bars 100  $\mu\text{m}$ .



## Spherical Ferromagnetic 1



## Spherical Ferromagnetic 2

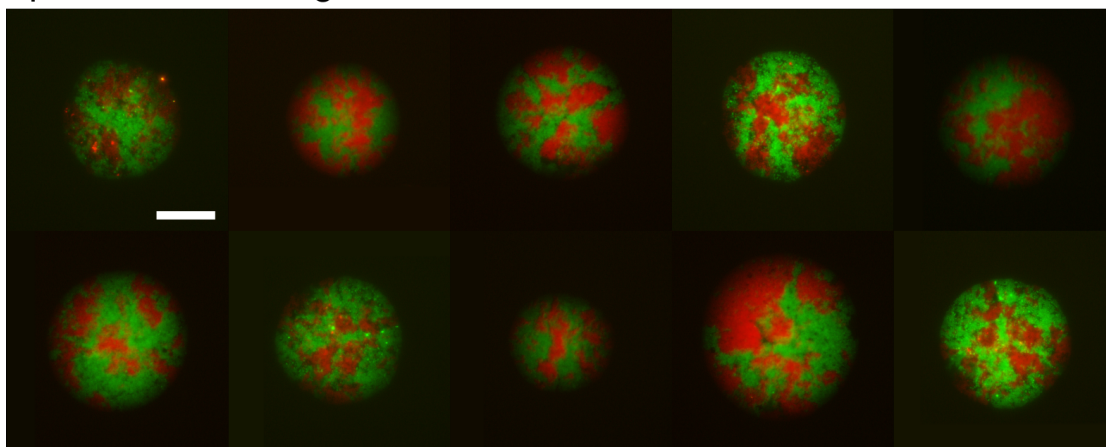
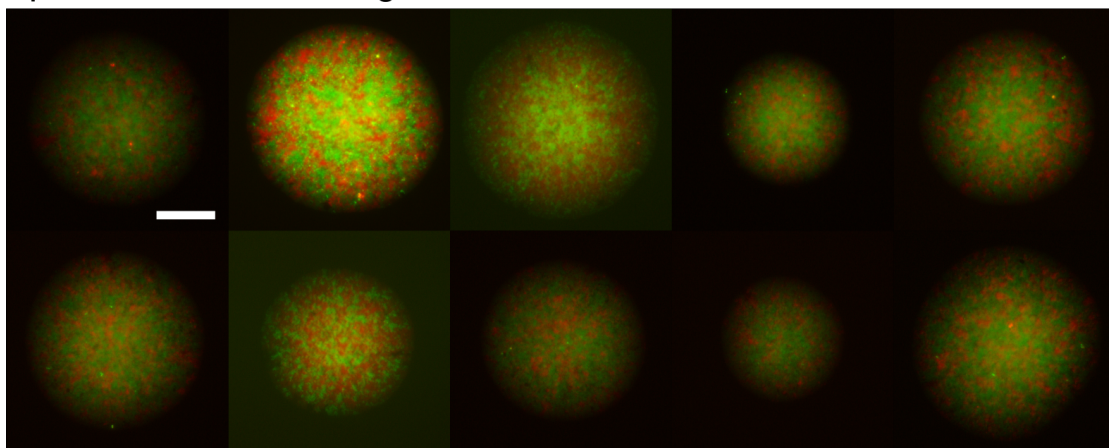


**Figure A.3:** Colonies of spherical *E. coli* cells carrying the ferromagnetic system with reporter vector 1 or 2. Scale bars 100  $\mu\text{m}$ .

## Spherical Anti-ferromagnetic 1



## Spherical Anti-ferromagnetic 2

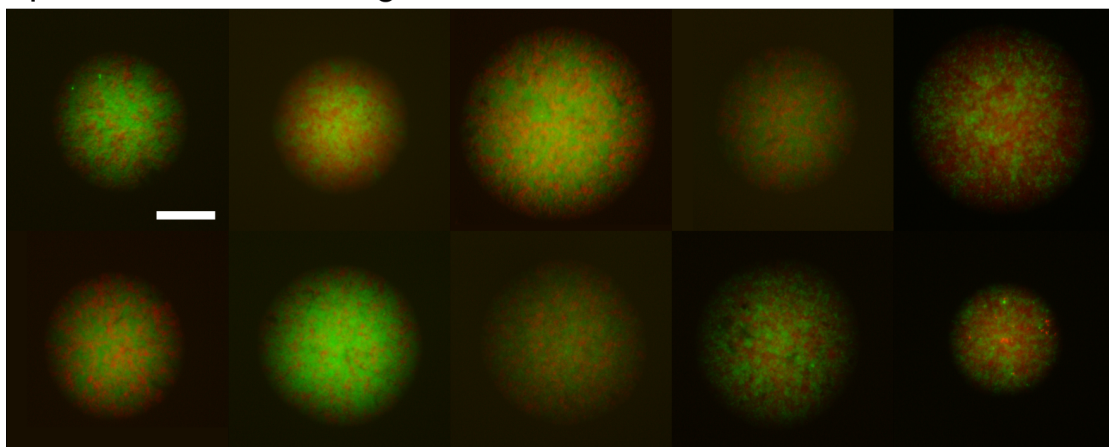


**Figure A.4:** Colonies of spherical *E. coli* cells carrying the anti-ferromagnetic system with reporter vector 1 or 2. Scale bars 100  $\mu\text{m}$ .

# Appendix B

## Python program to calculate the Hamming distance

---

```
1
2 import numpy as np
3 import os
4
5 directory1 = 'C:/Users/KevinSimpson/Desktop/Hamming-Distance/
              Simulation_Ferro_2.00_2.54'
6 directory2 = 'C:/Users/KevinSimpson/Desktop/Hamming-Distance/KJB24_F1
              ',
7
8 HD = []
9 N = 0
10 M = 0
11 for f1 in sorted(os.listdir(directory1)):
12     if f1.endswith(".txt"):
13         N += 1
14 for f2 in sorted(os.listdir(directory2)):
15     if f2.endswith(".txt"):
16         M += 1
17 print(N,M)
18
19 for f1 in sorted(os.listdir(directory1)):
20     if f1.endswith(".txt"):
```

---

```

21         input1 = np.loadtxt(directory1 + "/" + f1, dtype='i',
delimiter='\t')
22         for f2 in sorted(os.listdir(directory2)):
23             if f2.endswith(".txt"):
24                 input2 = np.loadtxt(directory2 + "/" + f2, dtype='i',
delimiter='\t')
25
26                 row1 = len(input1)
27                 col1 = len(input1[0])
28                 row2 = len(input2)
29                 col2 = len(input2[0])
30
31                 HD = 0
32                 #Checks if dimensions of both the matrices are equal
33                 print("Hamming Distance", f1, "x", f2)
34                 if(row1 != row2 or col1 != col2):
35                     print("Matrices are not equal")
36
37                 else:
38                     for i in range(0, row1):
39                         for j in range(0, col1):
40                             if(input1[i][j] != input2[i][j]):
41                                 HD += 1
42                     H.D.append(HD)
43                     #print(H.D)
44
45 Hamming_Distance = np.array(H.D).reshape(N,M)
46 np.savetxt("Simulation_Ferro_2.00_2.54 x KJB24_F1.txt", np.array(
Hamming_Distance), delimiter='\t', fmt='%d')

```

---

# Bibliography

- [1] Marion B. Johnson, Alexander R. March, and Leonardo Morsut. Engineering multicellular systems: Using synthetic biology to control tissue self-organization. *Current Opinion in Biomedical Engineering*, 4:163–173, 2017. ISSN 2468-4511. doi: <https://doi.org/10.1016/j.cobme.2017.10.008>. URL <http://www.sciencedirect.com/science/article/pii/S2468451117300375>.
- [2] Ugo Borello and Alessandra Pierani. Patterning the cerebral cortex: traveling with morphogens. *Current Opinion in Genetics & Development*, 20(4):408–415, 2010. ISSN 0959-437X. doi: <https://doi.org/10.1016/j.gde.2010.05.003>. URL <http://www.sciencedirect.com/science/article/pii/S0959437X10000833>.
- [3] L. Wolpert. Positional information and patterning revisited. *J Theor Biol*, 269(1):359–65, 2011. ISSN 0022-5193. doi: 10.1016/j.jtbi.2010.10.034.
- [4] Anna Kicheva, Michael Cohen, and James Briscoe. Developmental pattern formation: Insights from physics and biology. *Science*, 338(6104):210–212, 2012. doi: 10.1126/science.1225182. URL <https://science.sciencemag.org/content/sci/338/6104/210.full.pdf>.
- [5] J. Casal, G. Struhl, and P. A. Lawrence. Developmental compartments and planar polarity in drosophila. *Curr Biol*, 12(14):1189–98, 2002. ISSN 0960-9822 (Print) 0960-9822. doi: 10.1016/s0960-9822(02)00974-0.
- [6] L. Wolpert. Positional information and the spatial pattern of cellular differentiation. *J Theor Biol*, 25(1):1–47, 1969. ISSN 0022-5193 (Print) 0022-5193 (Linking). doi: 10.1016/s0022-5193(69)80016-0. URL <http://www.ncbi.nlm.nih.gov/pubmed/4390734>.

- [7] A. M. Turing. The chemical basis of morphogenesis. 1953. *Bull Math Biol*, 52(1-2): 153–97; discussion 119–52, 1990. ISSN 0092-8240 (Print) 0092-8240 (Linking). doi: 10.1007/bf02459572. URL <http://www.ncbi.nlm.nih.gov/pubmed/2185858>.
- [8] A. Gierer and H. Meinhardt. A theory of biological pattern formation. *Kybernetik*, 12(1):30–39, 1972. ISSN 1432-0770. doi: 10.1007/BF00289234. URL <https://doi.org/10.1007/BF00289234>.
- [9] S. Kondo and T. Miura. Reaction-diffusion model as a framework for understanding biological pattern formation. *Science*, 329(5999):1616–20, 2010. ISSN 0036-8075. doi: 10.1126/science.1179047.
- [10] A. E. Blanchard and T. Lu. Bacterial social interactions drive the emergence of differential spatial colony structures. *BMC Syst Biol*, 9:59, 2015. ISSN 1752-0509 (Electronic) 1752-0509 (Linking). doi: 10.1186/s12918-015-0188-5. URL <http://www.ncbi.nlm.nih.gov/pubmed/26377684>.
- [11] M. T. Mee, J. J. Collins, G. M. Church, and H. H. Wang. Syntrophic exchange in synthetic microbial communities. *Proc Natl Acad Sci U S A*, 111(20):E2149–56, 2014. ISSN 1091-6490 (Electronic) 0027-8424 (Linking). doi: 10.1073/pnas.1405641111. URL <http://www.ncbi.nlm.nih.gov/pubmed/24778240>.
- [12] J. A. Cole, L. Kohler, J. Hedhli, and Z. Luthey-Schulten. Spatially-resolved metabolic cooperativity within dense bacterial colonies. *BMC Syst Biol*, 9:15, 2015. ISSN 1752-0509 (Electronic) 1752-0509 (Linking). doi: 10.1186/s12918-015-0155-1. URL <http://www.ncbi.nlm.nih.gov/pubmed/25890263>.
- [13] A. Z. Rosenthal, Y. Qi, S. Hormoz, J. Park, S. H. Li, and M. B. Elowitz. Metabolic interactions between dynamic bacterial subpopulations. *Elife*, 7, 2018. ISSN 2050-084X (Electronic) 2050-084X (Linking). doi: 10.7554/eLife.33099. URL <http://www.ncbi.nlm.nih.gov/pubmed/29809139>.
- [14] J. Liu, A. Prindle, J. Humphries, M. Gabalda-Sagarra, M. Asally, D. Y. Lee, S. Ly, J. Garcia-Ojalvo, and G. M. Suel. Metabolic co-dependence gives rise to collective oscillations within biofilms. *Nature*, 523(7562):550–4, 2015. ISSN 1476-4687 (Electronic) 0028-0836 (Linking). doi: 10.1038/nature14660. URL <http://www.ncbi.nlm.nih.gov/pubmed/26200335>.

- [15] A. Prindle, J. Liu, M. Asally, S. Ly, J. Garcia-Ojalvo, and G. M. Suel. Ion channels enable electrical communication in bacterial communities. *Nature*, 527(7576):59–63, 2015. ISSN 1476-4687 (Electronic) 0028-0836 (Linking). doi: 10.1038/nature15709. URL <http://www.ncbi.nlm.nih.gov/pubmed/26503040>.
- [16] J. Liu, R. Martinez-Corral, A. Prindle, D. D. Lee, J. Larkin, M. Gabalda-Sagarra, J. Garcia-Ojalvo, and G. M. Suel. Coupling between distant biofilms and emergence of nutrient time-sharing. *Science*, 356(6338):638–642, 2017. ISSN 1095-9203 (Electronic) 0036-8075 (Linking). doi: 10.1126/science.aah4204. URL <http://www.ncbi.nlm.nih.gov/pubmed/28386026>.
- [17] Edwin H. Wintermute and Pamela A. Silver. Emergent cooperation in microbial metabolism. *Molecular systems biology*, 6:407–407, 2010. ISSN 1744-4292. doi: 10.1038/msb.2010.66. URL <https://pubmed.ncbi.nlm.nih.gov/20823845https://www.ncbi.nlm.nih.gov/pmc/articles/PMC2964121/>.
- [18] Alma Dal Co, Simon van Vliet, and Martin Ackermann. Emergent microscale gradients give rise to metabolic cross-feeding and antibiotic tolerance in clonal bacterial populations. *Philosophical Transactions of the Royal Society B: Biological Sciences*, 374(1786):20190080, 2019. doi: 10.1098/rstb.2019.0080. URL <https://royalsocietypublishing.org/doi/abs/10.1098/rstb.2019.0080>.
- [19] Simon van Vliet, Alma Dal Co, Annina R. Winkler, Stefanie Spriewald, Bärbel Stecher, and Martin Ackermann. Spatially correlated gene expression in bacterial groups: The role of lineage history, spatial gradients, and cell-cell interactions. *Cell Systems*, 6(4):496–507.e6, 2020/05/09 2018.
- [20] A. E. Noble, T. S. Rosenstock, P. H. Brown, J. Machta, and A. Hastings. Spatial patterns of tree yield explained by endogenous forces through a correspondence between the ising model and ecology. *Proc Natl Acad Sci U S A*, 115(8):1825–1830, 2018. ISSN 1091-6490 (Electronic) 0027-8424 (Linking). doi: 10.1073/pnas.1618887115. URL <http://www.ncbi.nlm.nih.gov/pubmed/29437956>.
- [21] D. Bray and T. Duke. Conformational spread: the propagation of allosteric states in large multiprotein complexes. *Annu Rev Biophys Biomol Struct*, 33:53–73, 2004. ISSN 1056-8700 (Print) 1056-8700 (Linking). doi: 10.1146/annurev.biophys.33.110502.132703. URL <http://www.ncbi.nlm.nih.gov/pubmed/15139804>.

- [22] T. A. Duke, N. Le Novere, and D. Bray. Conformational spread in a ring of proteins: a stochastic approach to allostery. *J Mol Biol*, 308(3):541–53, 2001. ISSN 0022-2836 (Print) 0022-2836 (Linking). doi: 10.1006/jmbi.2001.4610. URL <http://www.ncbi.nlm.nih.gov/pubmed/11327786>.
- [23] A. Gierer and H. Meinhardt. A theory of biological pattern formation. *Kybernetik*, 12(1):30–39, 1972.
- [24] James A. Shapiro. The significances of bacterial colony patterns. *BioEssays*, 17(7):597–607, 1995. doi: 10.1002/bies.950170706. URL <https://onlinelibrary.wiley.com/doi/abs/10.1002/bies.950170706>.
- [25] Johannes Jaeger. The gap gene network. *Cellular and Molecular Life Sciences*, 68(2):243–274, 2011.
- [26] Joanne R. Collier, Nicholas A. M. Monk, Philip K. Maini, and Julian H. Lewis. Pattern formation by lateral inhibition with feedback: a mathematical model of delta-notch intercellular signalling. *Journal of Theoretical Biology*, 183(4):429–446, 1996. ISSN 0022-5193. doi: <https://doi.org/10.1006/jtbi.1996.0233>. URL <http://www.sciencedirect.com/science/article/pii/S0022519396902337>.
- [27] Alma Dal Co, Simon van Vliet, Daniel Johannes Kiviet, Susan Schlegel, and Martin Ackermann. Short-range interactions govern the dynamics and functions of microbial communities. *Nature Ecology & Evolution*, 4(3):366–375, 2020. ISSN 2397-334X. doi: 10.1038/s41559-019-1080-2. URL <https://doi.org/10.1038/s41559-019-1080-2>.
- [28] Martin Ackermann. A functional perspective on phenotypic heterogeneity in microorganisms. *Nature Reviews Microbiology*, 13(8):497–508, 2015.
- [29] Peter Q Nguyen, Noémie-Manuelle Dorval Courchesne, Anna Duraj-Thatte, Pichet Praveschotinunt, and Neel S Joshi. Engineered living materials: Prospects and challenges for using biological systems to direct the assembly of smart materials. *Advanced materials (Deerfield Beach, Fla.)*, 30(19):e1704847–e1704847, 05 2018.
- [30] B. P. Teague, P. Guye, and R. Weiss. Synthetic morphogenesis. *Cold Spring Harb Perspect Biol*, 8(9), 2016. ISSN 1943-0264 (Electronic) 1943-0264 (Linking). doi:



- 10.1101/cshperspect.a023929. URL <http://www.ncbi.nlm.nih.gov/pubmed/27270296>.
- [31] Javier Santos-Moreno and Yolanda Schaerli. Using synthetic biology to engineer spatial patterns. *Advanced Biosystems*, 3(4):1800280, 2019. ISSN 2366-7478. doi: 10.1002/adbi.201800280. URL <https://onlinelibrary.wiley.com/doi/abs/10.1002/adbi.201800280>.
- [32] P. Bittihn, M. O. Din, L. S. Tsimring, and J. Hasty. Rational engineering of synthetic microbial systems: from single cells to consortia. *Curr Opin Microbiol*, 45:92–99, 2018. ISSN 1879-0364 (Electronic) 1369-5274 (Linking). doi: 10.1016/j.mib.2018.02.009. URL <http://www.ncbi.nlm.nih.gov/pubmed/29574330>.
- [33] N. S. McCarty and R. Ledesma-Amaro. Synthetic biology tools to engineer microbial communities for biotechnology. *Trends Biotechnol*, 37(2):181–197, 2019. ISSN 1879-3096 (Electronic) 0167-7799 (Linking). doi: 10.1016/j.tibtech.2018.11.002. URL <http://www.ncbi.nlm.nih.gov/pubmed/30497870>.
- [34] E. Ising. Beitrag zur theorie des ferromagnetismus. *Zeitschrift für Physik*, 31(1):253–258, 1925. ISSN 0044-3328. doi: 10.1007/BF02980577. URL <https://doi.org/10.1007/BF02980577>.
- [35] Ricard V. Solé and Brian C. Goodwin. *Signs of life : how complexity pervades biology*. Basic Books, New York, 2000. ISBN 0465019277 9780465019274.
- [36] J. C. Toledo-Roy, A. L. Rivera, and A. Frank. Symmetry, criticality and complex systems. *AIP Conference Proceedings*, 2150(1):020014, 2019. doi: 10.1063/1.5124586. URL <https://aip.scitation.org/doi/abs/10.1063/1.5124586>.
- [37] H. Wioland, F. G. Woodhouse, J. Dunkel, and R. E. Goldstein. Ferromagnetic and antiferromagnetic order in bacterial vortex lattices. *Nat Phys*, 12:341–345, 2016. ISSN 1745-2473 (Print) 1745-2473 (Linking). doi: 10.1038/nphys3607. URL <http://www.ncbi.nlm.nih.gov/pubmed/27213004>.
- [38] M. Weber and J. Buceta. The cellular ising model: a framework for phase transitions in multicellular environments. *J R Soc Interface*, 13(119), 2016. ISSN 1742-5662 (Electronic) 1742-5662 (Linking). doi: 10.1098/rsif.2015.1092. URL <http://www.ncbi.nlm.nih.gov/pubmed/27307510>.

- [39] Yanshu Wang, Tudor Badea, and Jeremy Nathans. Order from disorder: Self-organization in mammalian hair patterning. *Proceedings of the National Academy of Sciences*, 103(52):19800–19805, 2006. doi: 10.1073/pnas.0609712104. URL <https://www.pnas.org/content/pnas/103/52/19800.full.pdf>.
- [40] PAP Moran. The statistical analysis of the canadian lynx cycle. 1. structure and prediction. *Australian Journal of Zoology*, 1(2):163–173, 1953. doi: <https://doi.org/10.1071/ZO9530163>. URL <https://www.publish.csiro.au/paper/Z09530163>.
- [41] A. E. Noble, J. Machta, and A. Hastings. Emergent long-range synchronization of oscillating ecological populations without external forcing described by ising universality. *Nat Commun*, 6:6664, 2015. ISSN 2041-1723 (Electronic) 2041-1723 (Linking). doi: 10.1038/ncomms7664. URL <http://www.ncbi.nlm.nih.gov/pubmed/25851364>.
- [42] N. S. Scholes and M. Isalan. A three-step framework for programming pattern formation. *Curr Opin Chem Biol*, 40:1–7, 2017. ISSN 1879-0402 (Electronic) 1367-5931 (Linking). doi: 10.1016/j.cbpa.2017.04.008. URL <http://www.ncbi.nlm.nih.gov/pubmed/28463802>.
- [43] Jamie Davies. Using synthetic biology to explore principles of development. *Development*, 144(7):1146–1158, 2017. doi: 10.1242/dev.144196. URL <https://dev.biologists.org/content/develop/144/7/1146.full.pdf>.
- [44] N. Luo, S. Wang, and L. You. Synthetic pattern formation. *Biochemistry*, 58(11):1478–1483, 2019. ISSN 1520-4995 (Electronic) 0006-2960 (Linking). doi: 10.1021/acs.biochem.8b01242. URL <http://www.ncbi.nlm.nih.gov/pubmed/30666867>.
- [45] T. S. Gardner, C. R. Cantor, and J. J. Collins. Construction of a genetic toggle switch in escherichia coli. *Nature*, 403(6767):339–42, 2000. ISSN 0028-0836 (Print) 0028-0836 (Linking). doi: 10.1038/35002131. URL <http://www.ncbi.nlm.nih.gov/pubmed/10659857>.
- [46] M. B. Elowitz and S. Leibler. A synthetic oscillatory network of transcriptional regulators. *Nature*, 403(6767):335–8, 1 2000. ISSN 0028-0836. doi: 10.1038/35002125.

- [47] S. Mukherji and A. van Oudenaarden. Synthetic biology: understanding biological design from synthetic circuits. *Nat Rev Genet*, 10(12):859–71, 2009. ISSN 1471-0064 (Electronic) 1471-0056 (Linking). doi: 10.1038/nrg2697. URL <http://www.ncbi.nlm.nih.gov/pubmed/19898500>.
- [48] A. S. Khalil and J. J. Collins. Synthetic biology: applications come of age. *Nat Rev Genet*, 11(5):367–79, 2010. ISSN 1471-0064 (Electronic) 1471-0056 (Linking). doi: 10.1038/nrg2775. URL <http://www.ncbi.nlm.nih.gov/pubmed/20395970>.
- [49] P. E. Purnick and R. Weiss. The second wave of synthetic biology: from modules to systems. *Nat Rev Mol Cell Biol*, 10(6):410–22, 2009. ISSN 1471-0080 (Electronic) 1471-0072 (Linking). doi: 10.1038/nrm2698. URL <http://www.ncbi.nlm.nih.gov/pubmed/19461664>.
- [50] Alec A. K. Nielsen, Bryan S. Der, Jonghyeon Shin, Prashant Vaidyanathan, Vanya Paralanov, Elizabeth A. Strychalski, David Ross, Douglas Densmore, and Christopher A. Voigt. Genetic circuit design automation. *Science*, 352(6281):aac7341, 4 2016. ISSN 1095-9203. doi: 10.1126/science.aac7341.
- [51] Nagarajan Nandagopal and Michael B. Elowitz. Synthetic biology: integrated gene circuits. *Science (New York, N.Y.)*, 333(6047):1244–1248, 2011. ISSN 1095-9203 0036-8075. doi: 10.1126/science.1207084. URL <https://pubmed.ncbi.nlm.nih.gov/21885772https://www.ncbi.nlm.nih.gov/pmc/articles/PMC4117316/>.
- [52] Mark Isalan, Caroline Lemerle, and Luis Serrano. Engineering gene networks to emulate drosophila embryonic pattern formation. *PLOS Biology*, 3(3), 02 2005. doi: 10.1371/journal.pbio.0030064. URL <https://doi.org/10.1371/journal.pbio.0030064>.
- [53] Yolanda Schaerli, Andreea Munteanu, Magüi Gili, James Cotterell, James Sharpe, and Mark Isalan. A unified design space of synthetic stripe-forming networks. *Nature Communications*, 5(1):4905, 2014.
- [54] Frederick K Balagaddé, Hao Song, Jun Ozaki, Cynthia H Collins, Matthew Barnet, Frances H Arnold, Stephen R Quake, and Lingchong You. A synthetic escherichia coli predator–prey ecosystem. *Molecular Systems Biology*, 4(1):187, 2008. doi: 10.1038/msb.2008.24. URL <https://www.embopress.org/doi/abs/10.1038/msb.2008.24>.

- [55] K. Axelrod, A. Sanchez, and J. Gore. Phenotypic states become increasingly sensitive to perturbations near a bifurcation in a synthetic gene network. *Elife*, 4, 2015. ISSN 2050-084X (Electronic) 2050-084X (Linking). doi: 10.7554/eLife.07935. URL <http://www.ncbi.nlm.nih.gov/pubmed/26302311>.
- [56] David Karig, K. Michael Martini, Ting Lu, Nicholas A. DeLateur, Nigel Goldenfeld, and Ron Weiss. Stochastic turing patterns in a synthetic bacterial population. *Proceedings of the National Academy of Sciences*, 115(26):6572–6577, 2018. ISSN 0027-8424. doi: 10.1073/pnas.1720770115. URL <https://www.pnas.org/content/115/26/6572>.
- [57] S. Basu, Y. Gerchman, C. H. Collins, F. H. Arnold, and R. Weiss. A synthetic multicellular system for programmed pattern formation. *Nature*, 434(7037):1130–4, 2005. ISSN 1476-4687 (Electronic) 0028-0836 (Linking). doi: 10.1038/nature03461. URL <http://www.ncbi.nlm.nih.gov/pubmed/15858574>.
- [58] Mitsuhiro Matsuda, Makito Koga, Knut Woltjen, Eisuke Nishida, and Miki Ebisuya. Synthetic lateral inhibition governs cell-type bifurcation with robust ratios. *Nature Communications*, 6(1):6195, 2015.
- [59] Satoshi Toda, Lucas R. Blauch, Sindy K. Y. Tang, Leonardo Morsut, and Wendell A. Lim. Programming self-organizing multicellular structures with synthetic cell-cell signaling. *Science*, 361(6398):156–162, 2018. doi: 10.1126/science.aat0271. URL <https://science.sciencemag.org/content/361/6398/156>.
- [60] M. R. Ebrahimkhani and M. Ebisuya. Synthetic developmental biology: build and control multicellular systems. *Curr Opin Chem Biol*, 52:9–15, 2019. ISSN 1879-0402 (Electronic) 1367-5931 (Linking). doi: 10.1016/j.cbpa.2019.04.006. URL <http://www.ncbi.nlm.nih.gov/pubmed/31102790>.
- [61] J. A. Shapiro. Thinking about bacterial populations as multicellular organisms. *Annu Rev Microbiol*, 52:81–104, 1998. ISSN 0066-4227 (Print) 0066-4227 (Linking). doi: 10.1146/annurev.micro.52.1.81. URL <http://www.ncbi.nlm.nih.gov/pubmed/9891794>.
- [62] O. A. Igoshin, D. Kaiser, and G. Oster. Breaking symmetry in myxobacteria. *Curr Biol*, 14(12):R459–62, 2004. ISSN 0960-9822 (Print) 0960-9822 (Linking).

- doi: 10.1016/j.cub.2004.06.007. URL <http://www.ncbi.nlm.nih.gov/pubmed/15203014>.
- [63] A. L. McLoon, I. Kolodkin-Gal, S. M. Rubinstein, R. Kolter, and R. Losick. Spatial regulation of histidine kinases governing biofilm formation in *Bacillus subtilis*. *J Bacteriol*, 193(3):679–85, 2011. ISSN 1098-5530 (Electronic) 0021-9193 (Linking). doi: 10.1128/JB.01186-10. URL <http://www.ncbi.nlm.nih.gov/pubmed/21097618>.
- [64] S. S. Branda, J. E. Gonzalez-Pastor, S. Ben-Yehuda, R. Losick, and R. Kolter. Fruiting body formation by *Bacillus subtilis*. *Proc Natl Acad Sci U S A*, 98(20):11621–6, 2001. ISSN 0027-8424 (Print) 0027-8424 (Linking). doi: 10.1073/pnas.191384198. URL <http://www.ncbi.nlm.nih.gov/pubmed/11572999>.
- [65] E. Ben-Jacob and H. Levine. Self-engineering capabilities of bacteria. *J R Soc Interface*, 3(6):197–214, 2006. ISSN 1742-5689 (Print) 1742-5662 (Linking). doi: 10.1098/rsif.2005.0089. URL <http://www.ncbi.nlm.nih.gov/pubmed/16849231>.
- [66] N. A. Lyons and R. Kolter. On the evolution of bacterial multicellularity. *Curr Opin Microbiol*, 24:21–8, 2015. ISSN 1879-0364 (Electronic) 1369-5274 (Linking). doi: 10.1016/j.mib.2014.12.007. URL <http://www.ncbi.nlm.nih.gov/pubmed/25597443>.
- [67] J. Pascalie, M. Potier, T. Kowaliw, J. L. Giavitto, O. Michel, A. Spicher, and R. Doursat. Developmental design of synthetic bacterial architectures by morphogenetic engineering. *ACS Synth Biol*, 5(8):842–61, 2016. ISSN 2161-5063 (Electronic) 2161-5063 (Linking). doi: 10.1021/acssynbio.5b00246. URL <http://www.ncbi.nlm.nih.gov/pubmed/27244532>.
- [68] Martyn Amos. Population-based microbial computing: a third wave of synthetic biology? *International Journal of General Systems*, 43(7):770–782, 2014. ISSN 0308-1079. doi: 10.1080/03081079.2014.921001. URL <http://dx.doi.org/10.1080/03081079.2014.921001>.
- [69] Ricard V. Solé and Javier Macia. Expanding the landscape of biological computation with synthetic multicellular consortia. *Natural Computing*, 12(4):485–497, 2013. ISSN 1572-9796. doi: 10.1007/s11047-013-9380-y. URL <https://doi.org/10.1007/s11047-013-9380-y>.

- [70] K. Zhou, K. Qiao, S. Edgar, and G. Stephanopoulos. Distributing a metabolic pathway among a microbial consortium enhances production of natural products. *Nat Biotechnol*, 33(4):377–83, 2015. ISSN 1546-1696 (Electronic) 1087-0156 (Linking). doi: 10.1038/nbt.3095. URL <http://www.ncbi.nlm.nih.gov/pubmed/25558867>.
- [71] S. Payne, B. Li, Y. Cao, D. Schaeffer, M. D. Ryser, and L. You. Temporal control of self-organized pattern formation without morphogen gradients in bacteria. *Mol Syst Biol*, 9:697, 2013. ISSN 1744-4292 (Electronic) 1744-4292 (Linking). doi: 10.1038/msb.2013.55. URL <http://www.ncbi.nlm.nih.gov/pubmed/24104480>.
- [72] C. Liu, X. Fu, L. Liu, X. Ren, C. K. Chau, S. Li, L. Xiang, H. Zeng, G. Chen, L. H. Tang, P. Lenz, X. Cui, W. Huang, T. Hwa, and J. D. Huang. Sequential establishment of stripe patterns in an expanding cell population. *Science*, 334(6053):238–41, 2011. ISSN 1095-9203 (Electronic) 0036-8075 (Linking). doi: 10.1126/science.1209042. URL <http://www.ncbi.nlm.nih.gov/pubmed/21998392>.
- [73] K. Brenner, L. You, and F. H. Arnold. Engineering microbial consortia: a new frontier in synthetic biology. *Trends Biotechnol*, 26(9):483–9, 2008. ISSN 0167-7799 (Print) 0167-7799 (Linking). doi: 10.1016/j.tibtech.2008.05.004. URL <http://www.ncbi.nlm.nih.gov/pubmed/18675483>.
- [74] P. K. Grant, N. Dalchau, J. R. Brown, F. Federici, T. J. Rudge, B. Yordanov, O. Patange, A. Phillips, and J. Haseloff. Orthogonal intercellular signaling for programmed spatial behavior. *Mol Syst Biol*, 12(1):849, 2016. ISSN 1744-4292 (Electronic) 1744-4292 (Linking). doi: 10.15252/msb.20156590. URL <http://www.ncbi.nlm.nih.gov/pubmed/26814193>.
- [75] S. Regot, J. Macia, N. Conde, K. Furukawa, J. Kjellen, T. Peeters, S. Hohmann, E. de Nadal, F. Posas, and R. Sole. Distributed biological computation with multicellular engineered networks. *Nature*, 469(7329):207–11, 2011. ISSN 1476-4687 (Electronic) 0028-0836 (Linking). doi: 10.1038/nature09679. URL <http://www.ncbi.nlm.nih.gov/pubmed/21150900>.
- [76] H. Song, M. Z. Ding, X. Q. Jia, Q. Ma, and Y. J. Yuan. Synthetic microbial consortia: from systematic analysis to construction and applications. *Chem Soc*

- Rev*, 43(20):6954–81, 2014. ISSN 1460-4744 (Electronic) 0306-0012 (Linking). doi: 10.1039/c4cs00114a. URL <http://www.ncbi.nlm.nih.gov/pubmed/25017039>.
- [77] R. J. Case, M. Labbate, and S. Kjelleberg. Ahl-driven quorum-sensing circuits: their frequency and function among the proteobacteria. *ISME J*, 2(4):345–9, 2008. ISSN 1751-7362 (Print) 1751-7362 (Linking). doi: 10.1038/ismej.2008.13. URL <http://www.ncbi.nlm.nih.gov/pubmed/18273067>.
- [78] Fuqing Wu, David J. Menn, and Xiao Wang. Quorum-sensing crosstalk-driven synthetic circuits: from unimodality to trimodality. *Chemistry & biology*, 21(12):1629–1638, 2014. ISSN 1879-1301 1074-5521. doi: 10.1016/j.chembiol.2014.10.008. URL <https://pubmed.ncbi.nlm.nih.gov/25455858><https://www.ncbi.nlm.nih.gov/pmc/articles/PMC4272683/>.
- [79] A. M. Stevens and E. P. Greenberg. Quorum sensing in vibrio fischeri: essential elements for activation of the luminescence genes. *J Bacteriol*, 179(2):557–62, 1997. ISSN 0021-9193 (Print) 0021-9193 (Linking). doi: 10.1128/jb.179.2.557-562.1997. URL <http://www.ncbi.nlm.nih.gov/pubmed/8990313>.
- [80] M. Schuster, M. L. Urbanowski, and E. P. Greenberg. Promoter specificity in pseudomonas aeruginosa quorum sensing revealed by dna binding of purified lasr. *Proc Natl Acad Sci U S A*, 101(45), 2004. ISSN 0027-8424 (Print) 0027-8424 (Linking). doi: 10.1073/pnas.0407229101. URL <http://www.ncbi.nlm.nih.gov/pubmed/15505212>.
- [81] Simon van Vliet and Martin Ackermann. Bacterial ventures into multicellularity: Collectivism through individuality. *PLOS Biology*, 13(6):1–5, 06 2015. doi: 10.1371/journal.pbio.1002162. URL <https://doi.org/10.1371/journal.pbio.1002162>.
- [82] Wiebke Mohr, Tomas Vagner, Marcel M. M. Kuypers, Martin Ackermann, and Julie LaRoche. Resolution of conflicting signals at the single-cell level in the regulation of cyanobacterial photosynthesis and nitrogen fixation. *PLOS ONE*, 8(6):1–7, 06 2013. doi: 10.1371/journal.pone.0066060. URL <https://doi.org/10.1371/journal.pone.0066060>.

- [83] K. J. Begg and W. D. Donachie. Division planes alternate in spherical cells of *Escherichia coli*. *J Bacteriol*, 180(9):2564–7, 1998. ISSN 0021-9193 (Print) 0021-9193 (Linking). URL <http://www.ncbi.nlm.nih.gov/pubmed/9573213>.
- [84] C. Engler, R. Kandzia, and S. Marillonnet. A one pot, one step, precision cloning method with high throughput capability. *PLoS One*, 3(11):e3647, 2008. ISSN 1932-6203 (Electronic) 1932-6203 (Linking). doi: 10.1371/journal.pone.0003647. URL <http://www.ncbi.nlm.nih.gov/pubmed/18985154>.
- [85] D. G. Gibson, L. Young, R. Y. Chuang, J. C. Venter, 3rd Hutchison, C. A., and H. O. Smith. Enzymatic assembly of dna molecules up to several hundred kilobases. *Nat Methods*, 6(5):343–5, 2009. ISSN 1548-7105 (Electronic) 1548-7091 (Linking). doi: 10.1038/nmeth.1318. URL <http://www.ncbi.nlm.nih.gov/pubmed/19363495>.
- [86] S. V. Iverson, T. L. Haddock, J. Beal, and D. M. Densmore. Cidar moclo: Improved moclo assembly standard and new *E. coli* part library enable rapid combinatorial design for synthetic and traditional biology. *ACS Synth Biol*, 5(1):99–103, 2016. ISSN 2161-5063 (Electronic) 2161-5063 (Linking). doi: 10.1021/acssynbio.5b00124. URL <http://www.ncbi.nlm.nih.gov/pubmed/26479688>.
- [87] Yi Shen, Yingche Chen, Jiahui Wu, Nathan C. Shaner, and Robert E. Campbell. Engineering of mcherry variants with long stokes shift, red-shifted fluorescence, and low cytotoxicity. *PloS one*, 12(2):e0171257–e0171257, 2017. ISSN 1932-6203. doi: 10.1371/journal.pone.0171257. URL <https://pubmed.ncbi.nlm.nih.gov/28241009><https://www.ncbi.nlm.nih.gov/pmc/articles/PMC5328254/>.
- [88] J. Schindelin, I. Arganda-Carreras, E. Frise, V. Kaynig, M. Longair, T. Pietzsch, S. Preibisch, C. Rueden, S. Saalfeld, B. Schmid, J. Y. Tinevez, D. J. White, V. Hartenstein, K. Eliceiri, P. Tomancak, and A. Cardona. Fiji: an open-source platform for biological-image analysis. *Nat Methods*, 9(7):676–82, 2012. ISSN 1548-7105 (Electronic) 1548-7091 (Linking). doi: 10.1038/nmeth.2019. URL <http://www.ncbi.nlm.nih.gov/pubmed/22743772>.
- [89] C. A. Schneider, W. S. Rasband, and K. W. Eliceiri. Nih image to imagej: 25 years of image analysis. *Nat Methods*, 9(7):671–5, 2012. ISSN 1548-7105 (Electronic)



- 1548-7091 (Linking). doi: 10.1038/nmeth.2089. URL <http://www.ncbi.nlm.nih.gov/pubmed/22930834>.
- [90] Vivien Walter. *Lipid membrane interaction with self-assembling cell-penetrating peptides*. PhD thesis, Univ. Strasbourg, 09 2017.
- [91] Dong Qin, Younan Xia, and George M. Whitesides. Soft lithography for micro- and nanoscale patterning. *Nature Protocols*, 5(3):491–502, 2010. ISSN 1750-2799. doi: 10.1038/nprot.2009.234. URL <https://doi.org/10.1038/nprot.2009.234>.
- [92] Nicholas Metropolis, Arianna W. Rosenbluth, Marshall N. Rosenbluth, Augusta H. Teller, and Edward Teller. Equation of state calculations by fast computing machines. *The Journal of Chemical Physics*, 21(6):1087–1092, 1953. doi: 10.1063/1.1699114. URL <https://aip.scitation.org/doi/abs/10.1063/1.1699114>.
- [93] T. E. Harris. Contact interactions on a lattice. *Ann. Probab.*, 2(6):969–988, 1974. ISSN 0091-1798. doi: 10.1214/aop/1176996493. URL <https://projecteuclid.org:443/euclid.aop/1176996493>.
- [94] David P. Landau and Kurt Binder. *A Guide to Monte Carlo Simulations in Statistical Physics*. Cambridge University Press, Cambridge, 4 edition, 2014. ISBN 9781107074026. doi: DOI:10.1017/CBO9781139696463. URL <https://www.cambridge.org/core/books/guide-to-monte-carlo-simulations-in-statistical-physics/2522172663AF92943C625056C14F6055>.
- [95] Eduardo Ibarra-García-Padilla, Carlos Gerardo Malanche-Flores, and Freddy Jackson Poveda-Cuevas. The hobbyhorse of magnetic systems: the ising model. *European Journal of Physics*, 37(6):065103, 2016. ISSN 0143-0807 1361-6404. doi: 10.1088/0143-0807/37/6/065103. URL <http://dx.doi.org/10.1088/0143-0807/37/6/065103>.
- [96] N. Goldenfeld. *Lectures On Phase Transitions And The Renormalization Group*. CRC Press, 2018.
- [97] T. J. Rudge, J. R. Brown, F. Federici, N. Dalchau, A. Phillips, J. W. Ajioka, and J. Haseloff. Characterization of intrinsic properties of promoters. *ACS Synth Biol*, 5(1):89–98, 2016. ISSN 2161-5063 (Electronic) 2161-5063 (Linking). doi: 10.1021/acssynbio.5b00116. URL <http://www.ncbi.nlm.nih.gov/pubmed/26436725>.

- [98] Juan E. Keymer, Robert G. Endres, Monica Skoge, Yigal Meir, and Ned S. Wingreen. Chemosensing in *Escherichia coli*: Two regimes of two-state receptors. *Proceedings of the National Academy of Sciences of the United States of America*, 103(6):1786–1791, 2006. doi: 10.1073/pnas.0507438103. URL <https://www.pnas.org/content/pnas/103/6/1786.full.pdf>.
- [99] N. Kylilis, Z. A. Tuza, G. B. Stan, and K. M. Polizzi. Tools for engineering coordinated system behaviour in synthetic microbial consortia. *Nat Commun*, 9(1):2677, 2018. ISSN 2041-1723 (Electronic) 2041-1723 (Linking). doi: 10.1038/s41467-018-05046-2. URL <http://www.ncbi.nlm.nih.gov/pubmed/29992956>.
- [100] T. J. Rudge, F. Federici, P. J. Steiner, A. Kan, and J. Haseloff. Cell polarity-driven instability generates self-organized, fractal patterning of cell layers. *ACS Synth Biol*, 2(12):705–14, 2013. ISSN 2161-5063 (Electronic) 2161-5063 (Linking). doi: 10.1021/sb400030p. URL <http://www.ncbi.nlm.nih.gov/pubmed/23688051>.
- [101] I. N. Nunez, T. F. Matute, I. D. Del Valle, A. Kan, A. Choksi, D. Endy, J. Haseloff, T. J. Rudge, and F. Federici. Artificial symmetry-breaking for morphogenetic engineering bacterial colonies. *ACS Synth Biol*, 6(2):256–265, 2017. ISSN 2161-5063 (Electronic) 2161-5063 (Linking). doi: 10.1021/acssynbio.6b00149. URL <http://www.ncbi.nlm.nih.gov/pubmed/27794593>.
- [102] Mohamed N. Nounou and Bhavik R. Bakshi. Chapter 5 - multiscale methods for denoising and compression. In Beata Walczak, editor, *Wavelets in Chemistry*, volume 22 of *Data Handling in Science and Technology*, pages 119 – 150. Elsevier, 2000. doi: [https://doi.org/10.1016/S0922-3487\(00\)80030-1](https://doi.org/10.1016/S0922-3487(00)80030-1). URL <http://www.sciencedirect.com/science/article/pii/S0922348700800301>.
- [103] Dietrich Stauffer and Amnon Aharony. *Introduction to percolation theory*. Taylor & Francis, London ; Bristol, PA, rev., 2nd edition, 1994. ISBN 0748400273. 94200274 Dietrich Stauffer and Amnon Aharony. ill. ; 24 cm. Includes bibliographical references and index.
- [104] J. W. Larkin, X. Zhai, K. Kikuchi, S. E. Redford, A. Prindle, J. Liu, S. Greenfield, A. M. Walczak, J. Garcia-Ojalvo, A. Mugler, and G. M. Süel. Signal percolation within a bacterial community. *Cell Syst*, 7(2):137–145.e3, 2018. ISSN 2405-4712 (Print) 2405-4712. doi: 10.1016/j.cels.2018.06.005.

- [105] Ping Wang, Lydia Robert, James Pelletier, Wei Lien Dang, Francois Taddei, Andrew Wright, and Suckjoon Jun. Robust growth of *escherichia coli*. *Current biology : CB*, 20(12):1099–1103, 2010. ISSN 1879-0445 0960-9822. doi: 10.1016/j.cub.2010.04.045. URL <https://pubmed.ncbi.nlm.nih.gov/20537537><https://www.ncbi.nlm.nih.gov/pmc/articles/PMC2902570/>.
- [106] Vahini Reddy Nareddy, Jonathan Machta, Karen C. Abbott, Shadisadat Esmaeili, and Alan Hastings. Dynamical ising model of spatially coupled ecological oscillators. *Journal of The Royal Society Interface*, 17(171):20200571, 2020. doi: doi:10.1098/rsif.2020.0571. URL <https://royalsocietypublishing.org/doi/abs/10.1098/rsif.2020.0571>.
- [107] Paul K. Grant, Gregory Szep, Om Patange, Jacob Halatek, Valerie Coppard, Attila Csikász-Nagy, Jim Haseloff, James C. W. Locke, Neil Dalchau, and Andrew Phillips. Interpretation of morphogen gradients by a synthetic bistable circuit. *Nature Communications*, 11(1):5545, 2020. ISSN 2041-1723. doi: 10.1038/s41467-020-19098-w. URL <https://doi.org/10.1038/s41467-020-19098-w>.
- [108] Thierry Mora and William Bialek. Are biological systems poised at criticality? *Journal of Statistical Physics*, 144(2):268–302, 2011. ISSN 1572-9613. doi: 10.1007/s10955-011-0229-4. URL <https://doi.org/10.1007/s10955-011-0229-4>.
- [109] Blai Vidiella, Antoni Guillamon, Josep Sardanyés, Victor Maull, Nuria Conde-Pueyo, and Ricard Solé. Engineering self-organized criticality in living cells. *bioRxiv*, page 2020.11.16.385385, 2020. doi: 10.1101/2020.11.16.385385. URL <http://biorxiv.org/content/early/2020/11/17/2020.11.16.385385.abstract>.
- [110] Alexander A Green, Pamela A Silver, James J Collins, and Peng Yin. Toehold switches: De-novo-designed regulators of gene expression. *Cell*, 159(4):925–939, 2014. ISSN 0092-8674. doi: <https://doi.org/10.1016/j.cell.2014.10.002>. URL <http://www.sciencedirect.com/science/article/pii/S0092867414012896>.
- [111] N. Marchand and C. H. Collins. Peptide-based communication system enables *escherichia coli* to *bacillus megaterium* interspecies signaling. *Biotechnol Bioeng*, 110(11):3003–12, 2013. ISSN 0006-3592. doi: 10.1002/bit.24975.

- [112] Ferdinand Greiss, Shirley S. Daube, Vincent Noireaux, and Roy Bar-Ziv. From deterministic to fuzzy decision-making in artificial cells. *Nature Communications*, 11(1):5648, 2020. ISSN 2041-1723. doi: 10.1038/s41467-020-19395-4. URL <https://doi.org/10.1038/s41467-020-19395-4>.
- [113] A. L. Mulyukin, S. N. Filippova, A. N. Kozlova, N. A. Surgucheva, T. I. Bogdanova, I. A. Tsaplina, and G. I. El'-Registan. Non-species-specific effects of unacylated homoserine lactone and hexylresorcinol, low molecular weight autoregulators, on the growth and development of bacteria. *Microbiology*, 75(4): 405–414, 2006. ISSN 1608-3237. doi: 10.1134/S0026261706040072. URL <https://doi.org/10.1134/S0026261706040072>.
- [114] Jonathan V. Selinger. *Ising Model for Ferromagnetism*, pages 7–24. Springer International Publishing, Cham, 2016. ISBN 978-3-319-21054-4. doi: 10.1007/978-3-319-21054-4\_2. URL [https://doi.org/10.1007/978-3-319-21054-4\\_2](https://doi.org/10.1007/978-3-319-21054-4_2).
- [115] William P. J. Smith, Yohan Davit, James M. Osborne, Wook Kim, Kevin R. Foster, and Joe M. Pitt-Francis. Cell morphology drives spatial patterning in microbial communities. *Proceedings of the National Academy of Sciences*, 114(3): E280–E286, 2017. doi: 10.1073/pnas.1613007114. URL <https://www.pnas.org/content/pnas/114/3/E280.full.pdf>.